Measurements of Thermo-Acoustic Coupling

Thesis by

Winston Pun

In Partial Fulfillment of the Requirements

for the Degree of

Doctor of Philosophy

California Institute of Technology
Pasadena, California
2001
(Defended May 24, 2001)

ACKNOWLEDGEMENTS

This work could not have been completed without the help and encouragement of many of those around me. I would like to express my gratitude to my advisor, Prof. Fred Culick, for his guidance during my graduate career and in the preparation of this thesis. I would also like to thank Professors Mory Gharib, Melany Hunt, and Richard Murray for serving on my thesis committee.

I would like to acknowledge the financial support of AFOSR, DURIP, the Department of Energy's AGTSR program, ENEL, L.A. County Sanitation District, and the California Institute of Technology.

Those in the JPC research group have also contributed greatly to this work, as well as contributing to an enjoyable working environment. In particular, I would like to acknowledge the collaboration of Steve Palm with the OH PLIF measurements. I greatly value both his technical expertise and friendship. Thanks also are due to Konstantin Matveev and Guido Poncia for their significant contributions to the work with the Rijke tube. I would like to thank Giorgio Isella and Claude Seywert for occasionally hauling me out to the Red Door and contributing to my social (SC) as well as professional development. I would also like to thank Al Ratner, Grant Swenson, Sanjeev Malhotra, and Olivier Duchemin for their numerous discussions and for always being available whenever heavy lifting was required in the lab.

A special thanks to my family and to Suzie, for their support and encouragement.

Thank you all for helping me bring this thesis into reality!

ABSTRACT

The problem of combustion instabilities has existed since the early 1940s, when they were observed during the development of solid and liquid rocket engines. While various engineering solutions have served well in these fields, the problem is revisited in modern gas-turbine engines. The purpose of this work is to provide experimental measurements of laboratory devices that exhibit thermo-acoustic coupling, similar to the interaction observed during combustion instabilities, which will aid in the design and development of stable systems.

Possibly the simplest device which exhibits these characteristics is a Rijke tube. An electrical, horizontally mounted, 1 m long version of the original Rijke tube is presented, with measurements taken during unstable and stable operation. An accurate stability boundary with uncertainty is determined for a heater position of x/L = ¼, as a function of mass flow rate and heater power. Hysteresis, not previously reported, is observed at flow rates above 3 g/s. A one-dimensional model of the stability boundary with linear acoustics is shown to have qualitative agreement with experimental data.

A novel technique has also been devised which can provide insight into the local dynamic response of a flame to an acoustic field. In the experiments, a test chamber is acoustically excited by a pair of low-frequency drivers. The response of the flame is visualized by two techniques; chemiluminescence and planar laser-induced fluorescence (PLIF) of the hydroxyl (OH) radical, both of which are well-known indicators for heat release in flames. The resulting images are phase-resolved and averaged to yield a qualitative picture of the fluctuation of the heat release. The images are correlated with a

pressure transducer near the flame, which allows stability to be evaluated using Rayleigh's criterion and a combustion response function. This is the first known measurement of the combustion dynamics of a flame over a range of frequencies. Results indicate that the drive frequency and burner configuration have a pronounced effect on the response of the flame. Drive frequencies ranging from 22 Hz to 55 Hz are applied to the jet mixed burner, supplied with a premixed 50/50 mixture of methane and carbon dioxide at a Reynolds number of 20,000. The burner is operated in two configurations; with an aerodynamically stabilized flame and with a flame stabilized by two protruding bluff-bodies. Results indicate that in general the bluff-body stabilized flame is less sensitive to chamber acoustic excitation.

TABLE OF CONTENTS

Acknowledgements ..... **iii**

Abstract ..... **iv**

Table of Contents ..... **vi**

List of Figures ..... **xi**

List of Tables ..... **xviii**

CHAPTER 1 INTRODUCTION **1**

1.1 MOTIVATION **1**

1.2 OBJECTIVES **4**

1.3 RAYLEIGH'S CRITERION **5**

1.4 PREVIOUS WORK **7**

1.4.1 The Electrical Rijke Tube 7

1.4.2 Flares 8

1.4.3 Combustion Dynamics of Unsteady Flames 9

CHAPTER 2 THE RIJKE TUBE **13**

2.1 EXPERIMENTAL SETUP **13**

2.1.1 Heat Source 14

2.1.2 Air Flow 15

2.1.3 Pressure Transducers 16

2.1.4 Thermocouples 17

2.1.5 Data Acquisition System 18

2.2 EXPERIMENTAL PROCEDURE 19

2.3 RESULTS 20

2.3.1 Hysteretic Behavior 25

2.3.2 Stability Boundary 33

2.4 PREDICTION OF THE STABILITY BOUNDARY 35

2.5 COMPARISON OF PREDICTION WITH EXPERIMENTAL RESULTS 39

2.6 SUMMARY 42

CHAPTER 3 FULL-SCALE FLARE AND SUB-SCALE MODEL 44

3.1 FULL-SCALE FLARE 45

3.1.1 Introduction 45

3.1.2 Description of Full-Scale Flare 46

3.1.3 Diagnostics 47

3.1.4 Results 48

3.1.5 Possible Driving Mechanisms 55

3.2 SUB-SCALE FLARE MODEL 55

3.2.1 Apparatus and Diagnostics 55

3.2.2 Scaling of the Model 58

3.3 CONCLUSIONS 60

CHAPTER 4 CHEMILUMINESCENCE MEASUREMENTS 62

4.1 EXPERIMENTAL SETUP 63

4.1.1 Acoustic Driving System 63

4.1.2 Acoustic Cavity 64

4.1.3 Test Burners 65

4.2 ACOUSTIC PROPERTIES 68

4.3 DIAGNOSTICS 71

4.3.1 Pressure Transducers 71

4.3.2 Data Acquisition System 71

4.3.3 High-Speed Video Camera 72

4.3.4 Additional Electronics 72

4.3.5 Shadowgraph Setup 73

4.3.6 Chemiluminescence Measurements 74

4.4 SHADOWGRAPH RESULTS 75

4.5 CHEMILUMINESCENCE RESULTS 76

4.5.1 Two-Dimensional Flame Structure 76

4.5.2 Axial Flame Structure 83

4.5.3 Modified Rayleigh Index 91

4.5.4 Global Forced Rayleigh Results 92

4.5.5 Spatially Resolved Forced Rayleigh Results 93

4.6 SUMMARY 95

CHAPTER 5 OH PLIF MEASUREMENTS 97

5.1 PLANAR LASER-INDUCED FLUORESCENCE OF OH 97

5.1.1 PLIF Theory 97

5.1.2 Laser System 103

5.1.3 Optics 104

5.1.4 ICCD Camera 107

5.2 EXPERIMENTAL PROCEDURE 108

5.3 DATA REDUCTION 110

5.3.1 Phase Characterization 110

5.3.2 Image Processing 111

5.4 OH PLIF RESULTS 112

5.4.1 Pressure and Heat Release Measurements 112

5.4.2 Forced Rayleigh Index 127

5.4.3 Global Rayleigh Results 127

5.4.4 Spatially Resolved Rayleigh Results 129

5.4.5 Combustion Response 139

5.5 SUMMARY 145

CHAPTER 6 CONCLUDING REMARKS 147

Appendix A Mechanical Drawings 152

Appendix B Gas Mixture Viscosity Calculation 156

Appendix C Chemiluminescence Rayleigh Indices 158

Appendix D Locally Normalized Combustion Response 167

REFERENCES 170

LIST OF FIGURES

Figure 1-1: Effect of equivalence ratio on NO_x production (from Rosfjord 1995). 2

Figure 1-2: Combustor system. 3

Figure 2-1: Electrical Rijke tube experimental setup. 14

Figure 2-2: Expected stability boundary. 19

Figure 2-3: Steady state stable Rijke tube data recordings. (Mean power = 995 W, mean mass flow = 3.3 g/s). 22

Figure 2-4: Steady state unstable Rijke tube data recordings. (Mean power = 995 W, mean mass flow = 3.1 g/s). 23

Figure 2-5: FFTs of an unstable case in the Rijke tube. 24

Figure 2-6: Bulk RMS pressures at a mean flow rate of 3.15 g/s. 26

Figure 2-7: Bulk RMS pressures at a mean flow rate of 2.44 g/s. 27

Figure 2-8: Frequencies of oscillations for first two dominant modes at 3.15 g/s..... 29

Figure 2-9: RMS pressures of oscillations for first two dominant modes at 3.15 g/s..... 30

Figure 2-10: Frequencies of oscillations for first two dominant modes at 2.44 g/s..... 31

Figure 2-11: RMS pressures of oscillations for first two dominant modes at 2.44 g/s..... 32

Figure 2-12: Stability boundary for Rijke tube at x/L = ¼. 34

Figure 2-13: Efficiency factor, E, for $r^* = 1.0$. 40

Figure 2-14: Stability boundary prediction. Solid black line is for T = 600K, and the dashed black line for T = 300K. 41

Figure 3-1: Landfill flare station. 45

Figure 3-2: Instrumentation layout on full-scale flare. 47

Figure 3-3: Flare bulk temperature profile..... 49

Figure 3-4: Flare pressure traces (low pass filtered at a cutoff of 200 Hz). 50

Figure 3-5: FFT of pressure traces in full-scale flare. 52

Figure 3-6: Flare pressure traces, filtered using a 6th order butterworth phase-preserving bandpass filter between 7-10 Hz (1st mode). 53

Figure 3-7: Flare pressure traces, filtered using a 6th order butterworth phase-preserving bandpass filter between 21-24 Hz (2nd mode). 54

Figure 3-8: Schematic of sub-scale flare model assembly..... 57

Figure 4-1: Schematic of overall test section. 64

Figure 4-2: Bluff-body stabilized burner flameholder detail, viewed from the upstream side. 66

Figure 4-3: (a) Aerodynamically stabilized burner (b) bluff-body stabilized burner. 67

Figure 4-4: Gas feed system. 68

Figure 4-5: Peak-to-peak pressure amplitudes in the chamber, driven at various frequencies (no flame)..... 69

Figure 4-6: RMS pressure in the chamber, when driven at various frequencies (no flame). 69

Figure 4-7: Shadowgraph imaging setup. 73

Figure 4-8: Shadowgraph results above the burner tube for (a) aerodynamically and (b) bluff-body stabilized cases. 75

Figure 4-9: Chemiluminescence contour plots at 22 Hz for (a) aerodynamically stabilized and (b) bluff-body stabilized cases. 78

Figure 4-10: Chemiluminescence contour plots at 27 Hz for (a) aerodynamically stabilized and (b) bluff-body stabilized cases. 79

Figure 4-11: Chemiluminescence contour plots at 32 Hz for (a) aerodynamically stabilized and (b) bluff-body stabilized cases. 80

Figure 4-12: Chemiluminescence contour plots at 37 Hz for (a) aerodynamically stabilized and (b) bluff-body stabilized cases. 81

Figure 4-13: Chemiluminescence contour plots at 55 Hz for (a) aerodynamically stabilized and (b) bluff-body stabilized cases. 82

Figure 4-14: Mean axial intensities at 22 Hz (a) aerodynamic (b) bluff-body. 86

Figure 4-15: Normalized axial intensities at 22 Hz (a) aerodynamic (b) bluff-body. 86

Figure 4-16: Mean axial intensities at 27 Hz (a) aerodynamic (b) bluff-body. 87

Figure 4-17: Normalized axial intensities at 27 Hz (a) aerodynamic (b) bluff-body. 87

Figure 4-18: Mean axial intensities at 32 Hz (a) aerodynamic (b) bluff-body. 88

Figure 4-19: Normalized axial intensities at 32 Hz (a) aerodynamic (b) bluff-body. 88

Figure 4-20: Mean axial intensities at 37 Hz (a) aerodynamic (b) bluff-body. 89

Figure 4-21: Normalized axial intensities at 37 Hz (a) aerodynamic (b) bluff-body. 89

Figure 4-22: Mean axial intensities at 55 Hz (a) aerodynamic (b) bluff-body. 90

Figure 4-23: Normalized axial intensities at 55 Hz (a) aerodynamic (b) bluff-body. 90

Figure 4-24: Chemiluminescence global forced Rayleigh indices. 92

Figure 4-25: Chemiluminescence 2D forced Rayleigh indices at 32 Hz for (a) aerodynamic and (b) bluff-body stabilized burners. 94

Figure 4-26: Chemiluminescence axial forced Rayleigh indices. 94

Figure 5-1: Simplified energy level transfer diagram for LIF. 99

Figure 5-2: PLIF system. 105

Figure 5-3: Mixer/doubler system (Stages available but not used are indicated by dashed lines). 106

Figure 5-4: OH PLIF optics arrangement. 106

Figure 5-5: Phase-binning procedure for OH PLIF images. 111

Figure 5-6: OH PLIF images over a period of a sinusoidal pressure oscillation for the aerodynamically stabilized burner at 32 Hz. The intensity scale is in number of counts, and the x and y coordinates are in pixels. 114

Figure 5-7: Pressure and heat release traces and power spectrums for the aerodynamically stabilized burner driven at 22 Hz. 115

Figure 5-8: Pressure and heat release traces and power spectrums for the bluff-body stabilized burner driven at 22 Hz. 116

Figure 5-9: Pressure and heat release traces and power spectrums for the aerodynamically stabilized burner driven at 27 Hz. 117

Figure 5-10: Pressure and heat release traces and power spectrums for the bluff-body stabilized burner driven at 27 Hz. 118

Figure 5-11: Pressure and heat release traces and power spectrums for the aerodynamically stabilized burner driven at 32 Hz. 119

Figure 5-12: Pressure and heat release traces and power spectrums for the bluff-body stabilized burner driven at 32 Hz. 120

Figure 5-13: Pressure and heat release traces and power spectrums for the aerodynamically stabilized burner driven at 37 Hz. 121

Figure 5-14: Pressure and heat release traces and power spectrums for the bluff-body stabilized burner driven at 37 Hz. 122

Figure 5-15: Pressure and heat release traces and power spectrums for the aerodynamically stabilized burner driven at 55 Hz. 123

Figure 5-16: Pressure and heat release traces and power spectrums for the bluff-body stabilized burner driven at 55 Hz. 124

Figure 5-17: Phase relationship between the 1st mode of pressure and heat release for the (a) aerodynamically stabilized and (b) bluff-body stabilized cases at 22 Hz. Heat release traces have been scaled for ease of comparison. 126

Figure 5-18: Frequency driven global Rayleigh index. 128

Figure 5-19: Contour plot of R_f for (a) aerodynamically and (b) bluff-body stabilized burners at a driving frequency of 22 Hz. 131

Figure 5-20: Contour plot of R_f for (a) aerodynamically and (b) bluff-body stabilized burners at a driving frequency of 27 Hz. 132

Figure 5-21: Contour plot of R_f for (a) aerodynamically and (b) bluff-body stabilized burners at a driving frequency of 32 Hz. 133

Figure 5-22: Contour plot of R_f for (a) aerodynamically and (b) bluff-body stabilized burners at a driving frequency of 37 Hz. 134

Figure 5-23: Contour plot of R_f for (a) aerodynamically and (b) bluff-body stabilized burners at a driving frequency of 55 Hz. 135

Figure 5-24: Aerodynamically stabilized 2D Rayleigh plots. 138

Figure 5-25: Bluff-body stabilized 2D Rayleigh plots. 138

Figure 5-26: Axial Rayleigh index plot: Solid lines are the aerodynamically stabilized burner, and dashed lines are the bluff-body stabilized case. 139

Figure 5-27: Global combustion response function. 140

Figure 5-28: Combustion response – magnitude (a) aerodynamically stabilized (b) bluff-body stabilized. 142

Figure 5-29: Combustion response – phase (a) aerodynamically stabilized (b) bluff-body stabilized. 143

Figure A-1: 1/12th scale flare model: chamber section. 153

Figure A-2: 1/12th scale flare model: burner section. 154

Figure A-3: Instrumentation boss. 155

Figure C-1: Chemiluminescence axial forced Rayleigh indices at 22 Hz. ...159

Figure C-2: Chemiluminescence axial forced Rayleigh indices at 27 Hz. ...160

Figure C-3: Chemiluminescence axial forced Rayleigh indices at 32 Hz. ...160

Figure C-4: Chemiluminescence axial forced Rayleigh indices at 37 Hz. ...161

Figure C-5: Chemiluminescence axial forced Rayleigh indices at 55 Hz. ...161

Figure C-6: Chemiluminescence 2D forced Rayleigh indices at 22 Hz for (a) aerodynamically and (b) bluff-body stabilized burners. ...162

Figure C-7: Chemiluminescence 2D forced Rayleigh indices at 22 Hz for (a) aerodynamically and (b) bluff-body stabilized burners. ...163

Figure C-8: Chemiluminescence 2D forced Rayleigh indices at 22 Hz for (a) aerodynamically and (b) bluff-body stabilized burners. ...164

Figure C-9: Chemiluminescence 2D forced Rayleigh indices at 22 Hz for (a) aerodynamically and (b) bluff-body stabilized burners. ...165

Figure C-10: Chemiluminescence 2D forced Rayleigh indices at 22 Hz for (a) aerodynamically and (b) bluff-body stabilized burners. ..……...166

Figure D-1: Locally normalized combustion response – magnitude (intensity is on a log scale) (a) aerodynamically stabilized (b) bluff-body stabilized. .....….169

LIST OF TABLES

Table 1-1: Previous work in oscillating flames. 11

Table 2-1: PCB 112A04 pressure transducer properties with 422D11 charge amp. 17

Table 2-2: Data acquisition analog measurements. 18

Table 4-1: Flame base position and oscillation..... 84

Table 5-1: Smoothing filter weighting matrix. 112

Table B-1: Coefficients for viscosity quadratic fit, valid for P = 1 atm, 5 °C < T < 45 °C. 157

Chapter 1
Introduction

1.1 Motivation

Of the six principle air pollutants tracked by the EPA (carbon monoxide, lead, nitrogen oxides, particulate matter, sulfur dioxide, and volatile organic compounds), all have made significant reductions in emissions since the passage of the Clean Air Act in 1970, except for nitrogen oxides[1]. NO_x, consisting of NO and NO_2 are contributors to stratospheric ozone depletion, acid rain, and smog. Stricter government regulations regarding pollutant emissions and in particular oxides of nitrogen have come into effect. As a result, the gas-turbine industry is seeking ways to reduce NO_x emissions.

[1] From document EPA-456/F-98-006 (September 1998)

Several techniques have been explored to lower pollutant production, including catalytic combustion, rich-burn/quick-quench schemes, fuel staging, water or steam injection, and lean premixed combustion. Of these, the most promising technique is believed to be the operation of combustors in the regime of lean, premixed flames (Correa 1992). The general strategy is to reduce flame temperatures, and thereby minimize NO_x production due to the thermal (or Zeldovich) mechanism. The other pathways for production of nitrogen oxides, the prompt or Fenimore mechanism, and the nitrous oxide mechanism are typically not significant contributors to NO_x formation under gas-turbine combustion conditions. Another important consideration in lean combustion is the uniformity of the fuel-air mixture ratio, since both spatial and temporal fluctuations in mixture ratio will result in higher NO_x production (Swenson et al. 1996; Fric 1993).

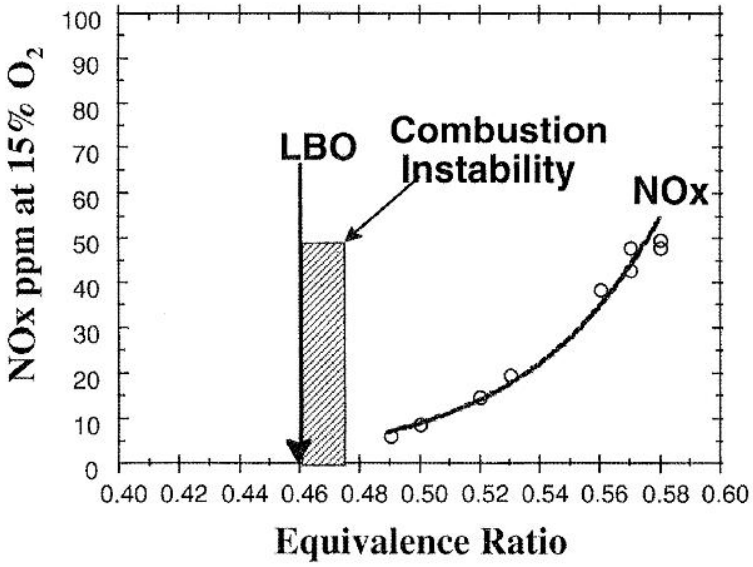

Figure 1-1: Effect of equivalence ratio on NO_x production (from Rosfjord 1995).

Operation near the lean blowout limit is desirable to minimize high flame temperatures. This circumstance gives rise to conditions under which combustion instabilities are more likely to occur in lean premixed systems, and have in fact been observed in new

combustors operating under these conditions, as shown in Figure 1-1. The term combustion instability refers to the presence of a large amplitude pressure oscillation inside the combustion chamber and does not indicate unstable burning of the flame. The pressure excursions associated with these instabilities can cause unacceptable levels of vibration and increased rates of heat transfer. Vibration levels may induce mechanical failure, and enhanced heat transfer can cause components already operating near high temperature limits, such as the liner or turbine blades, to fail catastrophically.

Lean premixed combustion systems are especially susceptible to combustion instabilities, since small pressure oscillations in the chamber can also affect air feed lines, causing variations in the fuel-oxidizer ratio, which in turn will produce fluctuations in the heat release rate, which can further drive the pressure oscillations. Incomplete premixing of the fuel and oxidizer can have a similar effect, creating pockets of burning mixtures at different equivalence ratios, which can drive acoustic modes in the chamber. This interaction suggests a coupling or feedback loop that exists between combustor dynamics and combustion dynamics, as shown in Figure 1-2.

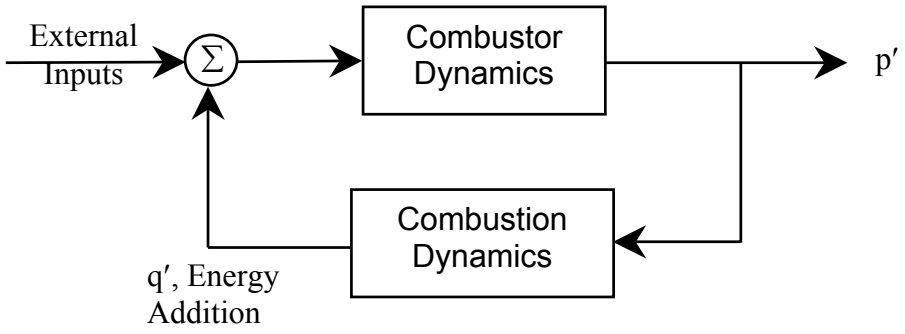

Figure 1-2: Combustor system.

1.2 Objectives

The mechanisms causing combustion instabilities in gas turbine combustors are not well understood. Although similar in principle (Raun et al. 1983) to a Rijke tube (a heat-driven acoustic oscillation), the added geometric complexities and injector configurations of a practical combustor make their dynamical behavior unpredictable. Current industry design techniques are largely empirical and not clearly defined with respect to combustion instabilities. Ultimately, industrial combustor designs are finalized without a clear measure of the stability margins of the system. A method for predicting and evaluating the stability characteristics of a given combustor configuration is needed for more robust designs. The central objectives of this work are

- To provide accurate measurements of nonlinear instability phenomena of laboratory devices for use in model validation.
- To develop tools for evaluation of the combustion response of a burner in a variety of combustor configurations.
- To evaluate the use of chemiluminescence and OH PLIF as indicators for the response of a combustion system in a forced acoustic environment.

It is anticipated that this work and future work derived from it will lead to design rules of thumb that will improve current design techniques and the understanding of acoustic-flame interactions.

1.3 Rayleigh's Criterion

When considering the phenomena of heat-driven pressure oscillations, Rayleigh stated his now well-known criterion in 1878:

> "If heat be given to the air at the moment of greatest rarefaction, or be taken from it at the moment of greatest rarefaction, the vibration is encouraged. On the other hand, if heat be given at the moment of greatest rarefaction, or abstracted at the moment of greatest condensation, the vibration is discouraged."

The mathematical development of Rayleigh's criterion follows from the conservation equations. Following the framework of Culick (1976), the mass, momentum, and energy equations with sources can be written as

(1-1) $$\frac{\partial \rho}{\partial t} + \mathbf{u} \cdot \nabla \rho = \mathcal{W}$$

(1-2) $$\rho \frac{\partial \mathbf{u}}{\partial t} + \rho\, \mathbf{u} \cdot \nabla \mathbf{u} = -\nabla p + \vec{\mathcal{F}}$$

(1-3) $$\frac{\partial p}{\partial t} + \gamma p \nabla \cdot \mathbf{u} = -\mathbf{u} \cdot \nabla p + \mathcal{P}$$

where

(1-4) $$\mathcal{W} = w_s - \rho \nabla \cdot \mathbf{u}$$

(1-5) $$\vec{\mathcal{F}} = \mathbf{F_s} - \mathbf{u} w_s$$

(1-6) $$\mathcal{P} = \frac{R}{C_V}\left[Q_s - \mathbf{u} \cdot \mathbf{F_s} + w_s \frac{u^2}{2} \right]$$

where ρ, p, and $\mathbf{u}$, are the density, pressure, and velocity in the gas phase, w_s, $\mathbf{F_s}$, and Q_s are sources of mass, momentum, and energy. The analysis can be carried out in one-

dimension for convenience, following the development of Sterling (1987) and Culick (1987). Expanding the momentum and energy equations (1-2) and (1-3) in terms of mean and fluctuating quantities, multiplying them by u' and $\frac{p'}{\gamma p_o}$ respectively, and adding them together without mass sources, we arrive at

(1-7)
$$\left(\frac{\partial}{\partial t}+u_o\frac{\partial}{\partial x}\right)\left(\frac{\rho_o u'^2}{2}+\frac{p'^2}{2\gamma p_o}\right)=\frac{R}{C_V\gamma p_o}Q'p'-\frac{\partial}{\partial x}(u'p')-\frac{u'p'}{\gamma p_o}\frac{\partial p_o}{\partial x}$$
$$-\left(\rho' u' u_o+\rho_o u'^2+\frac{p'^2}{p_o}\right)\frac{\partial u_o}{\partial x},$$

where $(\,)_o$ are mean quantities and $(\,)'$ represent fluctuating quantities. Assuming small changes in a correspondingly low mean flow, orthogonality between u' and p', and integrating over the combustor volume we are left with

(1-8)
$$\frac{\partial}{\partial t}\left(\frac{\rho_o u'^2}{2}+\frac{p'^2}{2\gamma p_o}\right)=\frac{R}{C_V\gamma p_o}Q'p' \quad .$$

Integrating equation (1-8) over the volume of the combustor, V, and a cycle of the oscillation, τ, we arrive at

(1-9)
$$\Delta E=\frac{(\gamma-1)}{\gamma p_o}\int dV\int_t^{t+\tau} p'Q'dt\,,$$

where ΔE is the energy added to the system during a cycle. Equation (1-9) is an explicit expression of Rayleigh's criterion.

1.4 Previous Work

1.4.1 The Electrical Rijke Tube

A Rijke tube is comprised of a tube with a mean airflow and a heat source, often a heated wire gauze. At a particular heater position, temperature, and airflow, the tube can be made to "sing" as acoustic modes within the tube are excited. Through consideration of Rayleigh's criterion, Collyer and Ayres (1972) were able to excite the 1st through 3rd modes of a Rijke tube consisting of 3.66 cm diameter Pyrex glass tubes, of length 0.79 m and 1.54 m. The fundamental mode can be produced by placing the heater at L/4, the 2nd mode by a heater at L/8 or 5L/8, and the 3rd mode with a heater at L/12, 5L/12, or 3L/4. It was noted that the frequency of the modes increased slightly due to higher air temperatures, so a compensating heater to increase the air temperature at lower power levels was introduced just below L/2. Though not ideal, the addition of the second heater had the general desired effect.

Katto and Sajiki (1977) performed a wide range of experiments in an electrically driven Rijke tube. Their experimental arrangement consisted of a compressor supplying airflow rates up to 50 L/min through a large surge tank and into a steel tube with an inner diameter of 30 mm, with lengths of 310 mm to 2810 mm. The kanthar wire heaters were in a spiral or coil configuration. Stability boundaries are given, but without temperature profiles, a clear criterion for the onset of instability, or limit cycle amplitudes. Work by Madarame (1981a, 1981b), involved a similar apparatus, but added measurements of the linear growth rate and excited frequencies. A summary of work done on Rijke tubes and similar devices is contained in the review paper of Raun et al. (1993). Chapter 2 contains

the results and development of a model used to predict the stability boundary of a Rijke tube.

1.4.2 Flares

A device similar to a Rijke tube is the biogas flare, which is used to dispose of gases produced in a landfill site. Typically landfill flares use an enclosed design, with all combustion taking place inside a refractory-lined chamber, such that no flame is visible. This configuration allows control of product gas residence time and temperatures in order to minimize pollutant emissions (John Zink 1988). A consequence of this configuration is that the flare burner may interact with the feed system and chamber acoustics to produce an unstable system. While other types of unstable systems may be corrected by trial and error, unstable flares are often left to run below full capacity due to government restrictions on noise levels near residential areas. For testing purposes, landfill gas composition is taken to contain 50% methane and 50% carbon dioxide (Christo et al. 1998). At these compositions, the flame has substantially different properties than typical methane-air flames. Work by Qin et al. (2001) has shown that the presence of high CO_2 quantities decreases laminar flame speeds and extinction strain rates, while increasing NO_x production. Further work regarding unstable flares has been notably absent in the literature. Data taken from an unstable flare site, and sub-scale modeling attempts are presented in chapter 3.

1.4.3 Combustion Dynamics of Unsteady Flames

In order to study the unsteady dynamics of a combustion chamber, a reliable technique to visualize the combustion process and its response to an oscillating pressure field is required. Two techniques that can be used to perform these measurements are chemiluminescence and planar laser-induced fluorescence (PLIF). McManus et al. (1995) give a review of these techniques as they are applied in modern combustion research.

Chemiluminescence of various radicals of combustion, in particular CH, is an excellent marker of the reaction zone, and has been used by a number of researchers to study heat release in unsteady flames. One major drawback of chemiluminescence is the inability of the measurements to provide high spatial resolution, since line-of-sight integration occurs at the detector. These experiments can be categorized into two groups; measurements using a photo-multiplier tube (PMT) with a slit obscuring a portion of the flame to obtain some spatial (typically axial) resolution (Poinsot et al. 1987; Sterling 1991; Chen et al. 1993; and Kappei et al. 2000), and full two-dimensional imaging using a charge-coupled device (CCD) based camera (Broda et al. 1990; Kendrick et al. 1999; and Venkataraman et al. 1999). Of these works, only Chen et al. (1993) involved an acoustically forced flame, but used a PMT with a slit configuration that obtained only integrated one-dimensional information. Poinsot et al. (1987) had the capability of injecting acoustic waves into their system, but did not do so. They later made use of this capability to perform combustion instability active suppression control experiments (Poinsot et al., 1989). Venkataraman et al. (1999) used phase-resolved CH chemiluminescence to study

the instability characteristics of a dump combustor. They determined that swirl tends to induce combustion instabilities near the lean blowout limit.

Dyer and Crosley (1982) performed the first demonstration of 2D (or planar) laser-induced fluorescence (LIF) of the hydroxyl radical in a flame. Spatial resolution is defined by the resolution of the detector, and the laser sheet, typically several hundred microns in width. The PLIF technique has been used since then to measure a variety of chemical species in unsteady reacting flows, including OH as a measure of the heat release (Cadou et al. 1991; and Shih et al. 1996), and NO seeded fuel to measure the temperature field (Cadou et al. 1998). PLIF measurements can discriminate strongly between different chemical species, while chemiluminescence measurements often contain overlapping source contributions to the signal. A summary of these various works involving both chemiluminescence and PLIF is provided in Table 1-1, including the acoustic frequencies examined in the studies.

While chemiluminescence measurements are more readily obtained, since they do not require a costly laser pump source, they have several disadvantages. Chemiluminesence measurements cannot capture fine structures in flames, since the signal is integrated through the depth of the flame. PLIF images are obtained of only a very specific plane where the laser sheet illuminates the flame. Another disadvantage of chemiluminescence is that the signal is several orders of magnitude weaker than PLIF. This decreases the temporal resolution of measurements, since longer integration times are required to obtain a sufficiently strong signal. A typical integration time for a single shot using

chemiluminescence is on the order of approximately 100 μs, versus 100 ns when performing PLIF.

	Chemiluminescence	PLIF
Naturally Unsteady	• Poinsot et al. (1987) (440-590 Hz) • Sterling and Zukoski (1991) (188 Hz) • Broda et al. (1998) (1750 Hz) • Kendrick et al. (1999) (235 Hz, 355 Hz) • Venkataraman et al. (1999) (490 Hz) • Kappei et al. (2000) (370-460 Hz)	• Cadou et al. (1991) (43 Hz) • Shih et al. (1996) (400 Hz) • Cadou et al. (1998) (328 Hz)
Acoustic Forcing	• Chen et al. (1993) (300 Hz, 400 Hz)	• Cadou et al. (1998) (360 Hz, 420 Hz)

Table 1-1: Previous work in oscillating flames.

Most experimental work characterizing various combustor configurations has been performed on naturally unstable systems (see Table 1-1). However, these results are specific to the combustors tested and provide little insight to how a particular injector or burner design will behave in a different combustor. A study of the acoustic coupling between fuel injectors and an applied acoustic field has been carried out by Anderson et al. (1998), but only for cold flow experiments. Work by Chen et al. (1993) with premixed flames was specifically designed to simulate solid rocket propellants and used the same apparatus as Sankar et al. (1990). It produced one-dimensional spatial results and used only two forcing frequencies. The study by Cadou et al. (1998) was based on a specific 2D dump combustor configuration and showed little response to nonresonant forcing. A more generalized body of work is required to provide a scientific understanding of guidelines that will be useful in designing stable combustion systems.

Although OH radicals have been used by other researchers (Yip et al. 1994) as a marker of the reaction zone, there is some question as to its validity, since OH is known to persist in high-temperature product gas regions (Allen et al. 1993; Barlow et al. 1990). However, in non-premixed flames, the OH radical quickly vanishes on both sides of the reaction zone (Cessou 1996). Since the burner configuration is only partially premixed in this study, we assume OH to be sufficient as an indicator for the heat release, as is commonly the case.

The purpose of this study is to demonstrate a novel technique that can be used as part of a method to assess stability margins over a range of frequencies for various burner designs. It is anticipated that this technique will provide sufficient temporal and spatial resolution that can be used to improve predictive capabilities and correlate experimental results with numerical simulations. A burner using a mixture of methane and CO_2 is operated in two configurations: aerodynamically stabilized and stabilized with a bluff-body. The burner is subjected to a forced acoustic field with frequencies ranging from 22 Hz to 55 Hz. The configuration discussed here has been chosen to simulate a practical application. It serves as a relatively simple device for which the new diagnostics can be tested with minimal difficulties arising with the test apparatus. Results from chemiluminescence imaging are presented in chapter 4, and laser diagnostics involving OH PLIF are presented in chapter 5.

Chapter 2
The Rijke Tube

This chapter concerns perhaps the simplest device that exhibits a thermo-acoustic instability, namely the Rijke tube. The experimental campaign, results, and model used to predict the stability boundary are discussed.

2.1 Experimental Setup

The classic Rijke tube (Rijke 1859) consists of a vertically mounted glass tube with a wire gauze suspended inside. The gauze is heated using a flame, which causes the tube to "sing" in certain cases. The essential characteristics of the original device are retained with several modifications to better quantify the phenomenon. One of the major changes is orienting the tube horizontally, which removes the mean flow induced by convection. This enables a quantitative investigation of the effect the mean flow has on the system.

The other major change is use of an electrically heated nichrome grid as a heat source instead of a flame since the power input into the system is better characterized.

The electrical horizontal Rijke tube (pictured in Figure 2-1) consists of a 9.5 x 9.5 cm square aluminum tube, 1.0 m in length. Air is sucked in from one end of the tube (taken as the origin, x = 0) into a large plenum, which acts as a damping chamber to decouple the blower dynamics from the tube.

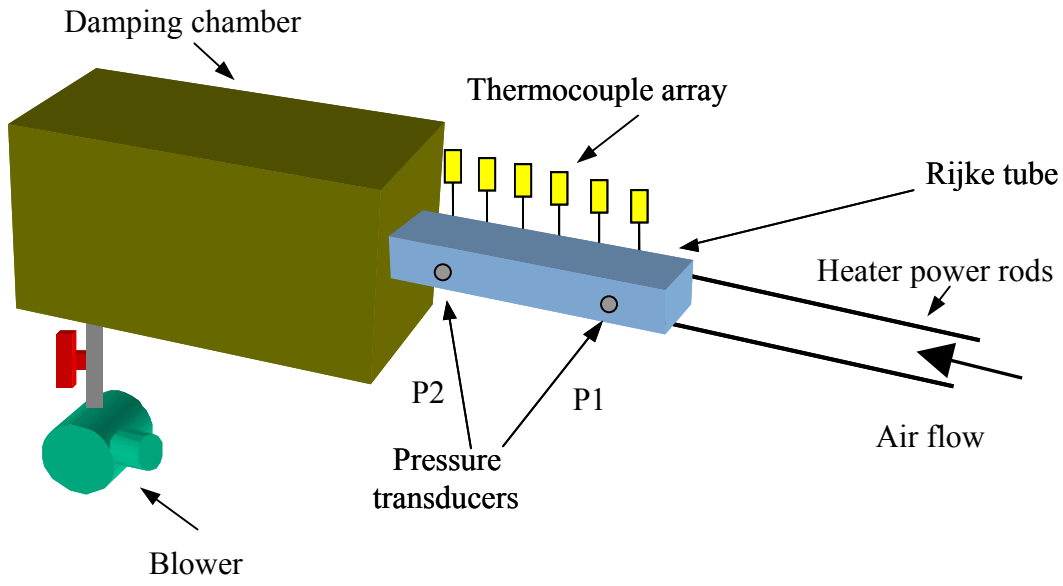

Figure 2-1: Electrical Rijke tube experimental setup.

2.1.1 Heat Source

As previously mentioned, the heat source consists of a nichrome grid (40 mesh) with a wire diameter of 0.01". It is silver brazed to two strips of copper, which form the positive and negative terminals of the heater. The heater is suspended in a frame machined from

macor in order to withstand high temperatures. Two long copper rods, welded directly to the copper strips on the heater, form a solid physical and electrical connection from the heater to the power source. The power source consists of two TCR-20T250 high current power supplies, each capable of producing 500 amps of current. The power supplies are load balanced and operate in parallel, enabling the system to draw up to 1000A. The actual power supplied is dependent on the resistance of the nichrome grid, which changes with temperature. The power supplies are computer controlled using a software-implemented controller to stabilize the output power, although fluctuations on the order of ±1% can occur.

The heater is located at a position of x/L = ¼. This is the ideal location for driving the fundamental mode of an open-open Rijke tube, according to Rayleigh's criterion. Input power is determined by directly measuring the voltage between the copper rods and measuring the current through one of the rods using a current sensor (Amploc, CL500). The final input power measurement is corrected to account for power dissipation along the copper rods.

2.1.2 Air Flow

The mean air flow through the Rijke tube is provided by a GAST R1102 blower, operating at 3450 rpm with a maximum throughput of 0.0127 m^3/s at standard atmospheric conditions. The blower is operated at full capacity with a 2" by-pass ball valve controlling the amount of air drawn through the damping chamber, or from the atmosphere. A large plastic shroud (not pictured) is placed above the entrance to the Rijke tube to minimize air current effects on the system.

The flow rate is measured using a laminar flow element (Meriam 50MW20) and a differential pressure transducer (Honeywell Microswitch). This measurement takes place between the damping chamber and the blower. A thermocouple, located upstream of the laminar flow element, is used to correct for air density and viscosity to produce the total air mass flow rate.

2.1.3 Pressure Transducers

Selection of the proper pressure transducers used in this experiment was critical since they must provide accurate measurements in a hot environment. The transducers used were PCB model 112A04, coupled with a 422D11 charge amplifier and a 482A20 signal conditioner. Table 2-1 lists some of the important characteristics of the pressure transducers. Charge-mode piezoelectric transducers were used, since the majority of the electronics is located in a separate charge amplifier, increasing the operating temperature range while retaining relatively high sensitivities. The two pressure transducers, flush mounted in the tube at positions x/L = 0.15 and x/L = 0.80, are labeled P1 and P2 respectively (see Figure 2-1). In most cases, P1 is on the cold side of the tube and P2 is on the hot side.

Sensitivity	100 mV/psi
Maximum Pressure	5000 psi
Linearity	< 1% FS
Temperature Range	-400 to +600 F
Flash Temperature	3000 F
Resonant Frequency	> 250 kHz
Rise Time	< 2 μs

Table 2-1: PCB 112A04 pressure transducer properties with 422D11 charge amp.

2.1.4 Thermocouples

An array of 15 type K thermocouples is suspended from the top of the tube to the centerline, at positions of x = 5, 10, 15, 22, 27, 30, 35, 40, 45, 50, 56.7, 63.3, 70, 76.7, and 90 cm. An additional thermocouple is located just before the laminar flow element that measures the mean flow through the tube. The odd spacing results from a desire to place more thermocouples nearer to the heat source, as well as to allow the heater to be located at key locations without interfering with the thermocouples. Since the thermocouples have a relatively large time constant, they are multiplexed and sampled at 2 Hz (i.e., all 16 thermocouples are read in 0.5 s). It is not possible for thermocouples to respond quickly enough at the acoustic time scales required in the experiment. They are used solely for bulk temperature measurements.

2.1.5 Data Acquisition System

In order to provide accurate measurements of the acoustic pressures and other relevant phenomenon in the Rijke tube, a fast sampling system is required. The data acquisition system is based on a Pentium III 700 MHz computer. A Computer Boards CIO-DAS1602/12 (12 bit) data acquisition board is installed in the machine, using Sparrow (Murray, 1995) as the software interface. An EXP-16 expansion board accommodates the 16 thermocouples in a multiplexed array and also provides cold junction compensation. The channels acquired are listed in Table 2-2.

Channel	Measurement
0	System thermocouples
1	Cold junction compensation
2	Pressure transducer P1
3	Pressure transducer P2
4	Heater voltage
5	Flow rate (LFE pressure drop)
6	Heater current

Table 2-2: Data acquisition analog measurements.

The DAS1602/12 is operated in single-ended mode, giving a total of up to 16 analog input channels. It also contains two analog output channels, one of which is used to control the power supplies. In this configuration, data could be acquired in short bursts at over 8000 Hz, and for extended periods of time streaming to the hard drive at over 4000 Hz. For this Rijke tube, the primary frequencies are the first two modes at approximately

190 Hz and 380 Hz. These frequencies were easily captured at the data rates capable by the data acquisition system.

2.2 Experimental Procedure

In order to carefully map the stability boundary, a methodical system of acquiring data was employed. Variables in the Rijke tube experiment are the heater power (P), air flow rate or velocity (V), and heater position (x). Based on previous works (Katto and Sajiki 1977; Madarame 1981a), the stability region should be similar to the one schematically shown in Figure 2-2.

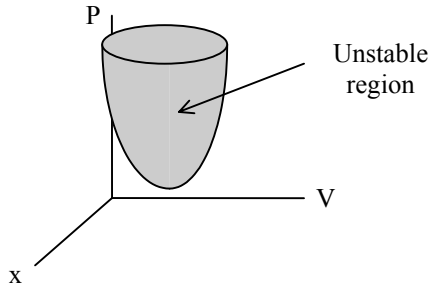

Figure 2-2: Expected stability boundary.

For this work, only one heater position (x/L = ¼) is investigated, although the experiment is easily modified to include other heater positions, which can preferentially drive alternate harmonics in the tube.

Before commencing an experimental run, the tube is subjected to a warm-up procedure, in order to minimize temperature variations as the power input is increased. The warm-up depends on the actual conditions under which the experimental run will take place, based on anticipated stability boundaries. Typically, the power input will be set to

approximately 200 W below the unstable point for a particular flow condition, and the tube run at that rate for 20 minutes. If the stability boundary is not known or incorrectly selected, a more conservative estimate of the stability boundary is used at the expense of an increased duration for the experiment.

Since the flow rate is manually controlled, the flow condition is set, and the power increased via computer control. Initial power increments of 50 W are used while relatively "far" from the stability boundary. As the boundary is approached, the power increments are reduced to the limits of resolution of the controller and power supplies. The tube is held steady at each condition for approximately 120 seconds until the system temperature field has settled and is quasi-static, before data is acquired. Due to the presence of hysteresis at certain conditions, there exist two possible states for the system. The small steps in power followed by a long waiting period prevent transient thermal effects from triggering (Burnley and Culick 2000) the transition to the unstable regime. Once the tube has become unstable, a few more data points are taken within the instability boundary, and then the power increments are reversed to determine the "return to stability" boundary. In a similar fashion, power decrements are initially large and then subsequently refined as the boundary is approached. At each point, a full set of data is acquired for post-processing.

2.3 Results

The raw data obtained by the data acquisition system is post-processed, with the variables converted into appropriate units. The pressure signals are filtered using a 5th order

Butterworth highpass filter with a cutoff frequency of 20 Hz, to eliminate low frequency noise and environmental effects.

Examples of data traces taken at a stable and unstable condition are shown in Figure 2-3 and Figure 2-4 respectively. Notice that while both conditions are very similar, their behavior is quite different. This is due to hysteresis effects, which must take into account the time history or evolution of a particular condition. This will be explored in greater detail in the next section.

Notice in the stable case (Figure 2-3), there is no coherent pressure oscillation. The low frequency drift in the signal is due to thermal drift and noise induced in the pressure transducers. The unstable case (Figure 2-4) shows a well-defined pressure oscillation in both transducers. Differences in amplitude are due to the position of the transducers with respect to the modeshape of the acoustic modes, as well as transducer P2 being located in the hot section. The temperature profiles are characterized by a large jump at x = 25 cm (the position of the heater gauze) of approximately 300 K. There is significant cooling of the air as it progresses downstream in the tube, which is often neglected in modeling efforts. The mass flow rate fluctuates with a period characteristic of the blower (RPM and number of fan blades). In the unstable case (Figure 2-4), the flow rate oscillates approximately out of phase with the pressure oscillations, as would be expected. In both cases, the power fluctuates with a small amplitude high frequency superimposed over a lower frequency higher amplitude, which is due to the action of the controller on the system.

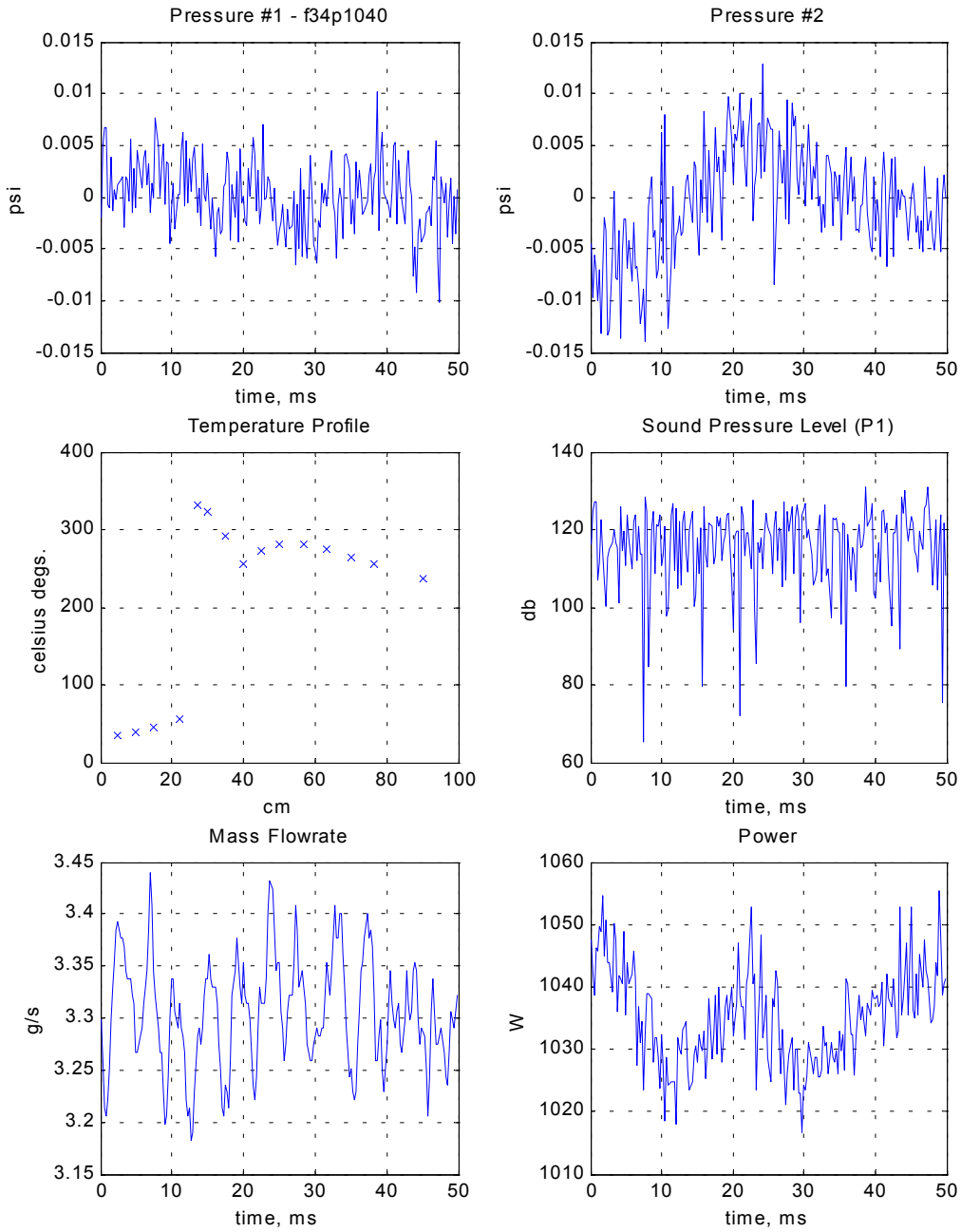

Figure 2-3: Steady state stable Rijke tube data recordings. (Mean power = 995 W, mean mass flow = 3.3 g/s).

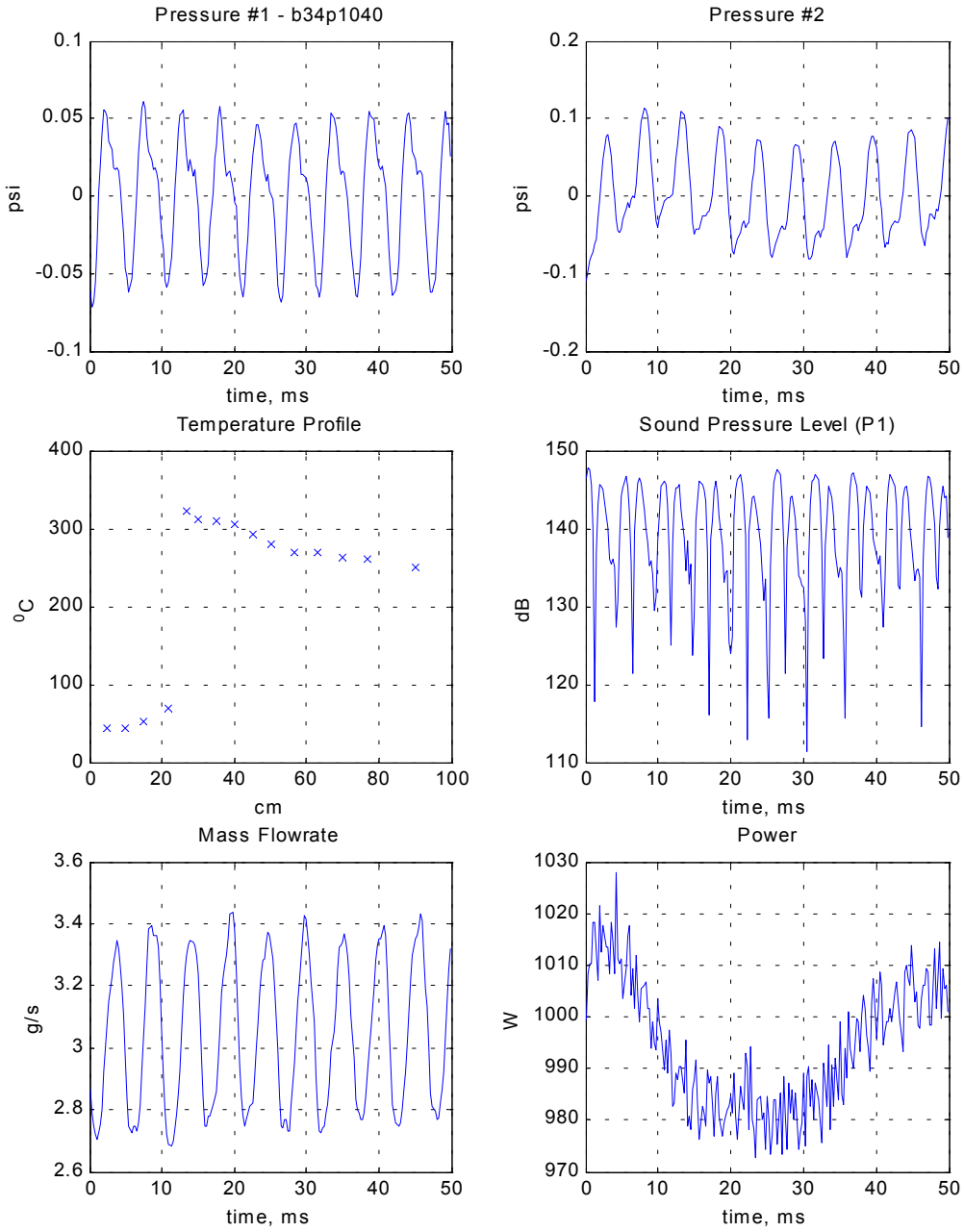

Figure 2-4: Steady state unstable Rijke tube data recordings. (Mean power = 995 W, mean mass flow = 3.1 g/s).

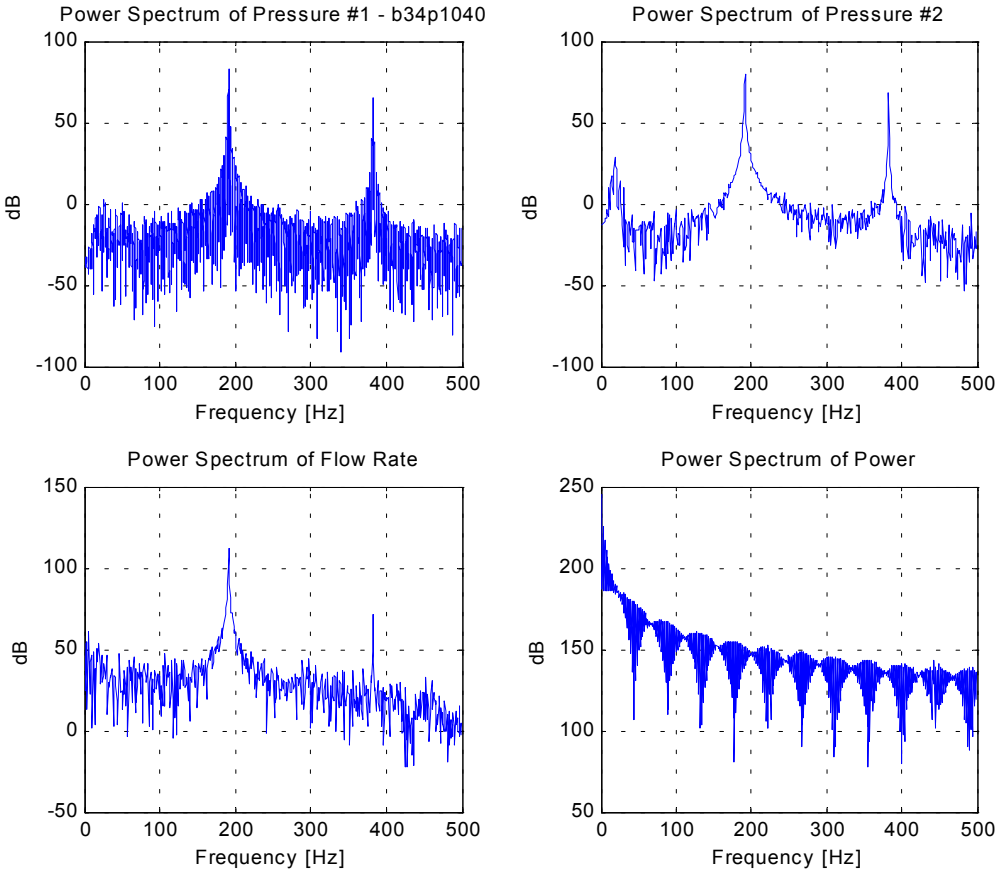

Figure 2-5: FFTs of an unstable case in the Rijke tube.

For the unstable case shown in Figure 2-4, the corresponding FFTs are plotted in Figure 2-5. The first and second modes are most prominent (higher modes are not significant, and are not shown) at approximately 190 Hz and 380 Hz respectively. The spectrum of the flow rate shows a response at the fundamental excitation frequency, but significantly lower excitation of the second mode when compared with the relative magnitudes of the pressure responses, possibly attributable to the damping chamber.

2.3.1 Hysteretic Behavior

As the Rijke tube transitions from a stable to an unstable operating condition, it is important to identify as precisely as possible when this transition actually takes place. One possible measure of the instability is the amplitude of the pressure oscillation. A problem with this definition arises since noise and flow-induced vortices can give rise to increasing pressure amplitudes measured by the transducers. Thus, the appropriate threshold that defines the transition to instability is not well defined. Instead, a combination of approaches is taken, using observation of both the amplitude of the oscillation as well as the frequency of the strongest mode excited. Once the Rijke tube goes unstable, the frequency "locks in" to an unstable mode of the tube. In this case, since the Rijke tube is in an open-open configuration with the heat source located at the ¼ point, the main unstable frequency will be approximately a half-wave (with appropriate end corrections) as dictated by Rayleigh's criterion and chamber acoustics.

Hysteresis implies that the history of the system is important in determining the current state of the system. Hysteresis has been viewed previously in a dump combustor (Isella et al. 1997) and in a Rijke burner (Seywert 2001). An example of the hysteresis in the electrical Rijke tube is shown in Figure 2-6. The cold section represents data taken by transducer P1 at x = 0.15 m, and the hot section by transducer P2 located at x = 0.8 m. The triangles pointing up indicate data points taken as the power is being increased. Since the transitional points are of primary interest, many of the preliminary settings are not recorded and often by-passed as described in the warm-up procedure. Once the

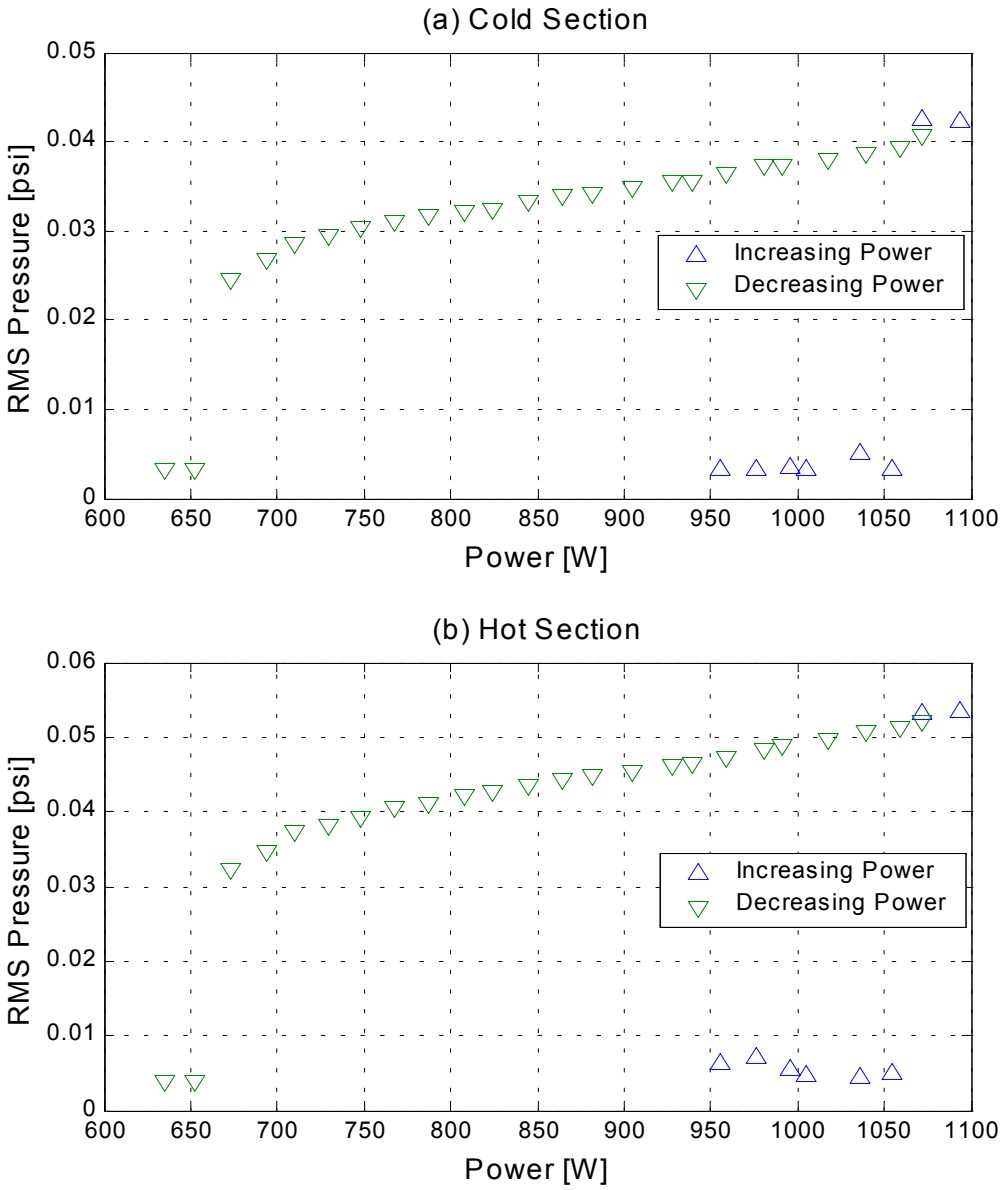

Figure 2-6: Bulk RMS pressures at a mean flow rate of 3.15 g/s.

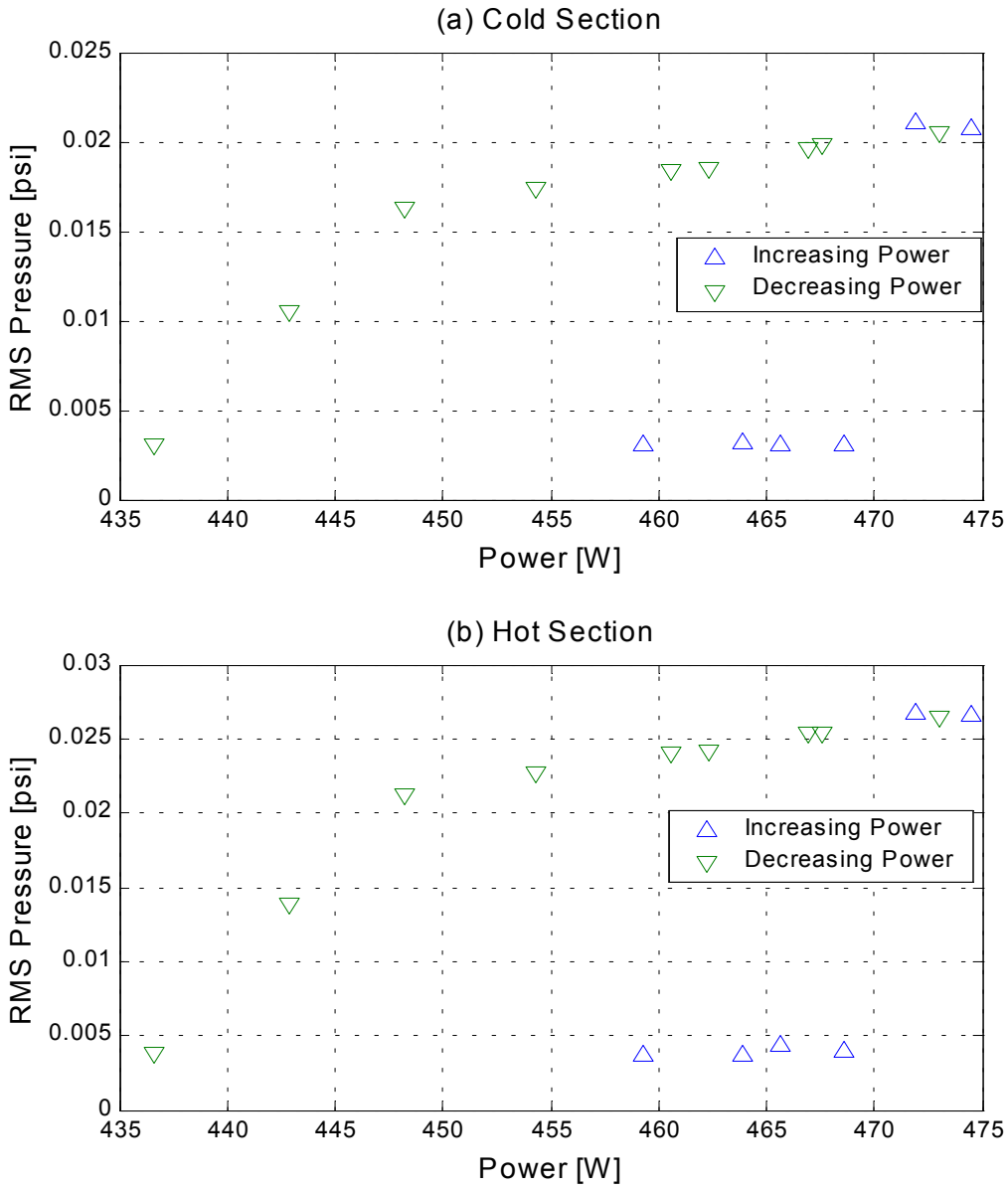

Figure 2-7: Bulk RMS pressures at a mean flow rate of 2.44 g/s.

unstable point has been reached and slightly exceeded, characterized by a sharp increase in pressure amplitudes at approximately 1075 W, the input power is decreased. As the power is gradually decreased, indicated by the downward-pointing triangles, the amplitude of the limit cycle slowly decreases. A large hysteresis loop exists, from approximately 1050 W down to 650 W, when the Rijke tube returns to stable operation. Note, that the amplitude of the pressure oscillations decreases with decreasing power, which could produce uncertainty as to when the system is again stable. Though in this case the transition is well defined, in other cases, such as the one in Figure 2-7, the transition may not be as obvious. At a flow rate of 2.44 g/s, it is not entirely clear whether the data point at approximately 443 W should be classified as stable or unstable. If an additional data point existed at a power level of 440 W, the ambiguity would be even greater.

As stated above, the definition chosen requires analysis of the frequencies produced corresponding to the first mode of the pressure oscillation. Returning to the first example at a mass flow rate of 3.15 g/s, Figure 2-8 and Figure 2-9 show the breakdown of frequencies and pressure amplitudes for the two most dominant modes in the system. It is clear from examination of the first mode, that the system has become unstable at a power level of 1070 W as the power is increased, and has returned to stable operation as the power is decreased at 650 W. In a similar fashion, Figure 2-10 and Figure 2-11 reproduce the same plots for the 2.44 g/s condition. It is now possible to classify the somewhat ambiguous point at a power of 443 W, observed in Figure 2-7. The frequency of the first mode in Figure 2-10 shows that at 443 W the system is still locked to the

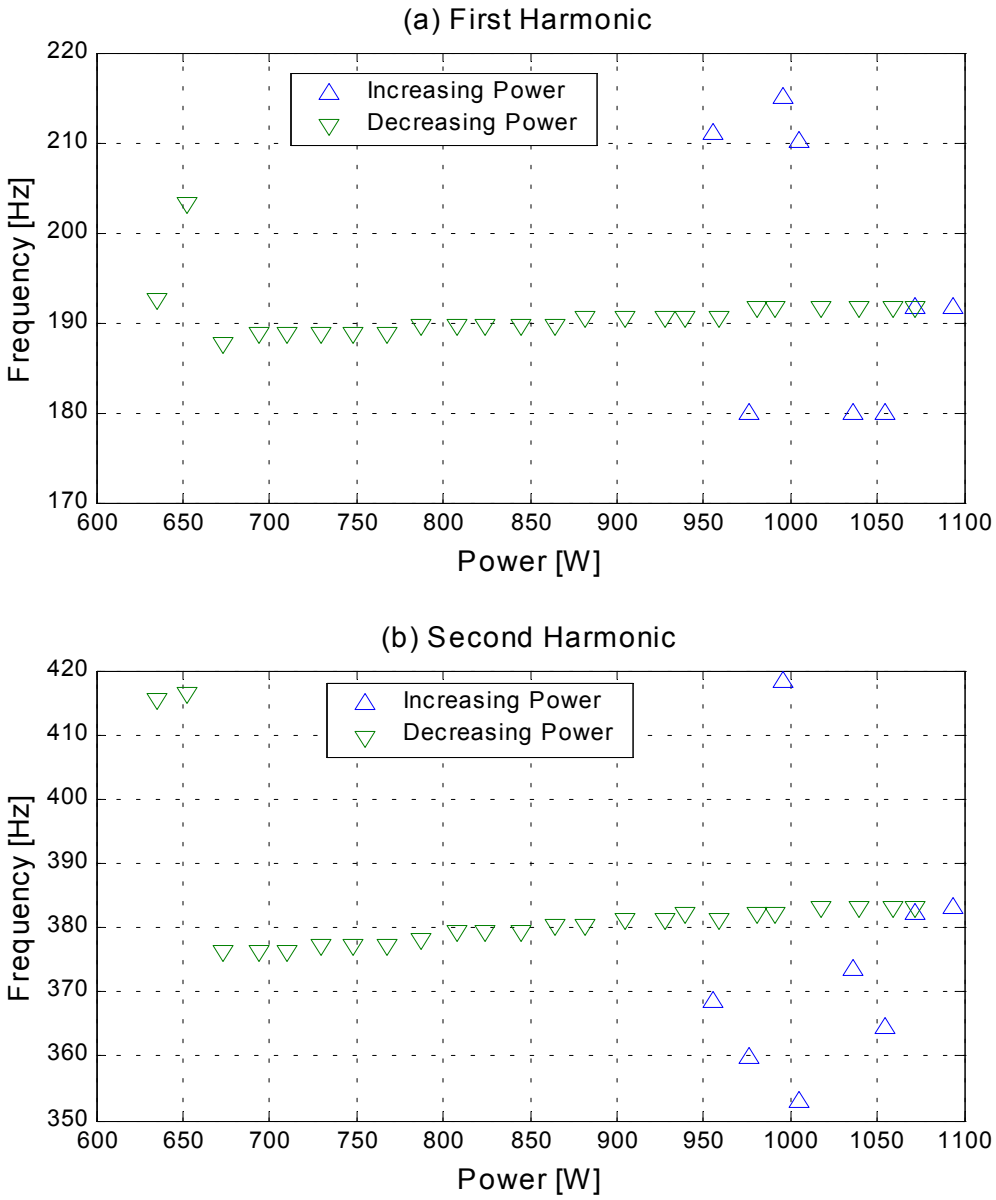

Figure 2-8: Frequencies of oscillations for first two dominant modes at 3.15 g/s.

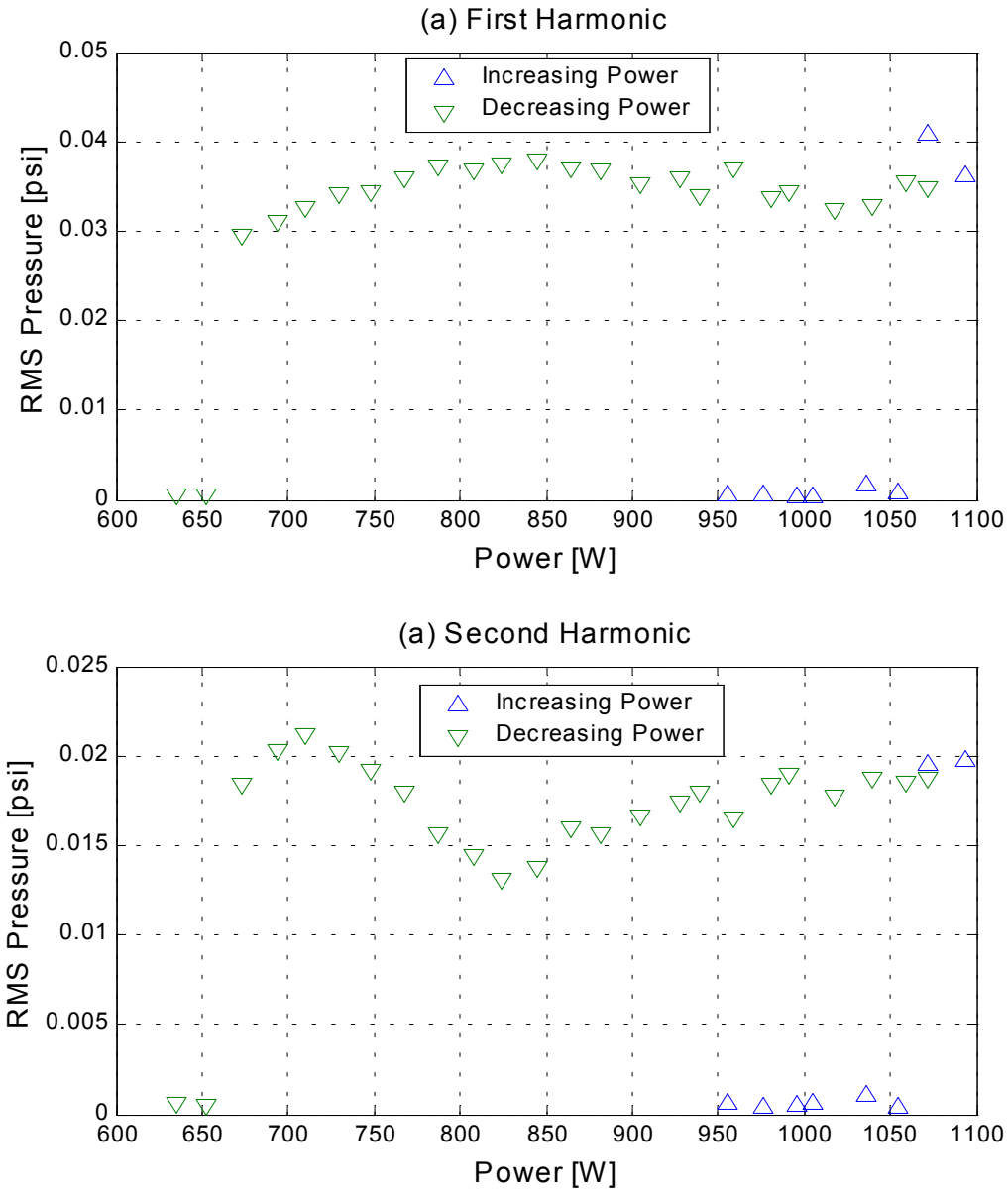

Figure 2-9: RMS pressures of oscillations for first two dominant modes at 3.15 g/s.

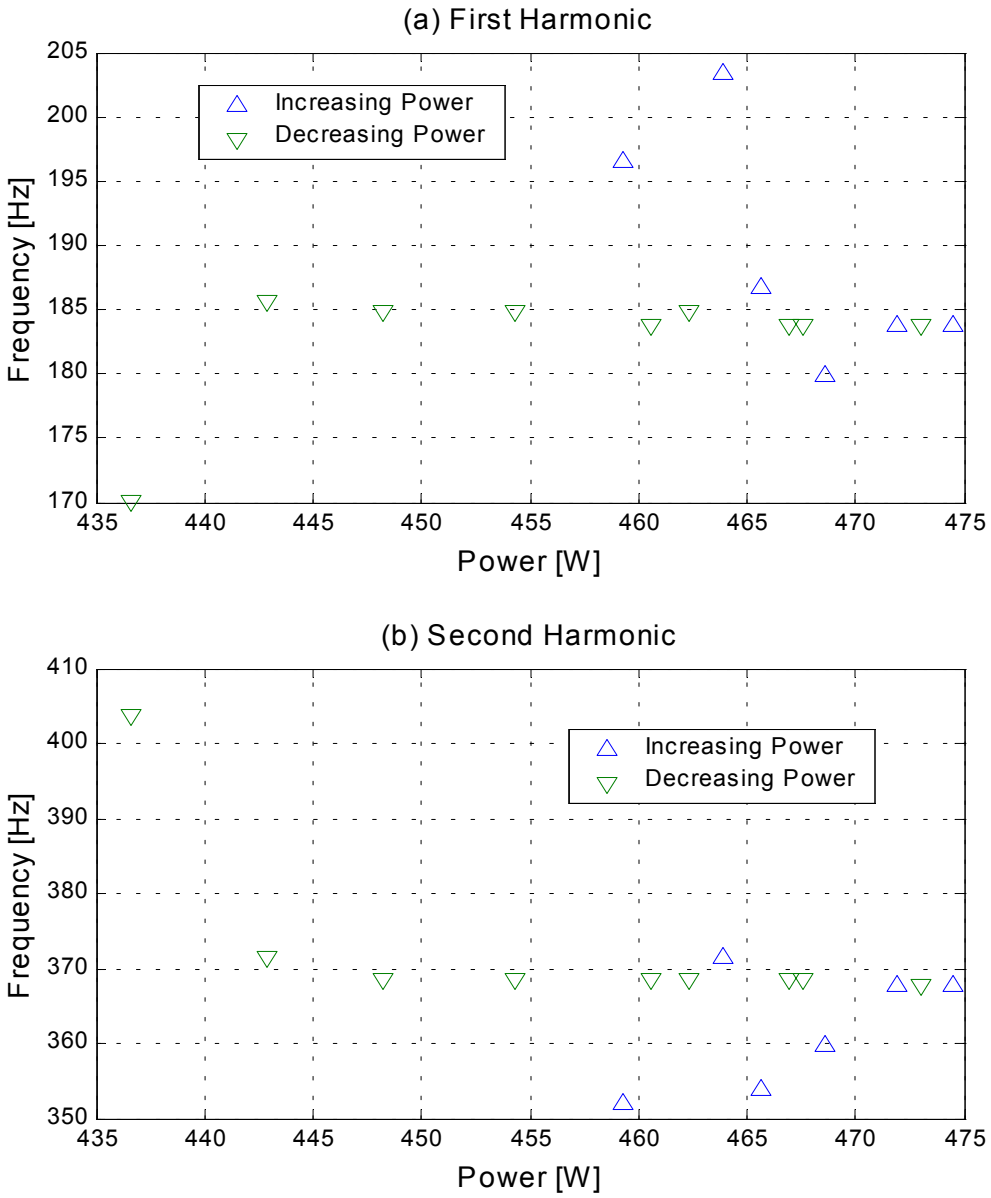

Figure 2-10: Frequencies of oscillations for first two dominant modes at 2.44 g/s.

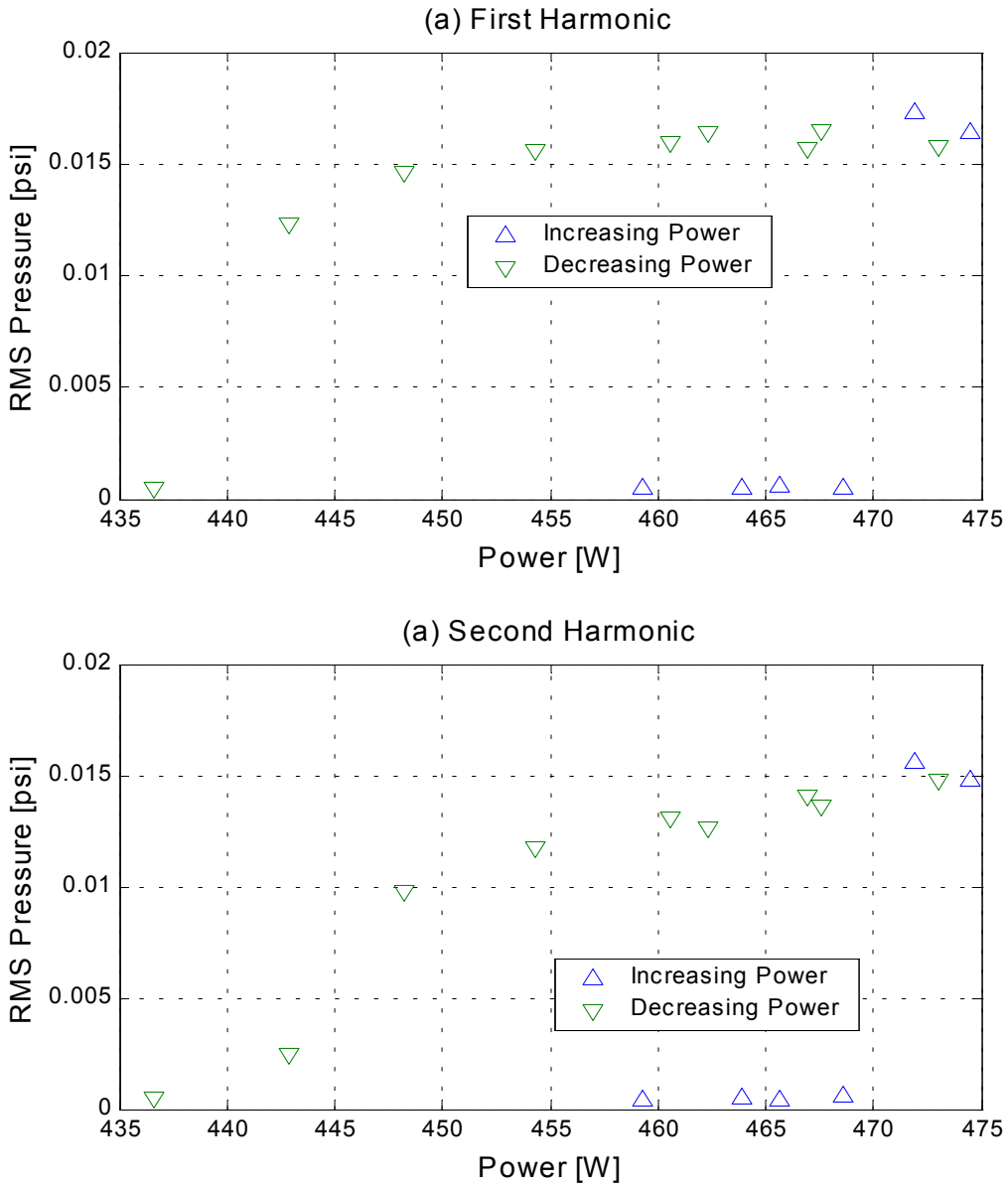

Figure 2-11: RMS pressures of oscillations for first two dominant modes at 2.44 g/s

unstable mode of the Rijke tube. This observation is corroborated by the plot of pressure amplitude (Figure 2-11), which shows that a limit cycle still exists significantly over noise levels at 443 W. It can be reasonably concluded that the system has returned to stable operation at 437 W.

2.3.2 Stability Boundary

The records presented in the previous section show the presence of hysteresis in the Rijke tube system. This however is not always the case. At lower mass flow rates, there is no hysteresis behavior. The results of mapping the stability boundary of the Rijke tube in two dimensions, power and mass flow rate (heater position is left for future work), are summarized in Figure 2-12. Red lines indicate increasing heater power and the point when the system goes unstable. Blue lines indicate the point when the system first returns to stable operation, as the heater power is being decreased.

Errors bars are included, and are taken from the rms values generated during the data collection process. Points below mass flow rates of 0.5 g/s were not taken due to high power requirements coupled with the low flow rates, which produced extremely high grid temperatures and risked overheating various elements of the apparatus. At high flow rates, the experiments were limited by the maximum throughput capacity of the blower.

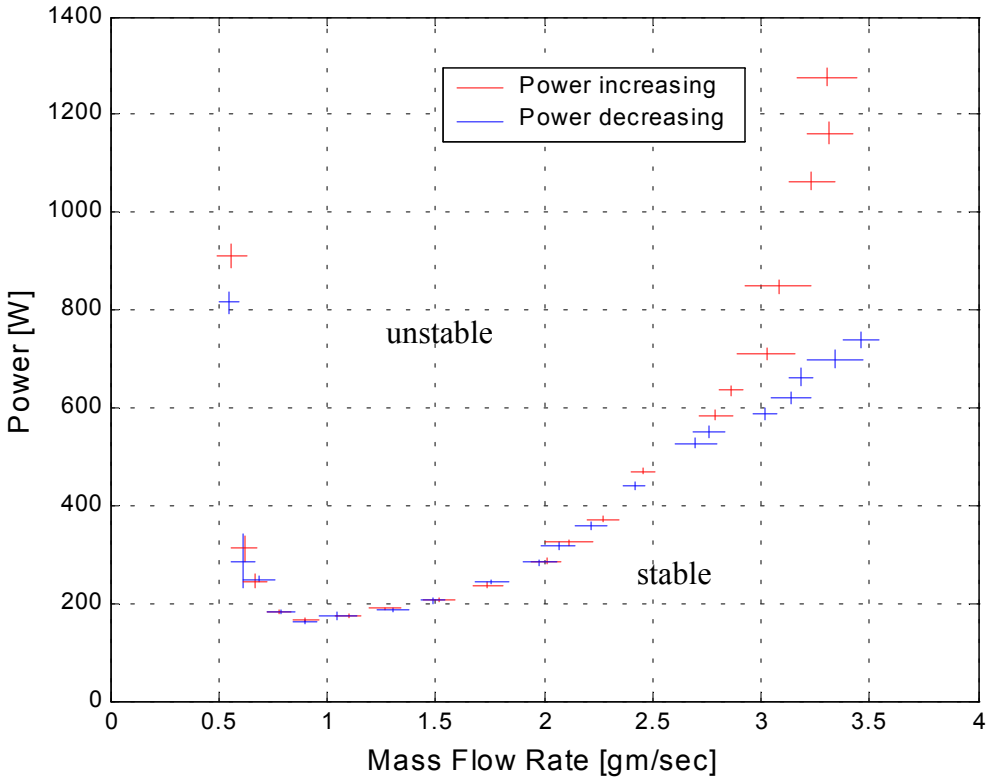

Figure 2-12: Stability boundary for Rijke tube at x/L = ¼.

Of particular interest is the large hysteresis region that appears at mass flow rates greater than approximately 3 g/s. This is most likely due to nonlinearities arising in the acoustics, but may also be partially attributable to transitions to turbulence, postulated by Poncia (1999). Mass flow rates from 3.0 to 3.5 g/s correspond to velocities of 40 to 50 cm/s, and Re_{D_H} (Reynolds number based on hydraulic diameter) in the range of 1200 to 1500. Transitional Reynolds numbers are typically in the range of 2000 to 3000 for normal pipe flows. However, the presence of the grid and frame may trip the system to turbulence earlier. The flow field is further complicated since the flow will not become fully developed in the relatively short (1 m long) tube length. At moderate flow rates,

there is no significant hysteresis beyond the uncertainty present in the experiment. At very low mass flow rates, the extreme slope of the curve also does not appear to contain hysteresis.

2.4 Prediction of the Stability Boundary

A condition for the stability boundary of the Rijke tube can be found by consideration of the energy added and dissipated by the system. Starting with the conservation equations of mass and momentum (equations 1-1 and 1-2) and expanding in terms of small fluctuations, a linearized wave equation with a heat source can be derived assuming a one-dimensional model, with a nearly uniform temperature profile. The linearized wave equation containing a heat source (Maling 1963) and generic linear damping (Howe, 1998) is given by

(2-1) $$p'_{tt}(t,x)+\alpha p'_{t}(t,x)-a^2 p'_{xx}(t,x)=(\gamma-1)\rho\dot{Q}'_{t}(t,x),$$

where p is the sound pressure, ρ is the gas (air) density, γ is the ratio of specific heats, $\dot{Q}$ is the heat release rate per unit mass, α represents generic linear damping, and $(\ )'$ indicates fluctuating quantities. The solution of equation (2-1) is sought as a Fourier expansion of the eigenmodes of the chamber, following the method of Culick (1976).

(2-2) $$\frac{p'}{p_o}=\sum_{n=0}^{\infty}\eta_n(t)\psi_n(x)$$

(2-3) $$u'=\sum_{n=1}^{\infty}\frac{\dot{\eta}_n(t)}{\gamma k_n^2}\frac{d}{dx}\psi_n(x)$$

(2-4) $$\psi_n(x)=\sin\left(k_n\left(x+l_c\right)\right),$$

where the acoustic field has been represented by the modeshape ψ, with a time-varying amplitude, η, and a length correction l_c, has been introduced to compensate for the non-ideality of the node locations of the acoustic mode outside the chamber with respect to the actual length, L. With the assumption of a uniform temperature profile along the tube, the speed of sound is constant and the modeshapes are orthogonal. Considering the simplest case of the existence of only one unstable mode, namely the first mode of the system (n=1), equation (2-1) can be converted from a partial differential equation into an ordinary differential equation. Substitution of equation (2-2) into equation (2-1), multiplying both sides of the resulting equation by $\psi_1(x)$, and integrating over the effective length of the tube, a dynamic equation for the amplitude of the first mode is obtained (indices dropped for convenience)

(2-5) $$\ddot{\eta} + \alpha\dot{\eta} + \omega^2\eta = \frac{\gamma - 1}{p_o}\frac{2}{L + 2l_c}\int_{-l_c}^{L+l_c} \rho\dot{Q}_t'(t,x)\sin(k(x + l_c))dx \,,$$

where k=ω/a represents the wave number.

A common model for the steady heat release in the Rijke tube is that the heat release is coupled to the flow velocity in the system. In a similar way, the unsteady heat release couples with the instantaneous velocity with the addition of a time delay τ (Putnam and Dennis 1954). Due to symmetry considerations, it is evident that the heat release should be independent of the direction of flow, but rather proportional to the magnitude of the flow. It is also assumed that the heat release takes place in an infinitesimally thin region characterized by the location of the heater grid, l_g. With these considerations, the heat release rate per unit mass can be expressed by

(2-6) $$\dot{Q}(t,x) = \frac{P}{\rho S}\sqrt{\left|1+\frac{u'(t-\tau,x)}{u_o}\right|}\delta(x-l_g),$$

where P is the electric power supplied to the grid and S is the cross-sectional area of the Rijke tube. The acoustic velocity of the first mode can be found from equation (2-3), and is given by

(2-7) $$u'(t,x) = \frac{\dot{\eta}}{\gamma k}\cos\left(k\left(x+l_c\right)\right).$$

Since we are interested in determination of the stability boundary, the acoustic velocity can be considered to be much smaller than the mean flow velocity. Linearizing equation (2-6) to form $\dot{Q}'$ and making use of equation (2-7) for the acoustic velocity, the integral on the right-hand side of equation (2-5) can be solved, resulting in

(2-8) $$\ddot{\eta}(t)+\alpha\dot{\eta}(t)+\omega^2\eta(t) = \frac{1}{2\pi}\frac{\gamma-1}{\gamma}\frac{P}{p_o u_o S}\sin\left(2k\left(l_g+l_c\right)\right)\ddot{\eta}(t-\tau)$$

$$= c\ddot{\eta}(t-\tau),$$

where the forcing and damping parameters are represented by c and α respectively. They are assumed to be of low enough magnitude, that they can be considered to be small corrections to the undamped linear oscillator equation. The mode amplitude can be approximately considered to vary harmonically in time, with a growth parameter A yielding

(2-9) $$\eta(t) = A\sin(\omega_n t).$$

Making use of equation (2-9), the energy dissipated per cycle is

(2-10) $$W_d = \int_0^{2\pi/\omega} \alpha \dot{\eta}(t)\dot{\eta}(t)dt = \alpha\omega A^2\pi \,.$$

Similarly, the energy added to the acoustic mode per cycle is given by

(2-11) $$W_a = \int_0^{2\pi/\omega} c\ddot{\eta}(t-\tau)\dot{\eta}(t)dt = c\omega^2 \sin(\omega\tau)A^2\pi \,.$$

The condition for the onset of instability occurs when $W_a > W_d$. Comparing equations (2-10) and (2-11) and using equality of W_a and W_d to indicate the stability boundary, the system first goes unstable when

(2-12) $$\frac{1}{2\pi}\frac{\gamma-1}{\gamma}\frac{P}{p_o u_o S}\sin\left(\frac{2\pi(l_g+l_c)}{L+2l_c}\right)\sin(\omega\tau) \geq \frac{\alpha}{\omega} \,.$$

Taking into account damping in wall boundary layers (other losses typically have negligible contributions), the losses are modeled classically by (Howe, 1998)

(2-13) $$\frac{\alpha}{\omega} = \frac{L}{R}\sqrt{\frac{2}{\pi}}\frac{\left(\sqrt{\nu}+(\gamma-1)\sqrt{\chi}\right)}{\sqrt{aL}},$$

where χ is the thermal diffusivity, ν is the kinematic viscosity, and R is the tube radius. Thus we arrive at

(2-14) $$\frac{1}{2\pi}\frac{\gamma-1}{\gamma}\frac{P}{p_o u_o S}\sin\left(\frac{2\pi(l_g+l_c)}{L+2l_c}\right)\sin(\omega\tau) \geq \frac{L}{R}\sqrt{\frac{2}{\pi}}\frac{\left(\sqrt{\nu}+(\gamma-1)\sqrt{\chi}\right)}{\sqrt{aL}},$$

which is an explicit criterion for instability involving all relevant parameters: supplied power, mean flow velocity, grid location, natural frequency, time delay, system geometry and fluid properties.

Note that the time delay τ is generally found from previous experiments and simulations, to be less than a quarter of a period, so the phase $\omega\tau$ can be considered to lie between 0 and $\pi/2$. Several observations can be drawn from equation (2-14).

- A necessary condition for instability is the location of the grid in the first half of the tube (in accordance with Rayleigh's criterion).
- No limit cycle is possible using a linear stability analysis.
- In the limits $u_0 \to \infty$ or $P \to 0$ with the other parameters fixed, the system is stable.
- In the limit as $P \to \infty$ the system is unstable.

The limit $u_0 \to 0$ cannot be analyzed with this approach, since it violates the initial assumption that the acoustic velocity is a small fluctuation imposed over the mean flow. It is evident that a stability diagram with flow velocity and power input as the variable parameters will result in a linear relationship. However in reality, the time delay and amount of energy transported to the acoustical mode are not constant, so that the exact stability boundary may not be predicted by equation (2-14).

2.5 Comparison of Prediction with Experimental Results

In order to reconcile the model of the previous section with experimental results, a better model must be constructed for the heat release, which takes into account the time delay and change in heat transfer characteristics at low flow rates. Kwon and Lee (1985) performed numerical simulations to compute the heat transfer from an isothermal wire to an acoustic wave. They define an efficiency factor, *E*, resulting from their simulations, which relates the amplitude of the heat release and phase delay as a function of non-

dimensionalized mean flow velocity, $u_o^* = u_o / \sqrt{\omega\chi}$, and heater wire radius, $r^* = r\sqrt{\omega / \chi}$. Transforming equation (2-14) for use with the model of Kwon and Lee, the efficiency factor can be defined as

(2-15)
$$E = \frac{R}{2u_o}\sqrt{\frac{a}{\pi L}}\sin(\omega\tau)$$

and is plotted for r^* = 1.0 in Figure 2-13.

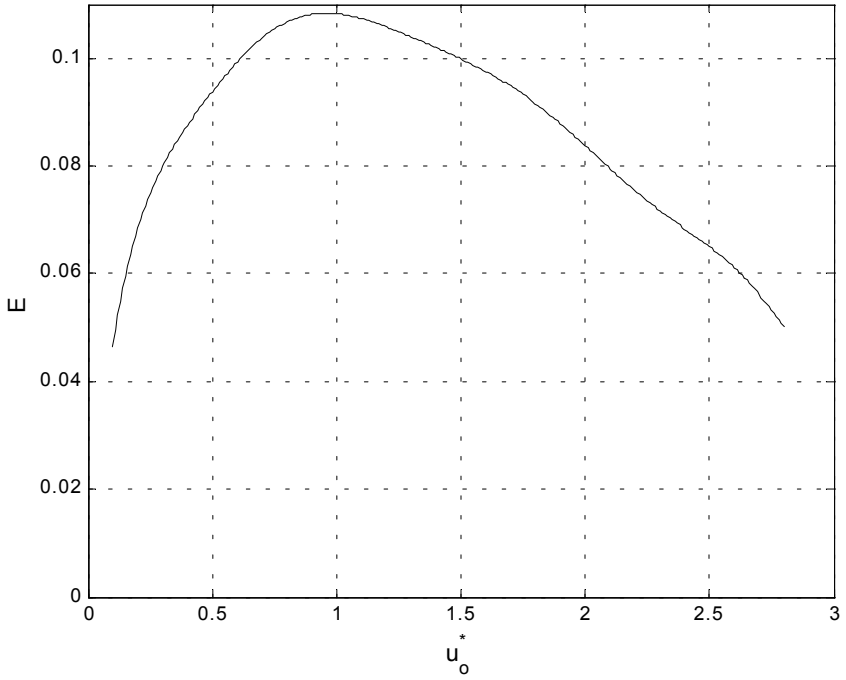

Figure 2-13: Efficiency factor, *E*, for r^* = 1.0.

Recall the assumption that the temperature is approximately uniform in the tube. Temperature selection affects the physical properties of the air, which in turn changes the scaling of the non-dimensional parameters. Two mean temperatures were selected,

which are representative of the low and high range of temperature in the tube. For the experimental conditions used, r^* varies from approximately 0.5 at 600K up to 1.0 at 300K. The difference in the efficiency curve for r^* between 0.5 and 1.0 is very small, so only the efficiency factor for $r^* = 1.0$ is considered.

The resulting stability boundary is plotted in Figure 2-14 for both temperatures. Qualitatively, the predicted curves show the correct shape, but fail to accurately predict

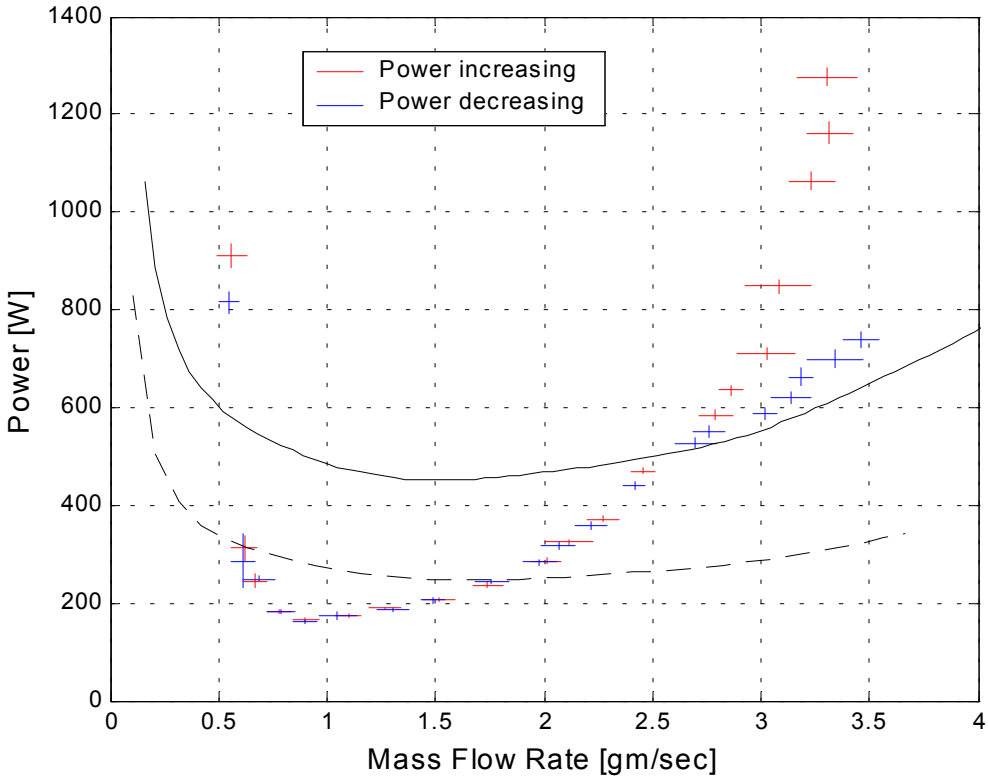

Figure 2-14: Stability boundary prediction. Solid black line is for T = 600K, and the dashed black line for T = 300K.

the stability boundary. It can be argued that the lower temperature curve is more suitable for low power inputs, but it still over-predicts the power required to cause instability. In general, the model over-predicts power requirements at low flow rates, and under-predicts power requirements at higher flow rates.

2.6 Summary

The experimental apparatus and approach for collecting a set of accurate measurements that characterize the Rijke tube have been presented. The experiment is capable of capturing both steady-state and transient behavior, spanning the relevant parameters (mass flow rate, heater power input, and heater position) over a wide range of values. In addition, bulk temperature profiles are collected along the centerline of the tube, which have not been measured previously. Experimental results show the presence of hysteresis at high mass flow rates (above 3 g/s). A stability curve is presented summarizing the stability characteristics of the Rijke tube, with the heater at a position of $x/L = ¼$.

A one-dimensional model using linear acoustics is used in conjunction with numerical heat transfer results from Kwon and Lee (1985) to attempt to predict the stability boundary. It is based on the physical parameters of the experiment, and is not limited to this configuration only. The results agree qualitatively, although accurate prediction of the stability curve was not achieved. It is evident that a more detailed model, involving

- an accurate heat transfer model including radiation
- fluid mechanical considerations
- at least two-dimensional, possibly three-dimensional effects
- nonlinear acoustics and multiple acoustic modes

will be necessary to predict accurately the limit cycle amplitudes and stability characteristics of the Rijke tube.

Chapter 3
Full-Scale Flare and Sub-Scale Model

This chapter describes a practical, industrial application of a device exhibiting characteristics similar to a Rijke tube, namely a large flare. A description of the device and the data collected on site is contained in this chapter. This chapter also describes the sub-scale design and modeling efforts, as well as the results that were obtained. Ultimately, this motivates the more advanced diagnostic techniques that were employed in Chapter 4.

3.1 Full-Scale Flare

3.1.1 Introduction

One of the nations largest landfill sites, local to Caltech, uses a pair of large flares to burn off its production of landfill gas. As solid waste material decomposes, landfill gas is collected by a system of gas wells, trenches, and collection pipes. A portion of the landfill gas (composed primarily of methane and carbon dioxide) is used to power a 50 MW power plant and on-site vehicles. The remainder is sent to the flare station, shown in Figure 3-1, to be burnt under controlled conditions, minimizing emission of unburnt hydrocarbons (UHC), NO_x, and other undesirable pollutants.

This particular landfill site receives in excess of 12,000 tons of solid waste per day. As the decomposition rates are anticipated to continue to increase, so will the production of

Figure 3-1: Landfill flare station.

landfill gas. In anticipation of increased capacity requirements, each flare is designed to process landfill gas at a maximum rate of 5500 SCFM. However, at approximately 50% of maximum capacity, the flares emit a low frequency rumbling, which disturbs local homeowners. This acoustic, low frequency noise is a result of the flares being unstable.

3.1.2 Description of Full-Scale Flare

The flare can be considered to be a type of Rijke tube, with closed-open boundary conditions, versus the Rijke tube's open-open boundary conditions. Each flare stands at a height of 45 feet, with an inner diameter of 12 feet. The burner inside the flare consists of an array of 180 fuel spuds (see Figure A-2 for more details) distributed evenly on ten welded straight lengths of 12-inch steel pipe. Each spud is 4.5 inches in height with an inner diameter of 0.688 inches. The tops of the spuds extend to a height of 5.7 feet relative to the ground. Landfill gas exits the spuds into a burner block section, which extends to a height of 8.8 feet relative to the ground. The burner block contains an eductor section, which accelerates the flow and allows it to jet-mix with entrained air.

Air enters the flare through two sets of horizontal louvers, located on opposite sides at the bottom of the flare. The smaller louver is 3 feet high by 3 ¼ feet wide, while the larger louver is 4 feet high by 7 feet wide. During the tests undertaken on-site, analysis of the landfill gas mixture showed 40% methane, 33% carbon dioxide, and the balance made up of nitrogen and trace gases (Bjerkin, 1999).

3.1.3 Diagnostics

In order to characterize the flare system, sets of instrumentation arrays were designed to slide into access ports in the side of the flare and on the gas feed line. Each instrumentation pair consisted of a pressure transducer (RE Technologies, Model PTX1) recessed to prevent damage from high temperatures and a type-K thermocouple. The

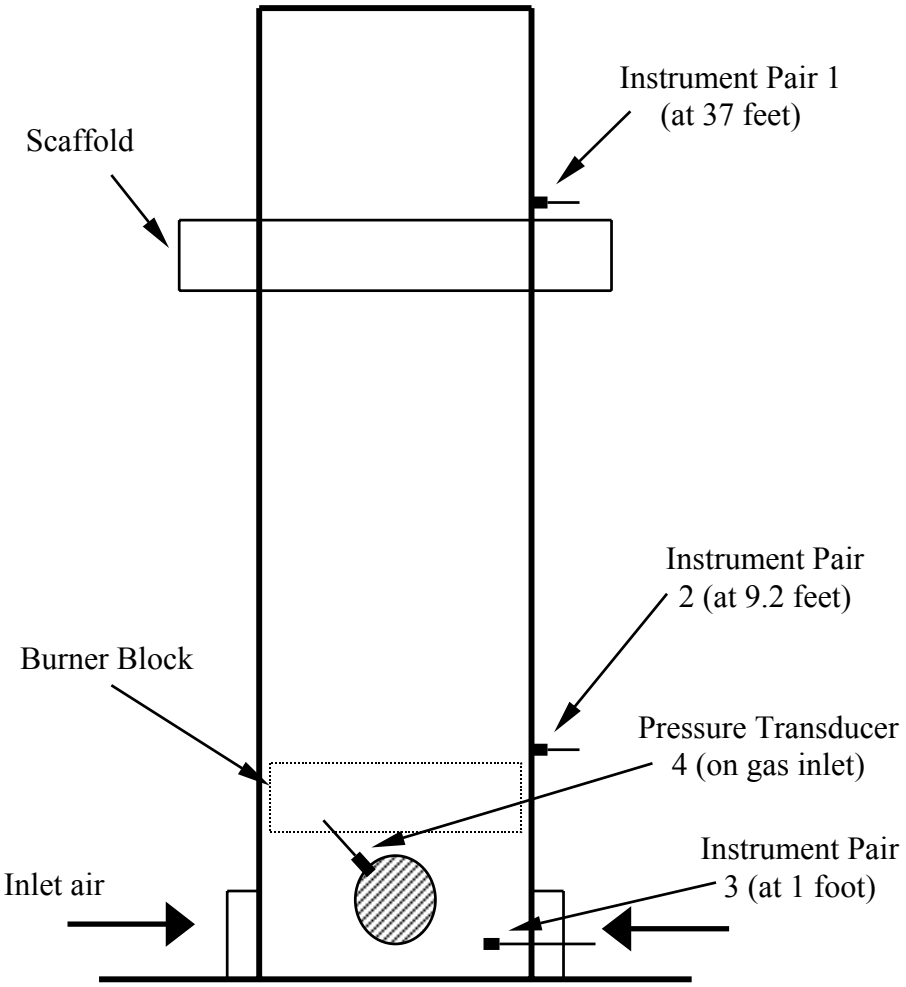

Figure 3-2: Instrumentation layout on full-scale flare.

thermocouples extended approximately 2 feet into the chamber. The pairs were located at heights of 37 feet, 9.2 feet, and 1 foot, labeled 1, 2, and 3 respectively. An additional pressure transducer was located on the gas inlet line and is referred to as transducer 4. Data was acquired on site with a Computer Boards CIO-DAS1602/12 data acquisition board and a CIO-EXP16 expansion board for the thermocouples, both installed in a Pentium II 400 MHz computer. Pressure data was acquired at 1 kHz, while temperature data was multiplexed and acquired at 2 Hz. A diagram showing the instrumentation on the flare and a few of the flare's physical characteristics is shown in Figure 3-2.

3.1.4 Results

The flare was run at mass flow rates of 2500-3100 SCFM. The data presented here is for the 3100 SCFM flow condition, since it is the highest mass flow condition tested and is representative of the system instability. Fuel composition was approximately 40% methane and 33% carbon dioxide with a balance of nitrogen and trace gases. The temperature distribution at the three data ports is shown in Figure 3-3. This represents the bulk temperature in the flare, since the time constant of the thermocouples is too large to respond to acoustically driven temperature fluctuations. The large jump in temperature at 9.2 feet is due to the presence of the burner block section just below this data port (Figure 3-2).

Pressure data taken from the site is shown in Figure 3-4, for each of the four measurement locations. This data has been low-pass filtered with a cutoff frequency of 200 Hz to remove any high frequency noise. Note the lower amplitudes of the oscillations for Pressures 1 and 3, since Pressure 1 is situated near the top of the tube

(atmospheric boundary condition), and Pressure 3 is located at the bottom of the tube. Even though there is an acoustically "solid" boundary at the bottom of the flare, the presence of the open louvers introduces a mixed boundary condition, at least with respect to the pressure transducer, which only penetrates 2 feet into the chamber through the bottom louver. Pressure 4, located on the gas inlet line, is similar to Pressure 2, even though there is the burner section in between the two transducers. The pressure traces show these positions to be of similar amplitude and qualitatively, to follow the same pattern.

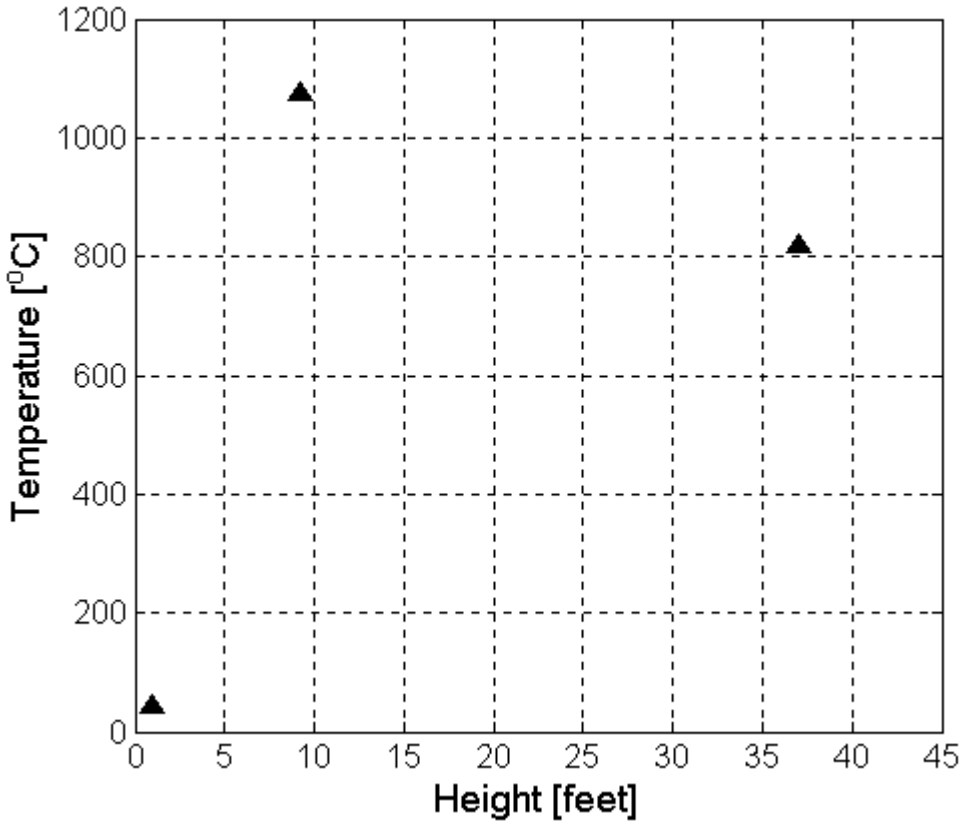

Figure 3-3: Flare bulk temperature profile.

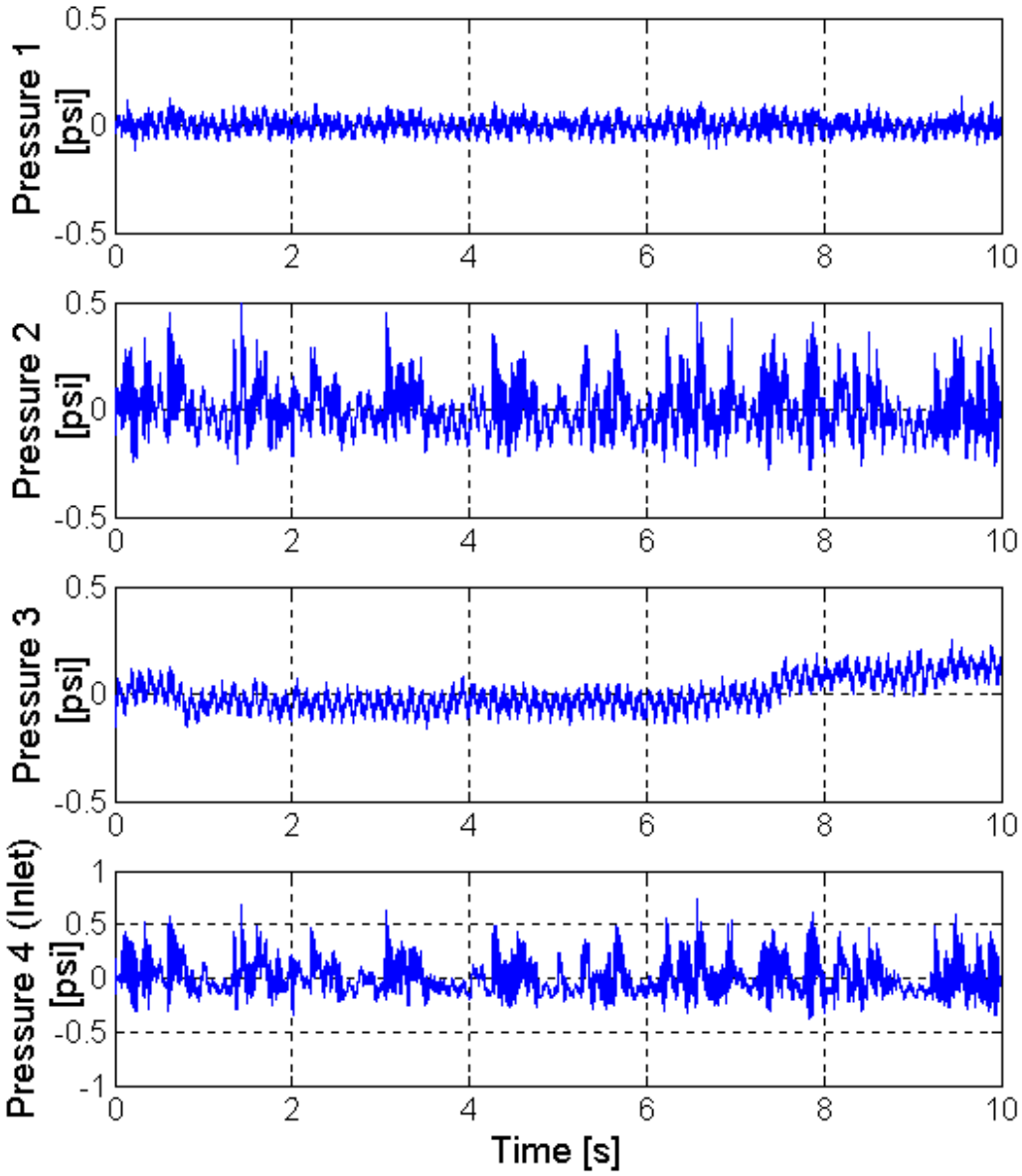

Figure 3-4: Flare pressure traces (low pass filtered at a cutoff of 200 Hz).

FFTs for the pressure traces are shown in Figure 3-5. They indicate peaks at approximately 8.6 Hz and 21.5 Hz, corresponding to the first and second modes of a closed-open acoustic system.

Making use of the FFT results, the pressure traces can be selectively bandpass filtered about their most prominent frequencies. A 6th order butterworth phase-preserving bandpass filter is applied to the pressure data about the first and second acoustic modes of the system, and displayed in Figure 3-6 and Figure 3-7 respectively. Figure 3-6 clearly shows all pressures to be in-phase, as would be expected for a quarter-wave (the 1st mode of an open-closed system). Corresponding to this result is the bandpass filtered data for the 2nd mode. Figure 3-7 indicates that Pressure 1 and Pressure 2 are generally speaking in-phase, which suggests that the pressure node of the 2nd mode occurs somewhere below Pressure 2. Pressure 3 is out-of-phase with the pressures in higher sections of the flame, as expected, with the inlet Pressure 4 again mirroring what is seen at Pressure 2.

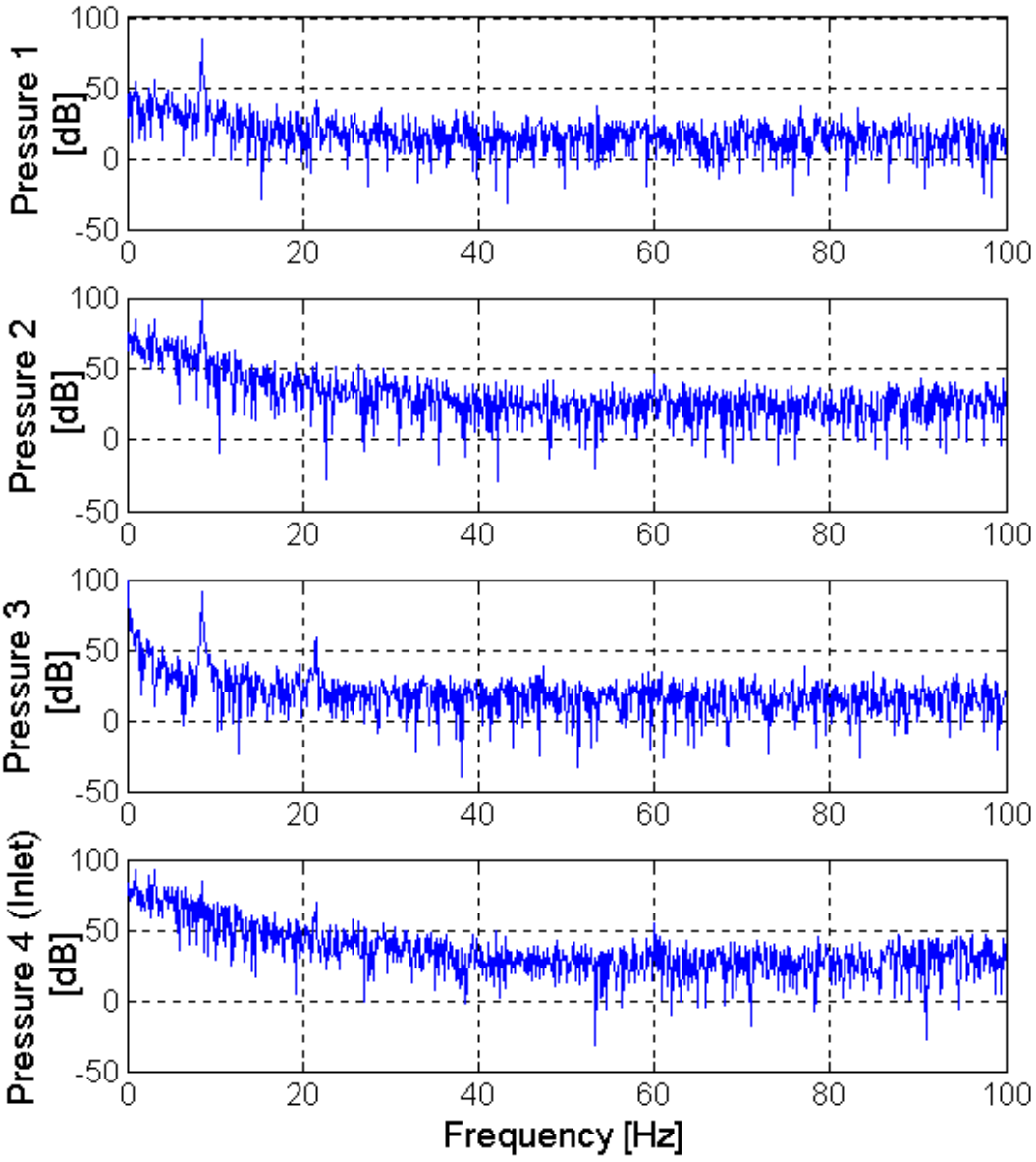

Figure 3-5: FFT of pressure traces in full-scale flare.

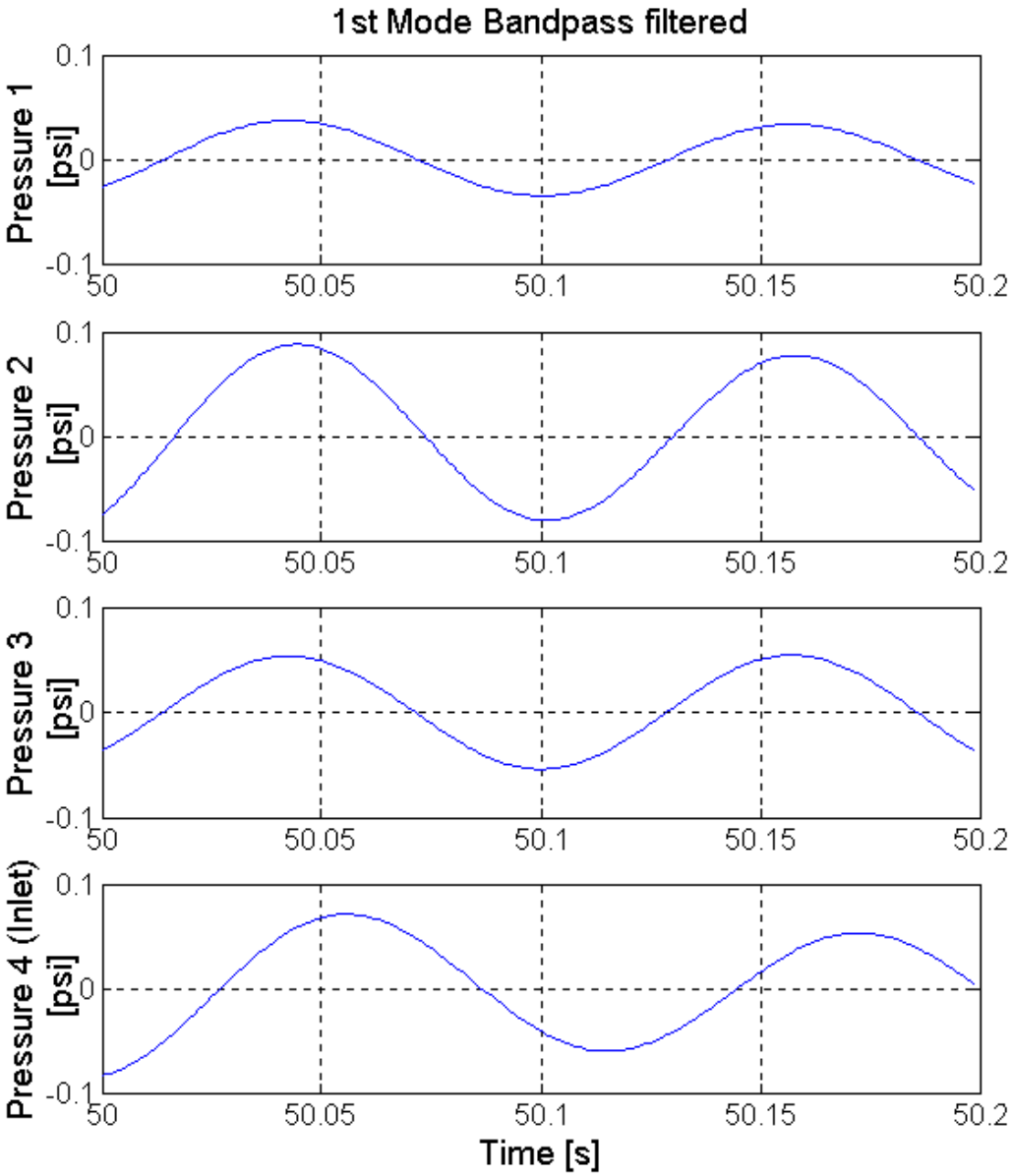

Figure 3-6: Flare pressure traces, filtered using a 6th order butterworth phase-preserving bandpass filter between 7-10 Hz (1st mode).

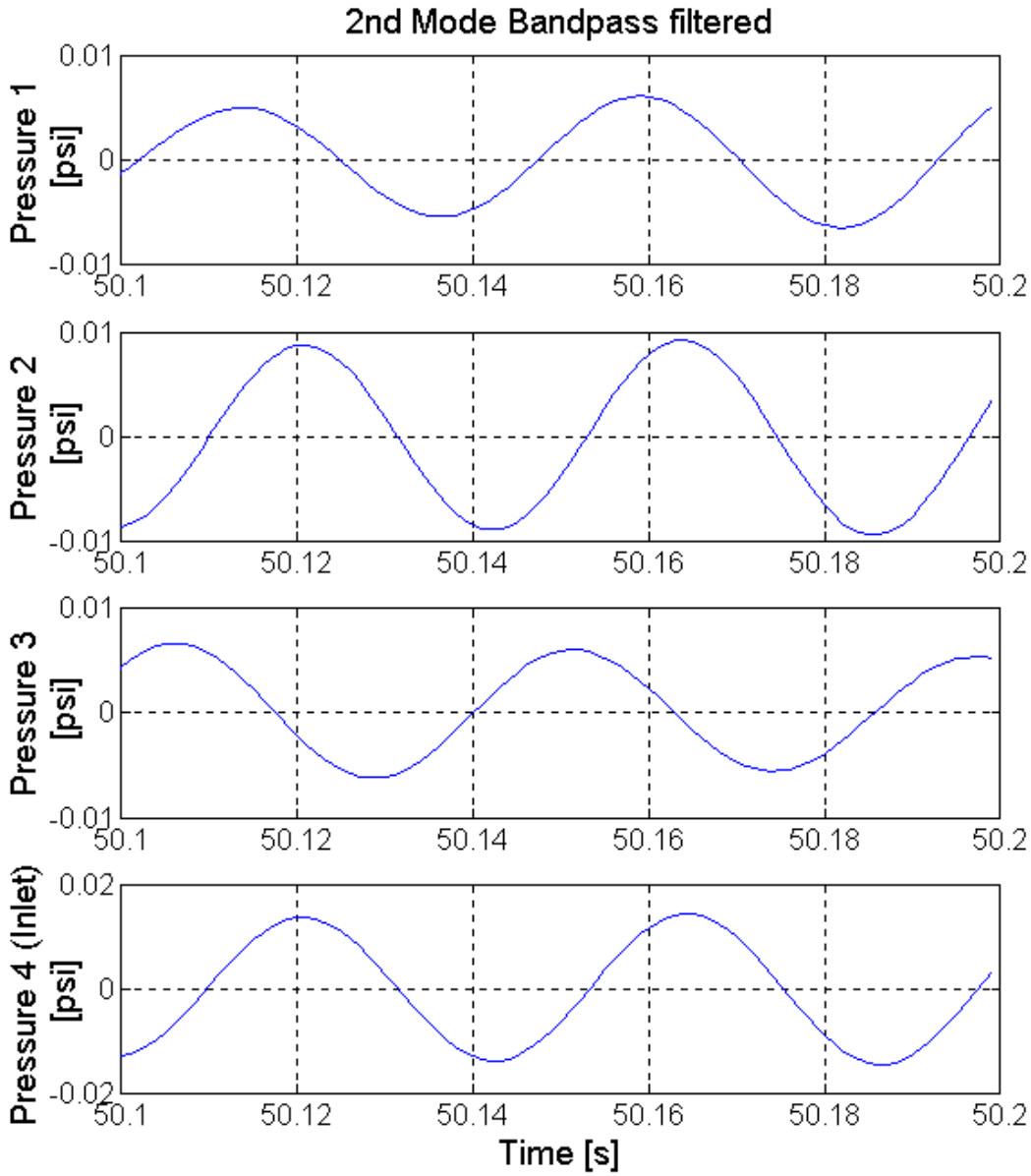

Figure 3-7: Flare pressure traces, filtered using a 6th order butterworth phase-preserving bandpass filter between 21-24 Hz (2nd mode).

3.1.5 Possible Driving Mechanisms

There exist a number of potential mechanisms that could be driving the flare towards instability. These may be working independently or acting in concert to exceed the natural losses associated with the flare system. They can be summarized as follows:

- Indirect Energy Transfer: Combustion induced buoyancy creates the draft of air; air flowing past physical edges causes vortex shedding that then excite acoustic waves. This is analogous to the operation of wind instruments or sirens.
- Feed System Coupling: Fluctuations of pressure and/or velocity in the fuel supply system and in the air flow through the louvers cause fluctuations of the fuel/oxidizer mixture ratio, which then cause fluctuations in the energy release that further pump the acoustic resonance.
- Chemical and/or Heat Transfer Sensitivity: Combustion processes in the burners are sensitive to pressure and velocity fluctuations, producing an internal feedback path which causes the combined system (burner and flow dynamics) to be linearly unstable.

Attempts to clarify which mechanism is responsible for the instability through sub-scale modeling of the system are detailed in the next section.

3.2 Sub-Scale Flare Model

3.2.1 Apparatus and Diagnostics

A 1/12th sub-scale model of the flare was designed and constructed, in an attempt to characterize the acoustic properties of the chamber and its interaction with the burner, and is shown fully assembled in Figure 3-8. The model consisted of a 12.5-inch diameter

quartz tube, 42 inches in length, with six ½-inch laser drilled holes along one side for instrumentation access. The quartz tube rests inside an aluminum base assembly that has front and back cutouts to simulate the louver action of the full-scale flare. The aluminum base and quartz tube together form the chamber section, shown in Appendix A, Figure A-1.

The corresponding burner section is shown in detail in Figure A-2. It is comprised of eight lengths of 1-inch diameter aluminum tubing, welded together to form the inlet feed system of the burner. There are five spuds on each length of tubing, which serve to provide fuel. The burning region, which occurs above the two rings, is shown in the Section A drawing of Figure A-2. These two rings form the "eductor" section of the burner, which was only approximately modeled in this apparatus and will be explored further in the next chapter.

The data acquisition system used on the sub-scale flare was essentially the same as that on the full-scale flare, though the specific transducers differed. The type-K thermocouples (Omega KMQSS-062U-6) and pressure transducers (PCB 112A04 with 422D11 charge amplifiers) were mounted in water-cooled instrumentation bosses (Figure A-3) that attached to the quartz tube through the laser drilled instrumentation ports.

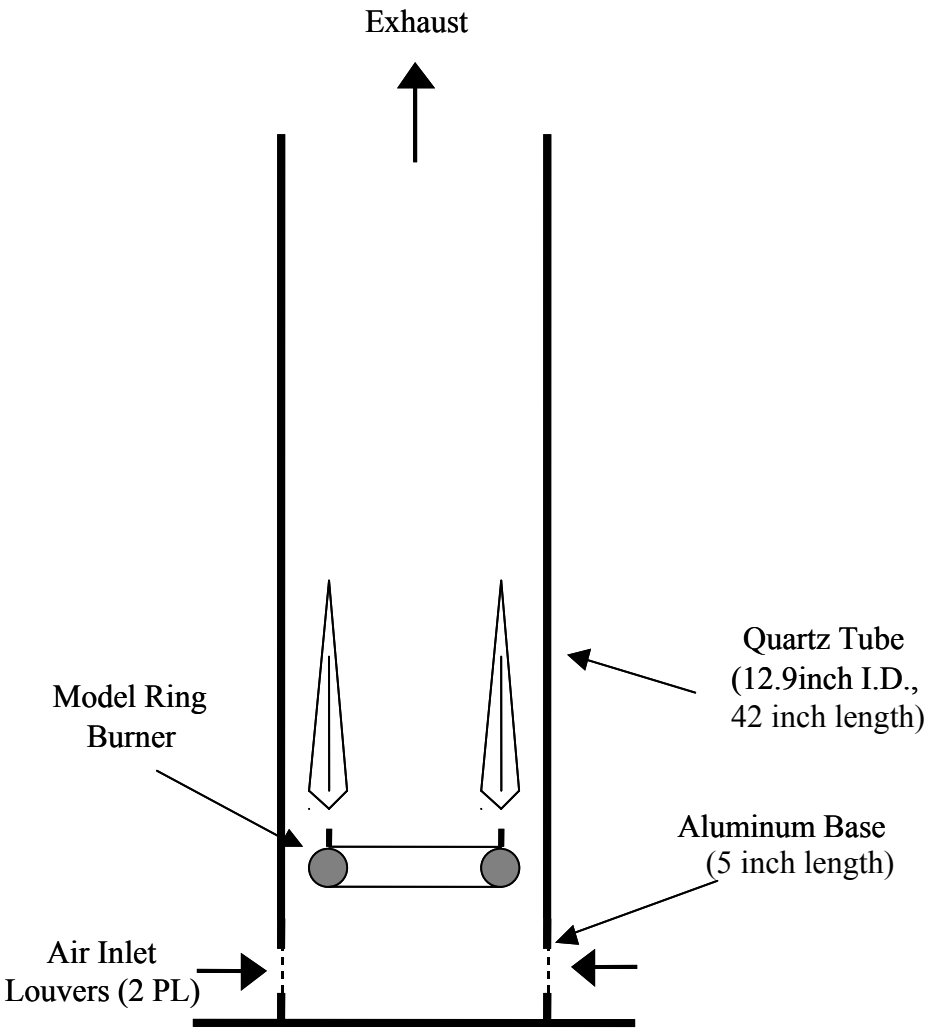

Figure 3-8: Schematic of sub-scale flare model assembly.

3.2.2 Scaling of the Model

The first step in characterizing the sub-scale flare model was an attempt to operate it in an unstable regime. A wide variety of conditions were experimented with to elicit oscillations from the model including:

- Diffusion flames
- Premixed flames
- Single and double meshes above the burner spuds
- Raising the burner from its natural position to x/L = 1/3 up to x/L = 1/2
- Running with and without burner "shields"
- Placing a mesh over the shields
- Doubling the chamber length by adding a stainless steel extension tube
- Secondary fuel pulsed injection

The strategy behind most of these techniques was to increase the intensity of heat release in a region that would be favorable to drive an acoustic instability according to Rayleigh's criterion. Switching from a diffusion to a premixed flame and using meshes both serve to concentrate the heat release in a more localized region. If the heat release is distributed too evenly, regions of strong damping will be created that will cancel out driving regions. Raising the position of the burner placed the heat release in a geometrically more favorable position for the excitation of the 2nd mode. This did not induce oscillations, hence, changes were next applied to the chamber geometry rather than just the burner.

Doubling the chamber length served two purposes – to lower the fundamental frequency of the system, as well as increasing the aspect ratio, L/D. This is significant due to the scaling of the acoustic radiative losses out the open end of the chamber. According to Clanet et al. (1999), the characteristic time for radiative damping can be given by

(3.1)
$$\frac{1}{\tau_{rad}} = \frac{(\omega D)^2}{8aL},$$

where ω is the acoustic frequency, D is the chamber diameter, a is the speed of sound, and L is the chamber length. The acoustic radiative losses are proportional to ω^2/L. Increasing the chamber length by a factor of 2 correspondingly decreases the fundamental frequency by a factor of 2. Therefore, a doubling of the chamber length results in an eight-fold decrease in acoustic radiative losses. Similarly, Clanet et al. (1999) show that diffusive losses due to the presence of viscous and thermal boundary layers at the lateral walls are proportional to $\omega^{1/2}$. As a result, lowering the fundamental frequency will also lower acoustic diffusive losses.

Another technique that was tested was to inject secondary fuel into the system, using an automotive fuel injector. Secondary fuel injection was superimposed over the main fuel feed, so the system was subjected to a mean fuel flow rate with a fluctuating component. The objective was to enhance natural resonant frequencies, by providing small-scale disturbances that would hopefully be further amplified as the instability developed into a limit cycle. This concept had physical relevance, since the landfill gas entering the fuel-scale flare would have a varying fuel composition and thus a fluctuation in fuel flow rate.

None of the mentioned techniques were successful in generating a "naturally" self-sustained limit cycle behavior in the sub-scale flare model. The most promising technique was secondary fuel injection coupled with the extended chamber length, producing measurable pressure oscillation in the chamber at 130 Hz. This case, however, was deemed to be too artificial, since the amplitude of the fluctuating fuel flow rate was of the same order as the mean flow rate. As a consequence, any attempts to stabilize the sub-scale model would not be relevant to the full-scale flare.

3.3 Conclusions

Measurements taken of the full-scale flare operating in its unstable regime indicate the presence of modes at 8.6 Hz and 21.5 Hz. This corresponds well to the natural first (1/4 wave) and second (3/4 wave) modes that would arise in a closed-open system. The frequencies do not match precisely due to changes in the speed of sound due to temperature gradients in the chamber. The pressure amplitudes do not correspond completely to a closed-open system, since at the closed boundary the presence of louvers produces a mixed boundary condition. Although the bottom of the flare is closed acoustically to a longitudinal mode, the louvers open the bottom of the flare to the atmosphere, greatly dampening the amplitude of the pressure oscillations.

The sub-scale model of the flare was unsuccessful at developing self-sustained pressure oscillations. This was due in large part to the distributed nature of the heat release (approximately over an 18 inch high region) in the model, compared to the relatively concentrated heat release that occurs in the flare. Another factor was the acoustic losses due to changes in the frequencies being studied. Artificial pumping of the acoustic

modes in the sub-scale model was achieved using a fuel injector; however, this would not be useful in a study to suppress oscillations in the full-scale flare. It therefore becomes necessary to take a closer look at the dynamics of the flame in order to improve its stability characteristics.

Chapter 4
Chemiluminescence Measurements

This chapter describes the methods used to visualize a flame under an acoustically forced pressure field. It relates to Chapter 3 in that the burner configuration is modeled after an individual spud from the flare and is motivated by a need for a more fundamental understanding of combustion dynamics in flames in unstable systems. The flowfield is imaged using two different techniques: shadowgraph and chemiluminescence. IN addition, chemiluminescence gives a measure of the heat release rate in the flame. Details regarding the experimental setup and diagnostics are also provided in this chapter.

4.1 Experimental Setup

The test section, shown in Figure 4-1, consists of three major components: the acoustic driving system; the acoustic cavity; and the burner section. It is based in part on the sub-scale model of the flare burner, discussed in Chapter 3.

4.1.1 Acoustic Driving System

The acoustic driving system is mounted above the acoustic cavity on the outer quartz tube. It consists of a large tubular stainless steel section in the shape of a cross, approximately 12 inches in diameter, which extends the overall length of the acoustic chamber an additional 24 inches. The exhaust section is open to the atmosphere, providing an acoustically open exit condition. A pair of acoustic drivers are sealed to a pair of air jet film cooling rings (to prevent failure of the drivers), which are in turn sealed to opposite sides of the steel structure. The acoustic drivers are 12 inch subwoofers (Cerwin-Vega model Vega 124), with a sensitivity of 1 W @ 1 m of 94 dB, and a continuous power handling capacity of 400 W. A 1000 W power amplifier (Mackie M1400i) and a function generator (Wavetek 171) provide the power and signal to the acoustic drivers. Significant power is required to provide reasonable amplitude pressure oscillations. The amplitude of the fundamental driving mode is actively controlled by custom-designed electronics (see section 4.3.4), which measure the pressure in the acoustic chamber at the burner with a pressure transducer (PCB 106B50), and appropriately scale the power output of the speakers. The signal from the transducer is notch-filtered to ensure the intended driving mode is correctly amplified or attenuated.

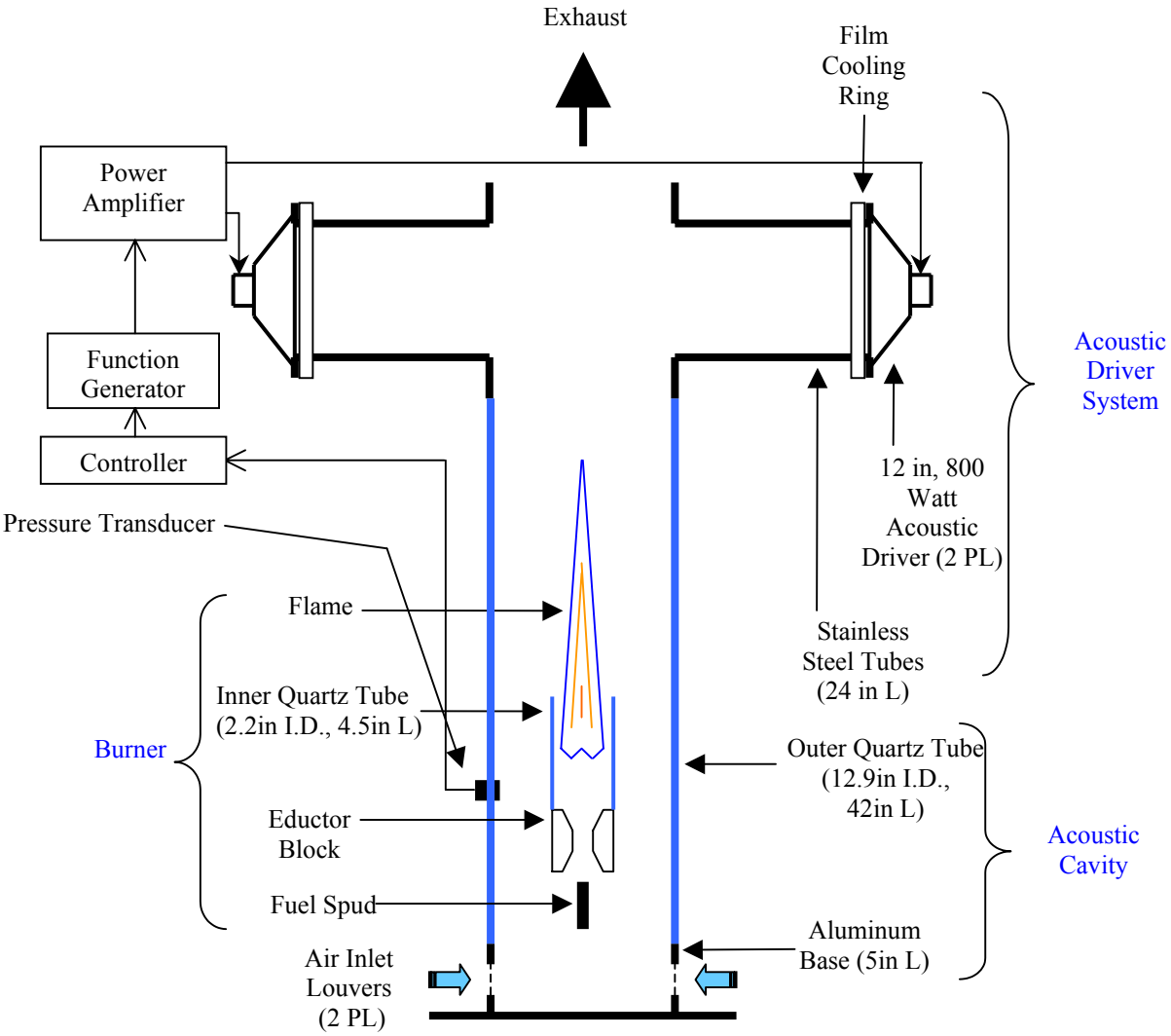

Figure 4-1: Schematic of overall test section.

4.1.2 Acoustic Cavity

The acoustic cavity consists of an aluminum ring, closed at the bottom end. It has two sets of inlet louvers cut on opposing sides to allow air to flow into the tube, while providing an acoustically closed end condition. A large diameter-matched quartz tube rests in a thin register on the aluminum ring, and extends for an additional 42 inches.

Quartz was used in order to withstand high flame temperatures, as well as to allow transmission of the ultraviolet laser sheet and fluorescence signal. The tube also has several laser-drilled holes at various locations to provide instrumentation entry ports. See Appendix A for more precise details on the dimensions of the acoustic chamber.

4.1.3 Test Burners

The burner sections are shown in Figure 4-3, in the aerodynamically stabilized and bluff-body stabilized configurations used. The design allows for a variety of different flameholder configurations to be easily tested. Elements common to both arrangements include a fuel spud that ejects a premixed jet of fuel and an additional gas into the eductor block made of machinable ceramic. The jet entrains air as it enters the eductor, where it is jet-mixed, resulting in a partially premixed flame.

For the aerodynamically stabilized flame, the flame is stabilized above the recirculation zone created as the flow exits the eductor and expands into the 4.5 inch tall burner tube. In the bluff-body stabilized burner, two additional tabs (constructed of machinable ceramic) are provided in the stabilization zone, which can provide a stronger recirculation zone for the flame to attach itself. In this case, the burner tube is 3.75 inches tall, with the remaining height taken up by a small quartz piece and the ceramic flameholder to bring the total height to 4.5 inches. The tabs are approximately 0.5 x 0.5 x 0.5 inches in size yielding a blockage of approximately 7.4%, and are tapered on the upstream side. More details of the bluff-body tabs can be seen in Figure 4-2. Each burner has two sets of burner tubes in which the flame is stabilized, one made of pyrex (I.D. 2.17 inches, O.D. 2.35 inches) and the other one of quartz (I.D. 2.17 inches, O.D. 2.33 inches). The

pyrex burner tubes are used for the shadowgraph and chemiluminescence measurements. Quartz tubes are required for the PLIF experiments, since they need to be able to transmit UV light. They also have two 1/8-inch slits cut on opposite sides in order to allow the laser sheet to pass through and illuminate the flame. The slits eliminate luminescence of the quartz tube caused by the laser sheet, which interferes with the fluorescence signal.

Figure 4-4 provides details of the gas feed system. Fuel for the burner is 50% methane premixed with 50% CO_2 gas to increase the mass flow. The premixer inlets for each gas are choked in order to prevent disturbances from propagating upstream and affecting flow rates. The mixture is subsequently passed through a laminar flow element (Meriam Model 50MJ10 Type 9). The temperature of the mixture is measured by a type-K thermocouple and a digital thermometer (Analog Devices, Model AD2050-K), while the pressure drop is measured by a barocel pressure sensor (Datametrics model 590D-10W-3P1-H5X-4D, 1400 electronic manometer). From these measurements, the flow rate is determined. The flow then exits the fuel spud and entrains atmospheric air. The volumetric flow rate through the spud is 2.14 SCFM, yielding a jet velocity of 30 m/s (*Re* = 20,000).

Figure 4-2: Bluff-body stabilized burner flameholder detail, viewed from the upstream side.

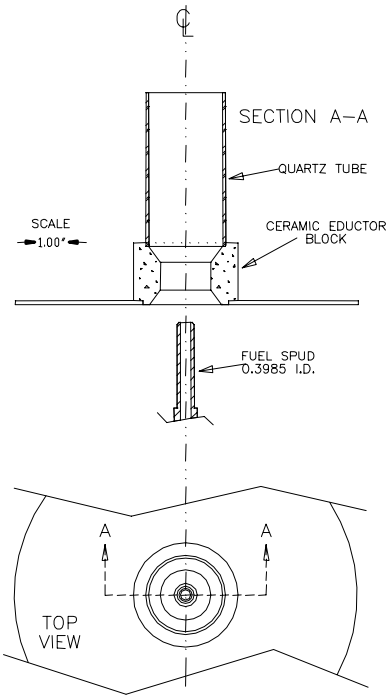

(a)

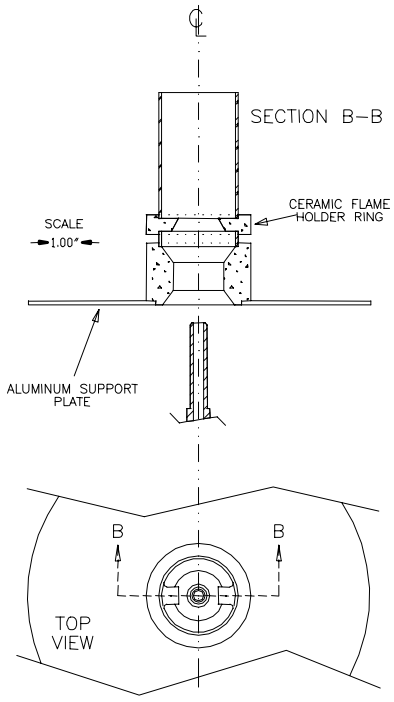

(b)

Figure 4-3: (a) Aerodynamically stabilized burner (b) bluff-body stabilized burner.

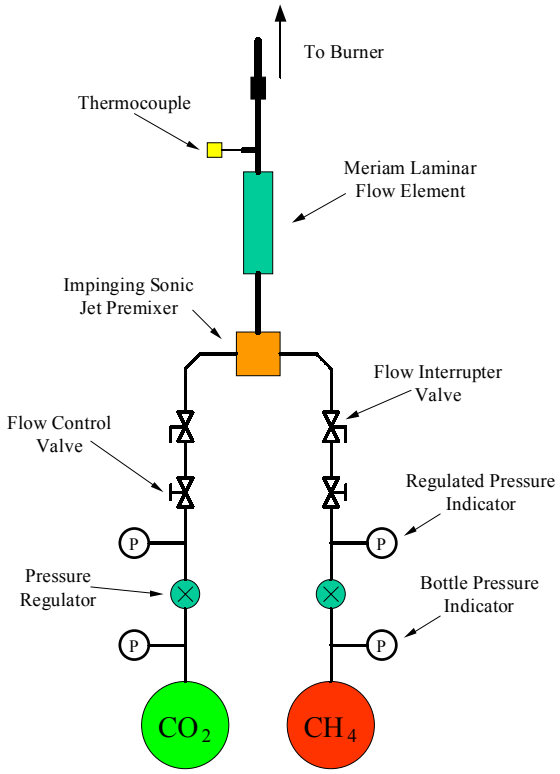

Figure 4-4: Gas feed system.

4.2 Acoustic Properties

In order to determine the acoustic properties of the chamber, a second pressure transducer was used to traverse the height of the chamber, while using the acoustic drivers to excite the system during a cold test.

Figure 4-5 shows the peak-to-peak pressure amplitudes under identical power conditions to those in the hot flame conditions. The driving frequencies used in this section were 22,

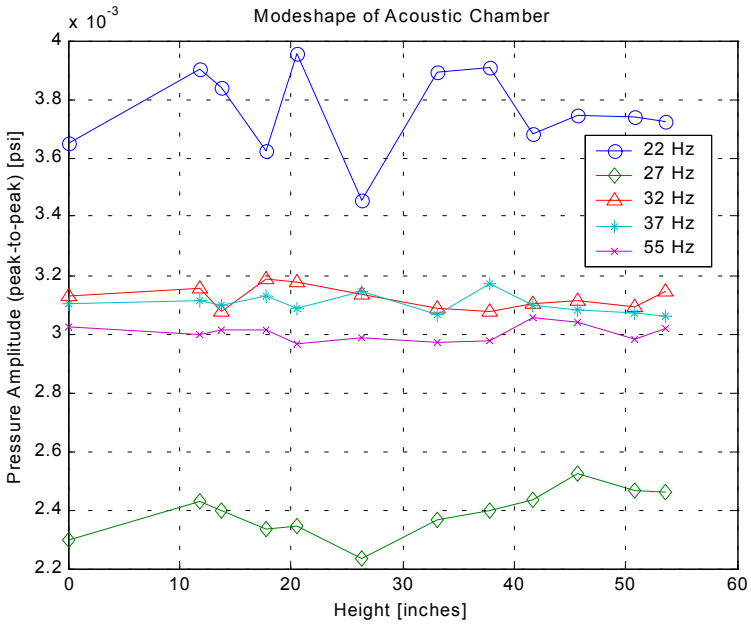

Figure 4-5: Peak-to-peak pressure amplitudes in the chamber, driven at various frequencies (no flame).

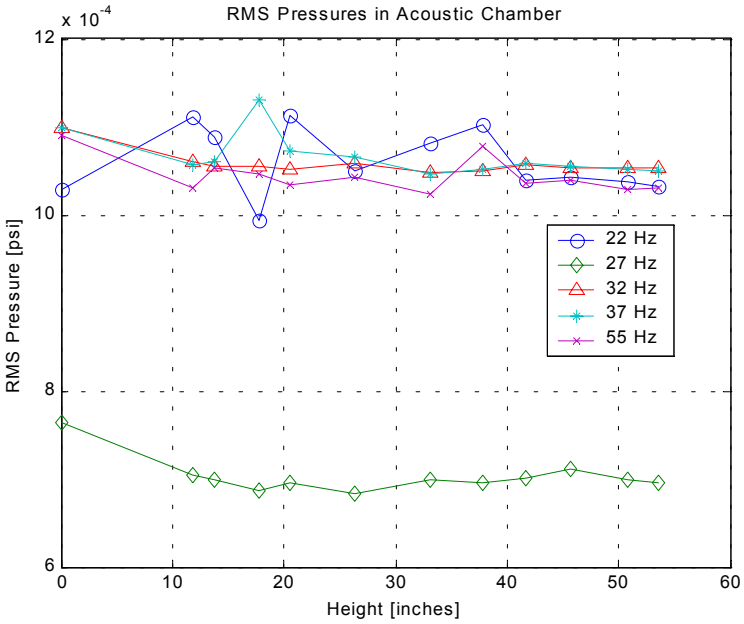

Figure 4-6: RMS pressure in the chamber, when driven at various frequencies (no flame).

27, 32, 37, and 55 Hz[2]. Due to difficulties inherent in producing low frequencies by the acoustic drivers (a very large excursion range is required), less power is given to the system at 22 Hz and 27 Hz to avoid driver failure. This is evident in the lower peak amplitudes at 27 Hz, however it is not as evident at 22 Hz. In the 22 Hz case, non-linearities in the drivers cause additional modes to be excited and cause the increased peak amplitudes. Figure 4-6 displays the rms pressures for the same test. Due to the driver nonlinearity, the rms pressure for 22 Hz matches those for the higher three frequencies, which are driven at the same (higher) power level. The drivers have a smoother response at 27 Hz that results in lower rms pressures at this frequency, since it is driven at a lower power level.

An important result from this test is the modeshape of the acoustic wave that the driving system establishes in the chamber. In Figure 4-5, the variations in peak amplitude at different heights and frequencies are shown. The maximum variation in peak amplitude is less than 3% from the mean amplitude for 32-55 Hz, increases to 6.4% at 27 Hz, and increases further to 8.1% at 22 Hz. If any of the driving frequencies excited a natural mode of the system, a distinct modeshape would be apparent from the amplitudes of the pressure traces at different heights (i.e., nodes and antinodes would be identifiable). Since the variation in amplitude is relatively low and the curve is flat, it can be reasonably concluded that the acoustic drivers produce a bulk mode in the system and not a standing wave.

[2] Actual frequencies were 22.02, 27.02, 32.02, 37.02, and 55.02 Hz, to prevent the system from "mode-locking" with the 10 Hz laser repetition rate.

4.3 Diagnostics

This section describes the diagnostics used in the flow visualization and combustion dynamics experiments, excluding equipment specific to PLIF, which is found in the next section.

4.3.1 Pressure Transducers

A piezoelectric pressure transducer (PCB Piezotronics, model 106B50) is located at a height of 3 inches above the fuel spud, where the flame is stabilized in the burner. This transducer was selected for its high sensitivity (493.3 mV/psi) and thermal characteristics. An additional piezoelectric transducer (PCB, 112A04) with a sensitivity of 2258 mV/psi was used to traverse the length of the test section when determining the modeshape of the system under various forcing frequencies. A PCB model 482A16 power supply and amplifier, using a gain stage setting of 100, powered both transducers.

4.3.2 Data Acquisition System

The computer used in the data acquisition system consisted of an AMD Athlon 650 MHz processor with 512 MB of RAM and approximately 100 GB of total hard drive space (image files are large). The system contains a CD-RW drive used to archive the data. Installed in the computer are two DAS1602/16 (Computer Boards) 16-bit data acquisition boards. One operates in differential mode measuring quantities including the oscillator frequency, pressure, laser shot energy, camera triggers, and control effort, while the other board operates in single-ended mode and measures three type-K thermocouple temperatures in the acoustic chamber (at heights of 18, 25, and 37 inches). Also in the same computer is the PCI controller card for the Princeton Instruments ICCD camera and

the IEEE 1394 FireWire card used to interface with the Vision Research Phantom V4.0 camera. The software package used to acquire data is National Instruments LabView 5.1.

4.3.3 High-Speed Video Camera

A Vision Research Phantom V4.0 high-speed video camera is used to capture images for the shadowgraph and chemiluminescence experiments. It is based on a proprietary 512 x 512 pixel monochrome SR-CMOS (Synchronous Recording, Complementary Oxide Metal Semiconductor) sensor, capable of exposure times as low as 10 μs. The camera contains 256 MB of memory on board, which allow it to acquire data at 1000 frames per second, for just over 1 second. Higher frame rates are possible by lowering the pixel resolution. The camera is equipped with a C-mount, and a Nikon 50 mm F/1.4 lens is used with a C-mount-to-F-mount adapter. Use of a lens with a low f-stop number increases the light gathering capacity of the lens and decreases it's depth of view. A decreased depth of view is advantageous, since it minimizes line-of-sight integration, though small contributions out of the focal plane that smear the image will be inevitable.

4.3.4 Additional Electronics

Two custom electronics units used in the experiments were designed and built by co-experimenter Steven L. Palm. The first is an active control unit that regulates the power amplifier output to the acoustic drivers. Output from the pressure transducer (PCB 106B50) is notch filtered by the controller to determine the amplitude of the fundamental frequency the acoustic drivers are producing in the chamber. This is compared with an adjustable preset value in the controller, which uses PI control to regulate the system to ensure a constant pressure amplitude at the transducer location (a height of 12 inches,

approximately level with the flame stabilization zone). The second unit is a peak capture/amplifier box, which reads the output from the pyroelectric joulemeter (Molectron J9LP) measuring laser shot energy and amplifies the signal so it can be read by the data acquisition system. More details on this equipment can be found in the work of Palm (*in progress*).

4.3.5 Shadowgraph Setup

The reacting flowfield was visualized using the high-speed Phantom V4.0 video camera described above, in a standard Z-configuration shadowgraph arrangement. Two 30 cm diameter spherical mirrors collimate the continuous light generated by an Ealing 250W universal arc-lamp supply driving a Mercury arc-lamp (Ealing, Model 27-1031). More details on the shadowgraph imaging arrangement are shown in Figure 4-7. Due to the curved surfaces of the burner and acoustic chamber, imaging was performed on an unforced flame above the burner tube.

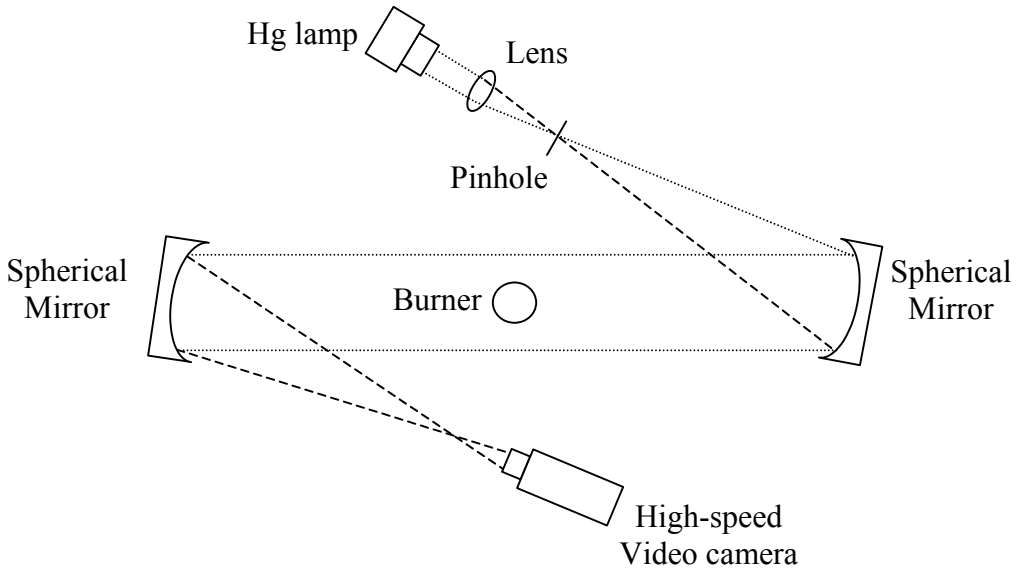

Figure 4-7: Shadowgraph imaging setup.

4.3.6 Chemiluminescence Measurements

In combustion experiments, a now common method of determining the reaction zone is to image the light emitted in the combustion zone (McManus et al. 1995). Of particular importance are C_2, CH, and OH radicals, since they are produced as intermediaries of the combustion process. Hurle et al. (1968) established the linearity between the radiation emitted and the volumetric heat release. Numerous studies involving combustion instabilities have taken place using this relationship (Samiengo et al. 1993; Shih et al. 1996; Broda et al. 1998). The major limitations with this technique are the integration of the intensities along the line of sight, and relatively long integration times O(~100 μs) due to low signal strength.

Consistent with previous JPC researchers, no filters are used, and the total radiation emitted from the combustion process is taken to be proportional to the heat release rate. The measurements taken by Sterling (1987) used a masked photomultiplier to achieve spatial resolution, and were subsequently improved upon by Zsak (1993) and Kendrick (1995), with the introduction of the Hycam (high-speed film camera) providing two-dimensional spatial resolution. In this work, advances in imaging technology further simplify measurements by use of the Phantom digital high-speed video camera described earlier. This provides temporally and spatially resolved measurements of the heat release subjected to a forced acoustic field, without the jitter introduced by a high-speed mechanical film camera.

4.4 Shadowgraph Results

In this particular configuration, the shadowgraph imaging technique provided limited results. Results could not be obtained under forced conditions and in the interior of the burner tube. While the flow fields are similar, there exist some differences between the aerodynamically and bluff-body stabilized cases, as shown in Figure 4-8. The bluff-body burner shows wider spreading of the flame outside of the burner and also displays finer structures in the downstream section. These can be attributed to the stronger recirculation zones and vorticity generated by the bluff-bodies.

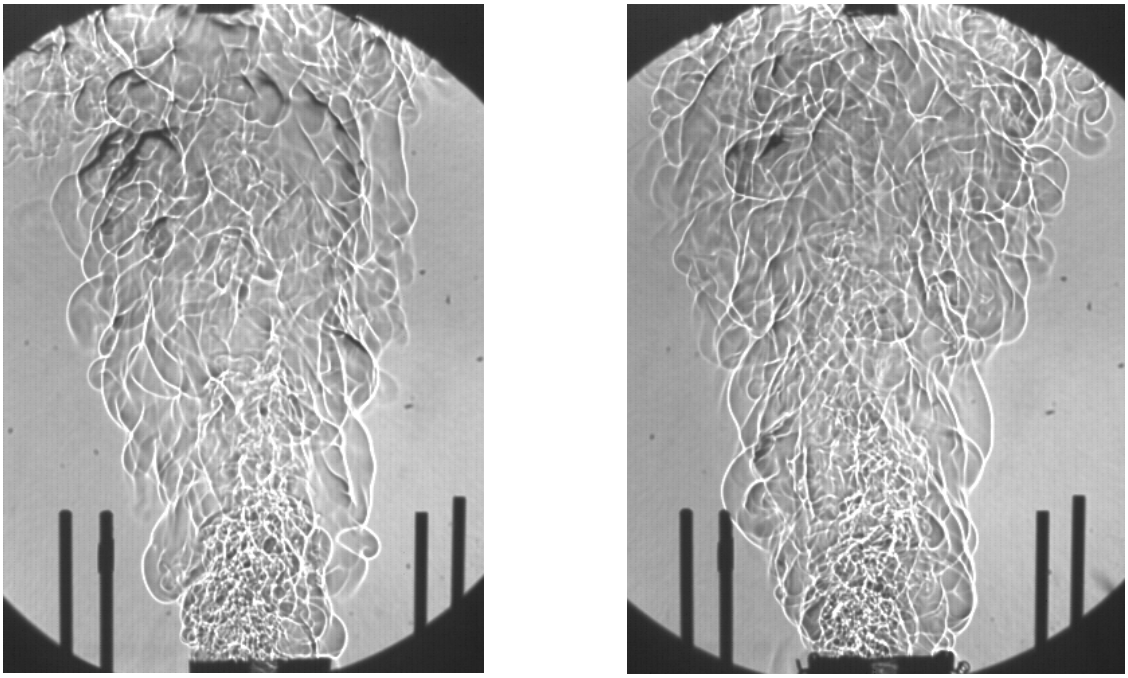

(a) (b)

Figure 4-8: Shadowgraph results above the burner tube for (a) aerodynamically and (b) bluff-body stabilized cases.

4.5 Chemiluminescence Results

4.5.1 Two-Dimensional Flame Structure

Single shot chemiluminescence images from the Phantom V4.0 camera were smoothed using a 3 x 3 median filter in Matlab. Images were then averaged by phase-locking to the pressure signal. Images were selected by locating their temporal locations, and selecting the images to be averaged based on their proximity to the sixteen phase divisions used. Approximately 15 images were used in the average at each phase position. The maximum phase resolution jitter was found to be less than 2 degrees in all cases. Contours were computed and plotted for each case (five forcing frequencies x two burners) showing eight phases in a cycle, and are displayed in Figure 4-9 through Figure 4-13. Contour levels are plotted at 5, 20, 40, 60, 80, and 95 percent levels of the maximum intensity of the 0 degree phase contour plot for each case. In all cases, the phases are taken as a sine wave, with 0 degrees corresponding to a zero crossing with a rising edge.

For forcing at 22 Hz (Figure 4-9), the bluff-body burner shows a larger stabilization zone than the aerodynamic burner (40% contour), centered at approximately a height of 5 cm. Note that the center "hole" at 8 cm at a phase of 0 degrees is actually at a contour of 5%, and not 40%. Characteristics to note in both cases are the traveling of a wave in the upstream direction on the outer edge of the flame, from 0 to 180 degrees. At 180 degrees, the wave reverses itself, and travels back downstream. There is also a distinct change in intensity as the flame oscillates. The intensity contour at 40% can be seen to grow into the burner tube as the flame evolves from 0 to 180 degrees, and in the bluff-body case even connects with the 40% contour levels in the stabilization zone. Again, as the pressure changes from 180 to 360

degrees, this intensity zone separates from each other and travels back downstream. These two oscillating characteristics are generally observed for each forcing frequency, except for the 55 Hz case.

At a frequency of 27 Hz (Figure 4-10), much the same phenomenon is observed, with a decrease in the amplitude of the outer propagating wave. In addition, there appears to be a superimposed higher frequency, lower amplitude outer wave, continuously traveling downstream. As the forcing frequency is increased to 32 Hz (Figure 4-11), the intensity of the flame in the burner tube has diminished – note the decrease in size of the 40% contour in the flame stabilization zone inside the tube. Once the acoustic oscillations reach 37 Hz (Figure 4-12), an interesting reversal occurs. The contours in the stabilization zone show a significantly larger 40% contour for the aerodynamically stabilized burner, than the bluff-body stabilized case. Recall in all previous cases, the bluff-body stabilized burner yielded stronger stabilization zones or at least zones comparable to that of the aerodynamically stabilized burner. Finally, for the 55 Hz case (Figure 4-13) there is essentially no change between contours at different phases. The low amplitude traveling waves on the outer rim of the flame are present, but none of the bulk oscillations of intensity or flame shape that occurred in previous situations.

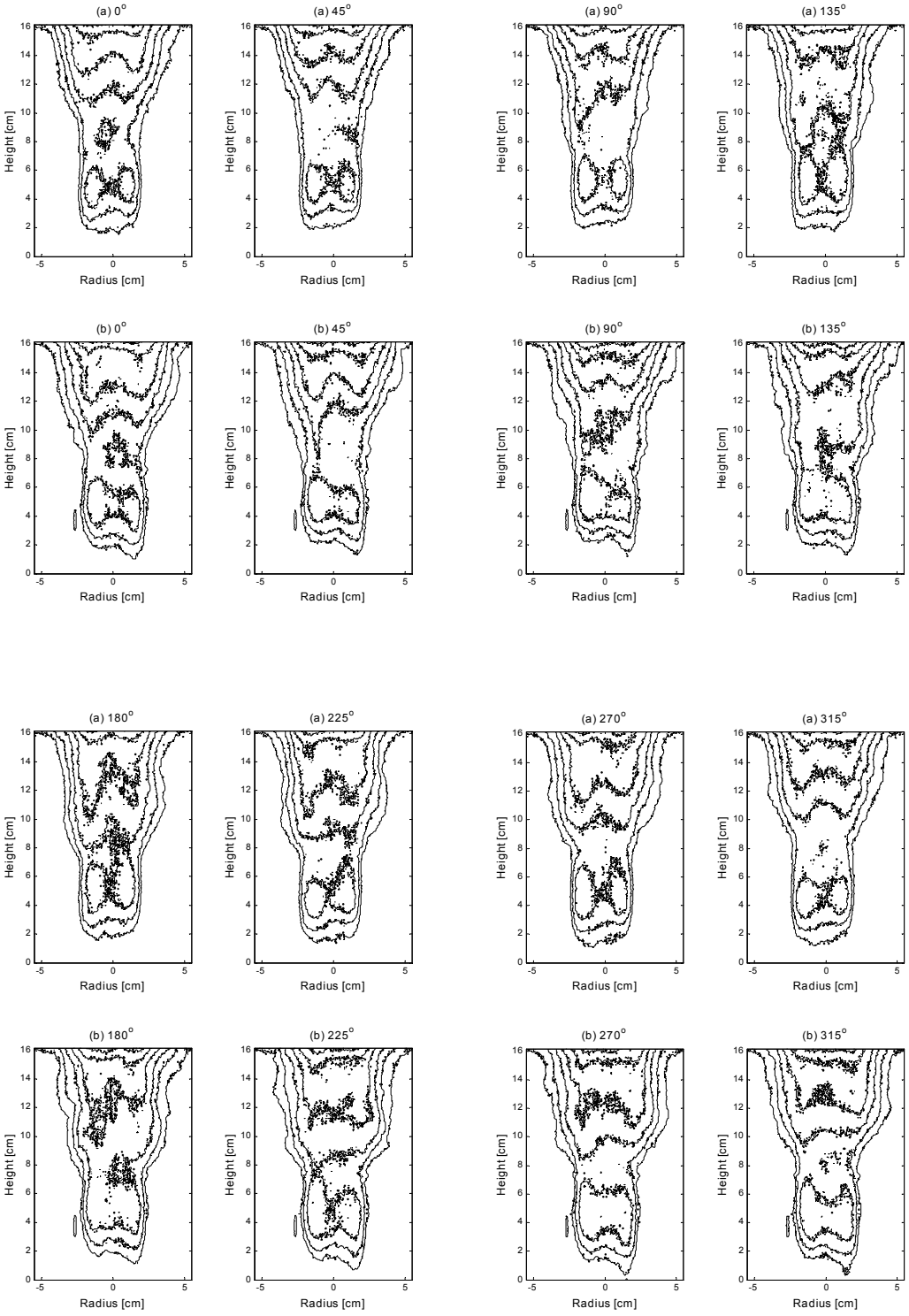

Figure 4-9: Chemiluminescence contour plots at 22 Hz for (a) aerodynamically stabilized and (b) bluff-body stabilized cases.

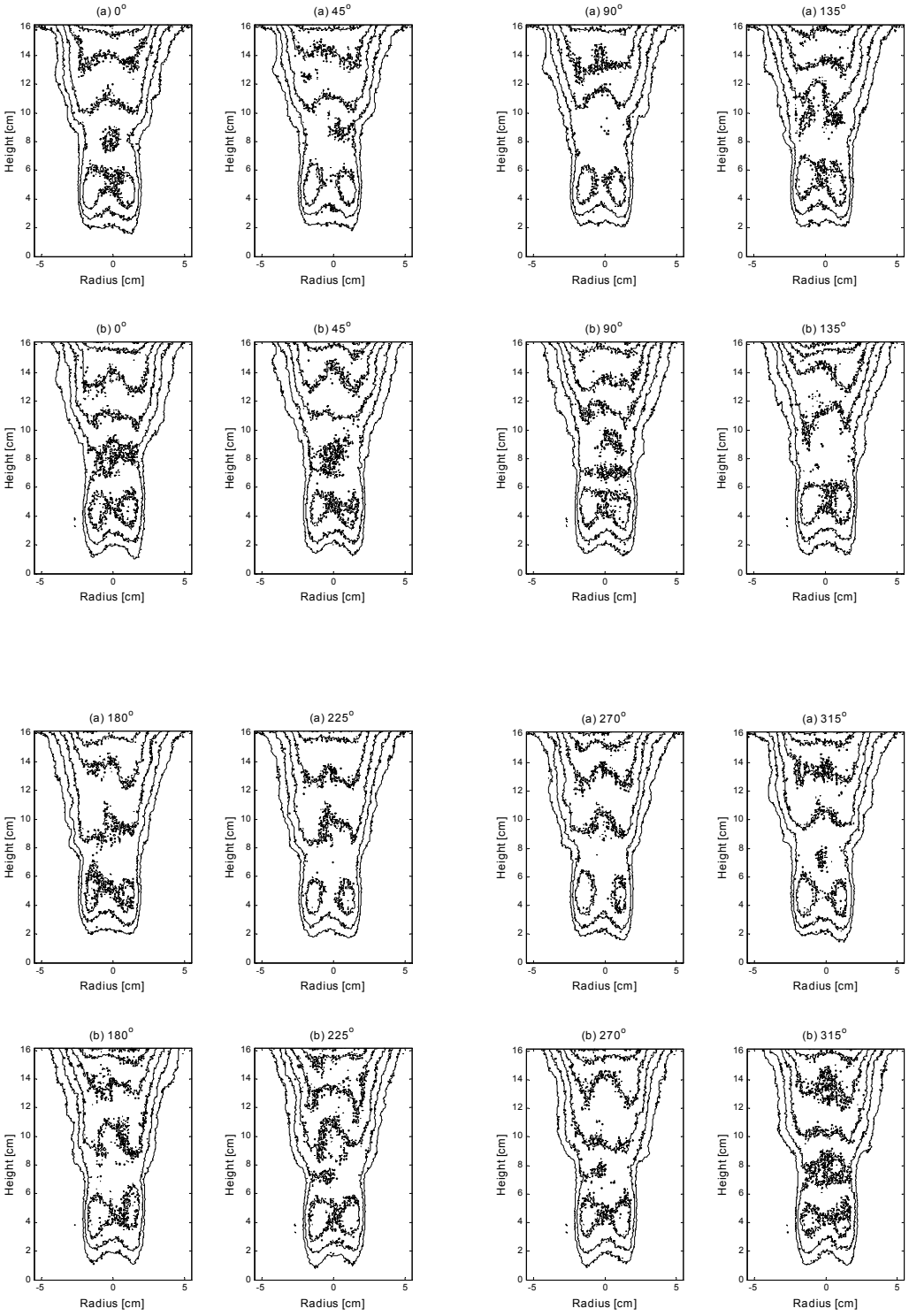

Figure 4-10: Chemiluminescence contour plots at 27 Hz for (a) aerodynamically stabilized and (b) bluff-body stabilized cases.

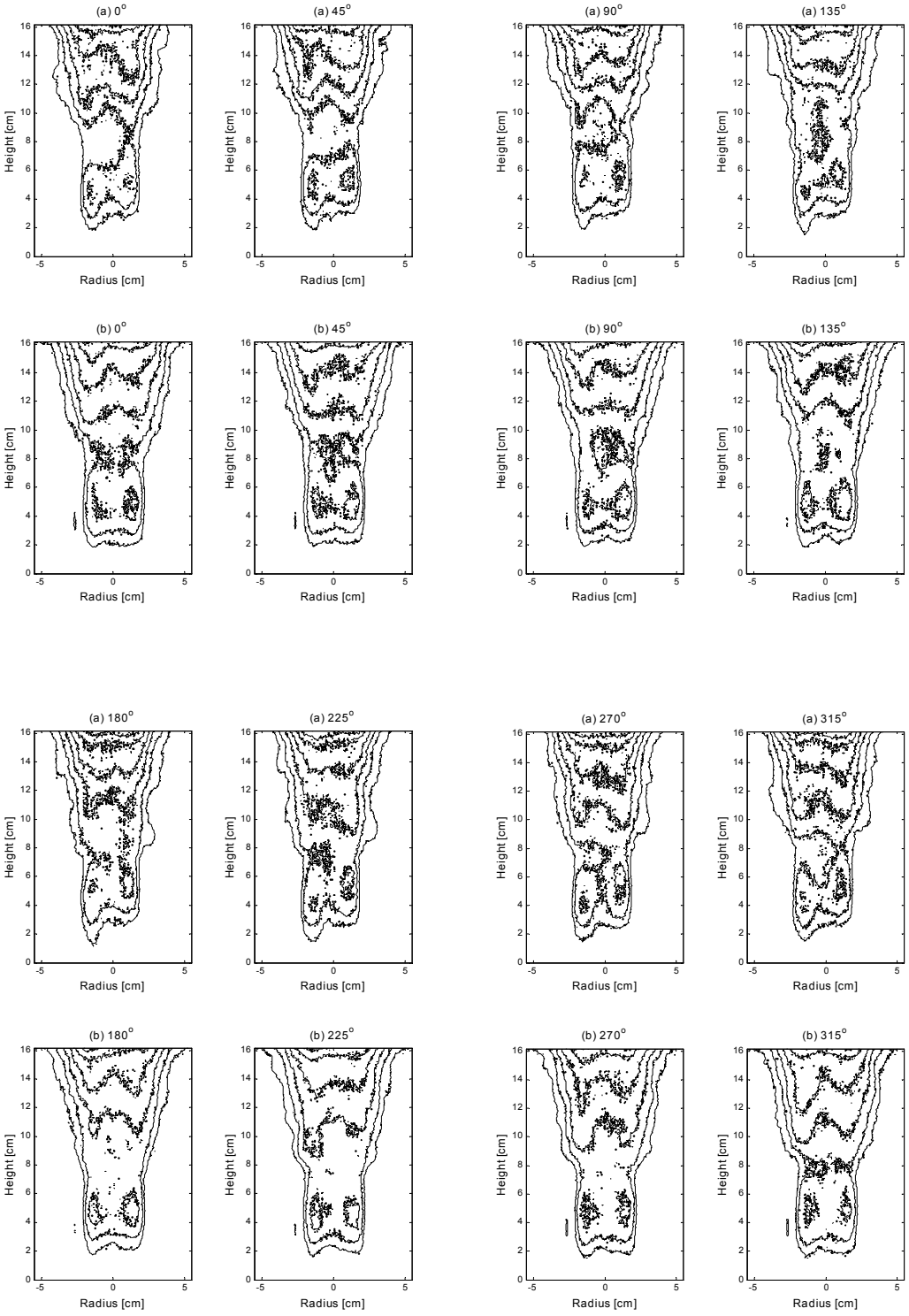

Figure 4-11: Chemiluminescence contour plots at 32 Hz for (a) aerodynamically stabilized and (b) bluff-body stabilized cases.

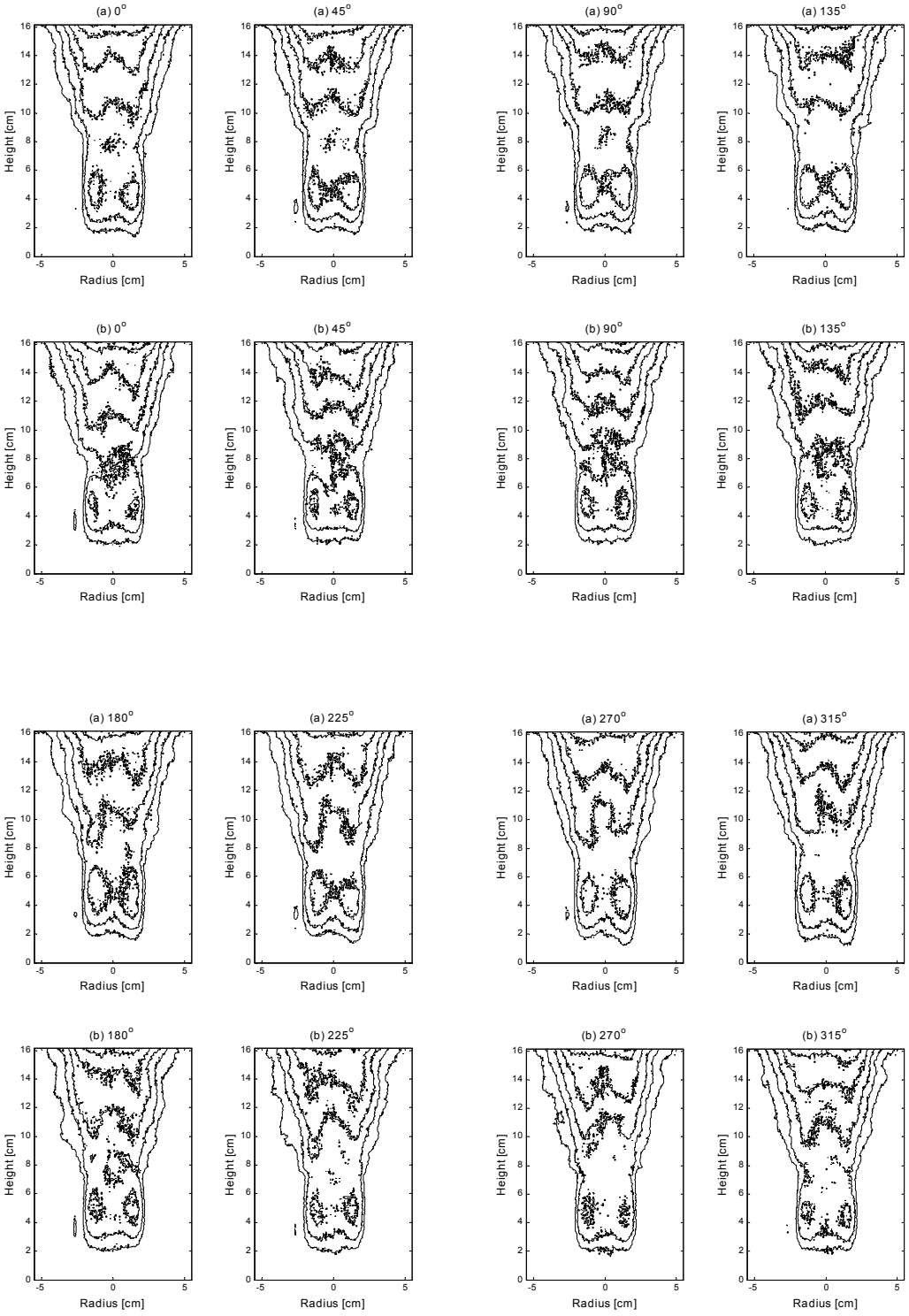

Figure 4-12: Chemiluminescence contour plots at 37 Hz for (a) aerodynamically stabilized and (b) bluff-body stabilized cases.

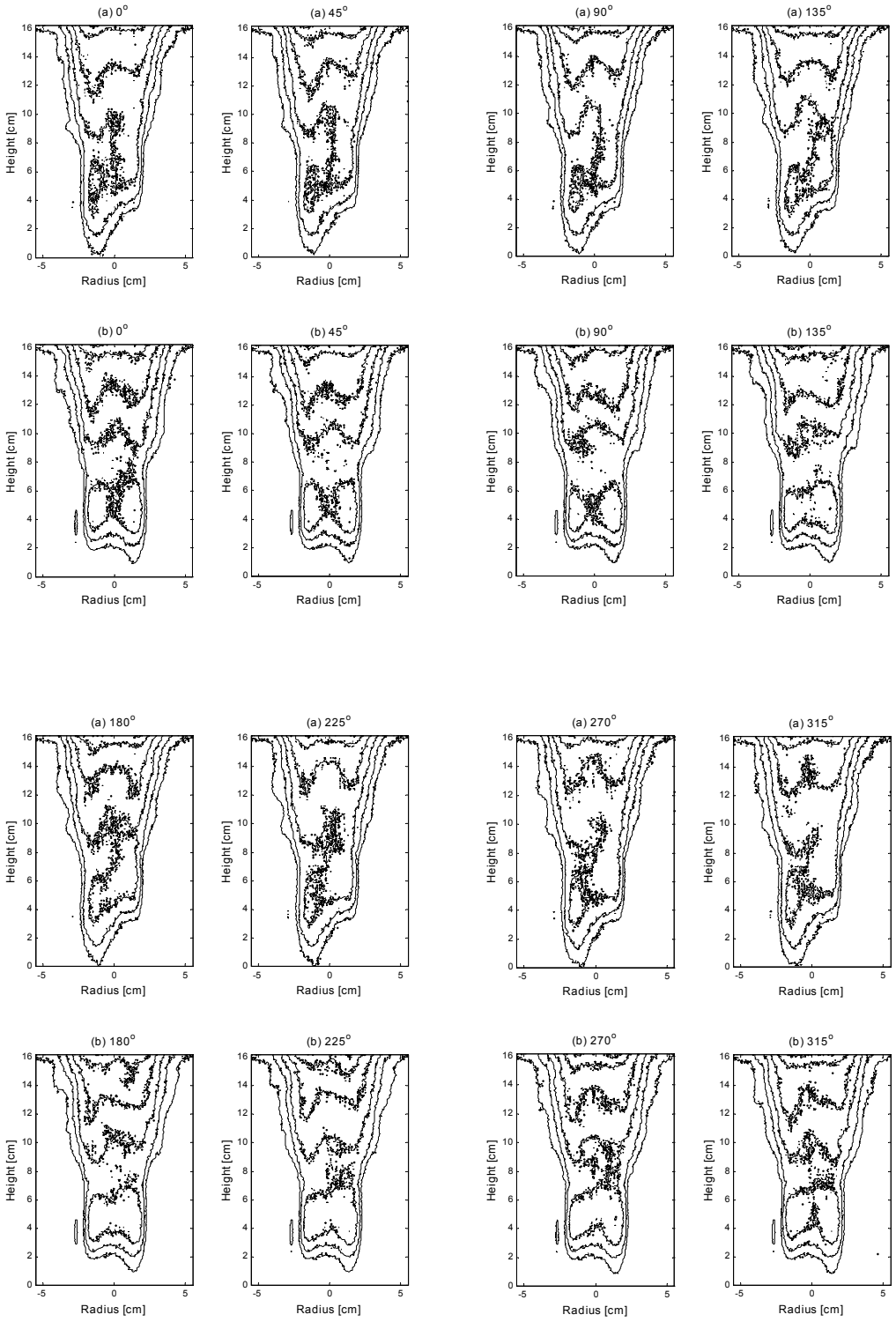

Figure 4-13: Chemiluminescence contour plots at 55 Hz for (a) aerodynamically stabilized and (b) bluff-body stabilized cases.

4.5.2 Axial Flame Structure

In order to emphasize the periodic motion contained in the flames, axial plots showing the mean intensity as a function of height and phase were constructed and plotted on a 2D contour plot. Mean intensities were calculated using a threshold intensity of 15, corresponding to approximately 5% of the maximum intensity level in the flame. Values below the threshold were considered to be outside the flame zone and not incorporated into the mean. In addition, the axial contours were averaged over a period, and the averages used to normalize the plots, which further enhances the periodic motion of the flame (Figure 4-14 through Figure 4-23). The mean plots of flame intensity are absolute – they are not normalized in any way to enable comparison between different forcing conditions. The flame base is defined at an intensity level of 15, and can be easily seen on the mean axial intensity plots. Data at conditions below approximately 2 cm (below the flame base) on the normalized intensity plots should be disregarded, since they are outside the flame zone (denoted by dark blue structures). Both sets of plots are repeated over an additional period for illustrative purposes.

Immediately observed is the fluctuation of the flame base (note: the lowest intensity plotted is at 15, i.e., the flame base). In each case, the flame base oscillates in a sinusoidal manner, corresponding to the driving frequency imposed by the acoustic drivers. Table 4-1 compiles the mean flame height, the amplitude of the oscillation, and the percent changes of these parameters when transitioning from the aerodynamically stabilized burner to the bluff-body burner.

	Mean Height (cm)			Amplitude of Oscillation (peak-to-peak) (cm)		
Frequency (Hz)	Aero	BB	Relative Change	Aero	BB	Relative Change
22	1.65	1.17	-29%	0.89	1.02	+15%
27	1.88	1.25	-33%	0.56	0.40	-28%
32	2.07	1.90	-8%	0.55	0.24	-56%
37	1.53	2.14	+40%	0.50	0.28	-44%
55	0.37	1.06	+186%	0.14	0.16	+14%

Table 4-1: Flame base position and oscillation.

At low frequencies, the bluff-body stabilizer has the effect of lowering the mean flame base position. At approximately 32 Hz, a change in the characteristics of the bluff-body flame seems to occur. At frequencies greater than 32 Hz, the bluff-body case shows increased flame base positions relative to the aerodynamic case. For frequencies between 22 and 37 Hz, the flame base increases continuously, except for the aerodynamically stabilized burner, which shows a sharp lowering of the mean flame base at 37 Hz. At 55 Hz, both burners appear to enter into a different regime from the lower frequencies. In addition, the bluff-body burner generally has a lower amplitude of oscillation than the aerodynamically stabilized burner.

Figure 4-14 and Figure 4-15 show the mean and normalized axial intensities at 22 Hz. It is evident from the flame structure that both burners are responding strongly to the acoustic forcing. The ranges of motion taken from the normalized axial intensity are comparable in

size, with the aerodynamic burner tending to oscillate at a higher overall position. Note the higher angle of oscillation for the aerodynamic case in Figure 4-15. This implied a larger velocity of the flame, possibly due to flow retardation caused by the enhanced recirculation off the bluff-body burner.

At 27 Hz, the mean axial intensities (Figure 4-16) show a stronger coupling in the aerodynamic case. The normalized intensities (Figure 4-17) show comparable angles (i.e., velocities) and a similar range of motion. As the driving frequency is increased to 32 Hz, there is a much stronger motion observed in the aerodynamic case (Figure 4-19). Again, the velocities of the motion are comparable between the two cases. At 37 Hz, there is much stronger anchoring of the flame in the aerodynamic case at the flame base, as shown in Figure 4-20. Figure 4-21 shows significantly more motion in the bluff-body case, which is observed for the first time. At the highest frequency tested of 55 Hz, Figure 4-22 and Figure 4-23 show very little motion in both cases.

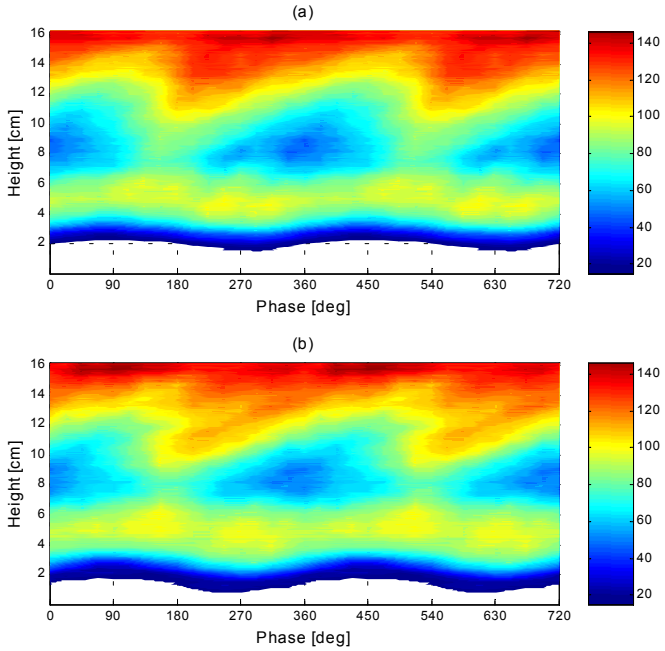

Figure 4-14: Mean axial intensities at 22 Hz (a) aerodynamic (b) bluff-body.

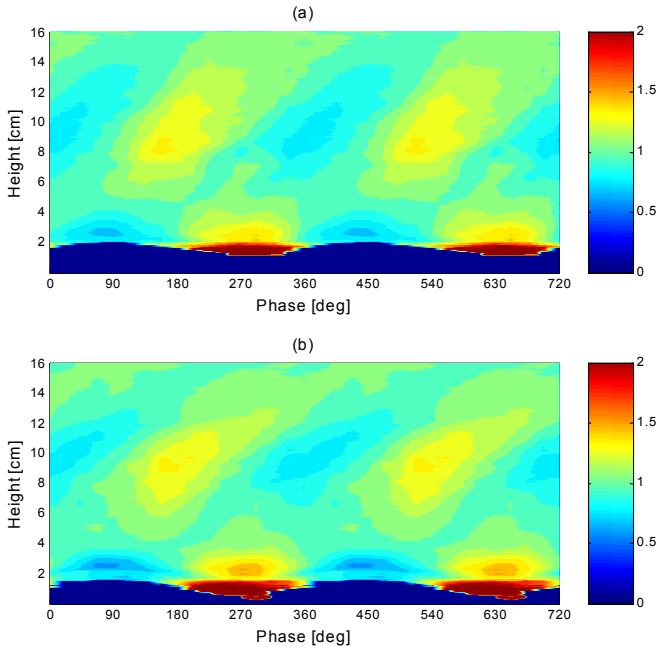

Figure 4-15: Normalized axial intensities at 22 Hz (a) aerodynamic (b) bluff-body.

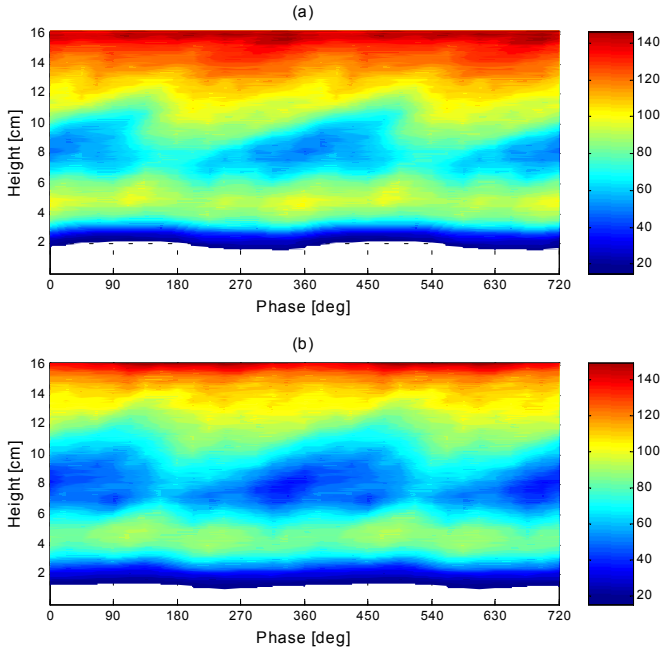

Figure 4-16: Mean axial intensities at 27 Hz (a) aerodynamic (b) bluff-body.

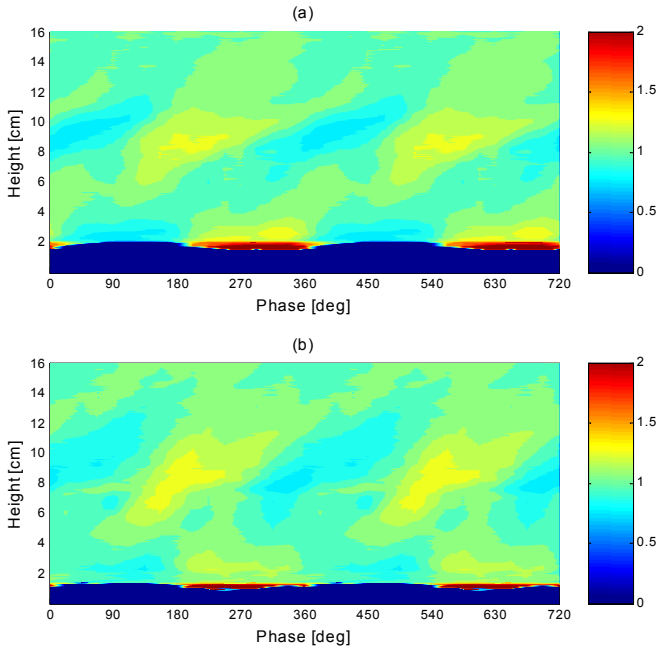

Figure 4-17: Normalized axial intensities at 27 Hz (a) aerodynamic (b) bluff-body.

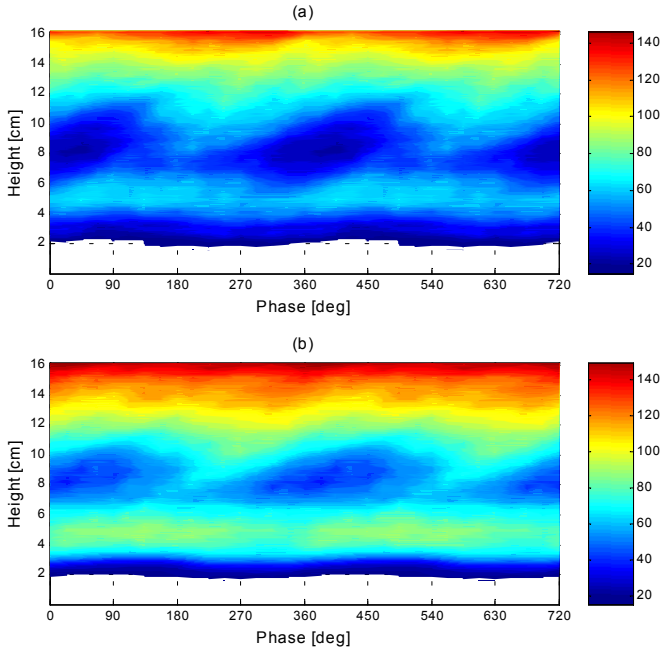

Figure 4-18: Mean axial intensities at 32 Hz (a) aerodynamic (b) bluff-body.

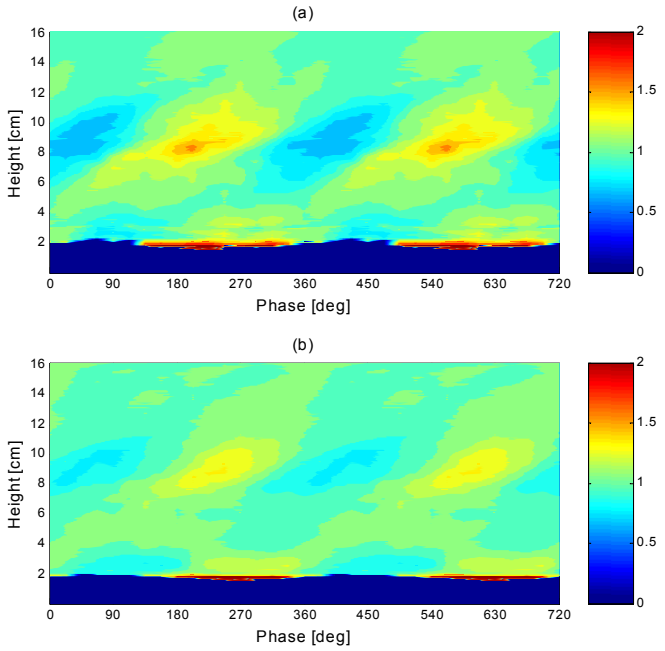

Figure 4-19: Normalized axial intensities at 32 Hz (a) aerodynamic (b) bluff-body.

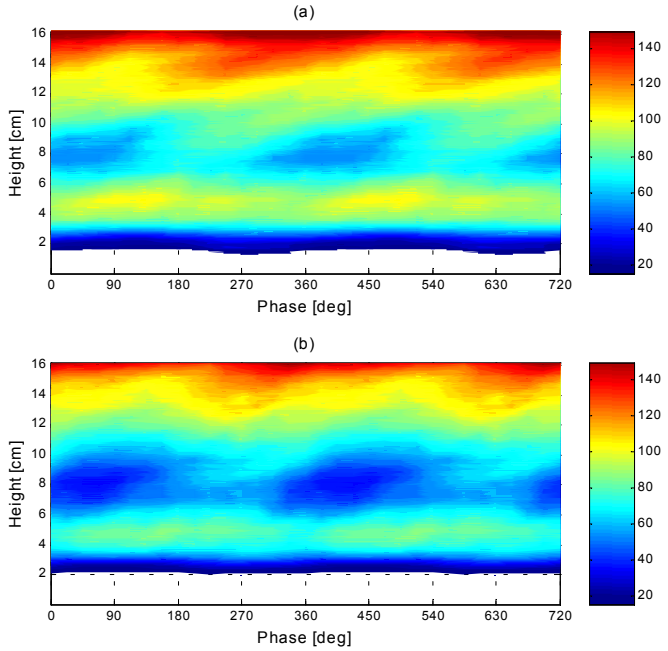

Figure 4-20: Mean axial intensities at 37 Hz (a) aerodynamic (b) bluff-body.

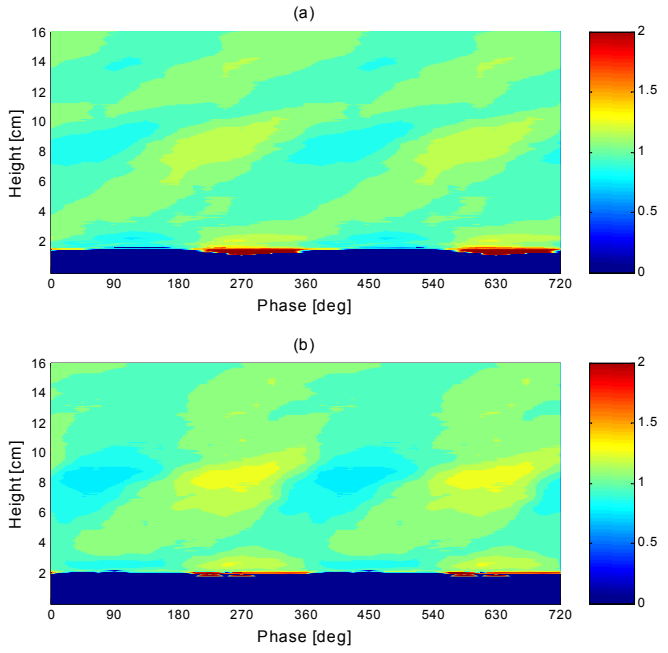

Figure 4-21: Normalized axial intensities at 37 Hz (a) aerodynamic (b) bluff-body.

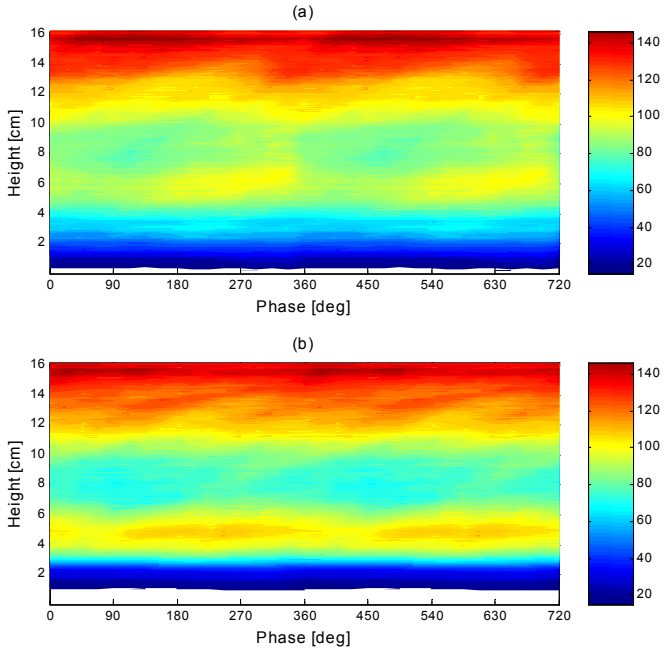

Figure 4-22: Mean axial intensities at 55 Hz (a) aerodynamic (b) bluff-body.

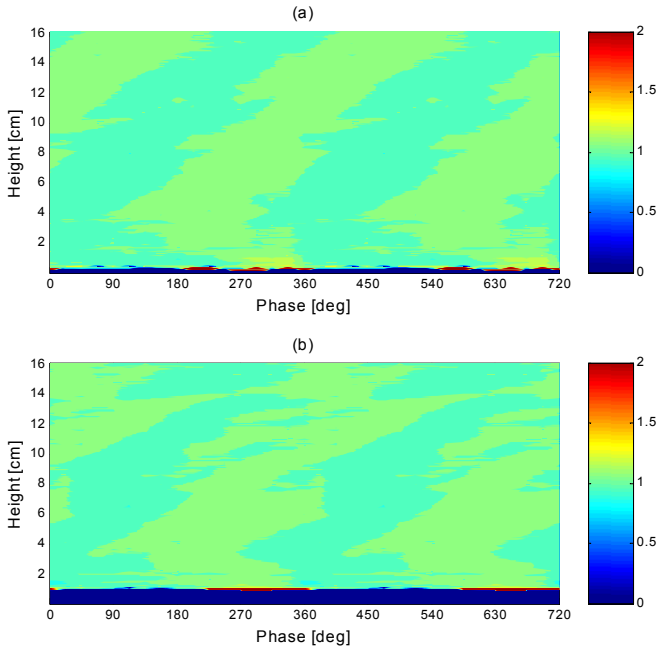

Figure 4-23: Normalized axial intensities at 55 Hz (a) aerodynamic (b) bluff-body.

4.5.3 Modified Rayleigh Index

Since the chemiluminescence measurements can be used as a measure of the heat release, it is possible to use the measurements in order to calculate Rayleigh indices. As mentioned previously, following the development by Culick (1987), Rayleigh's criterion can be stated mathematically as

(4-1) $$\Delta E = \frac{\gamma - 1}{\gamma \bar{p}} \int dV \int_{t}^{t+\tau} p'q' dt ,$$

where ΔE is the incremental energy added to the acoustic field over a period τ due to the coupling between the fluctuating pressure, p', and the fluctuating heat release, q'. For the purposes of this work, equation (4-1) can be modified to yield a frequency-driven or forced Rayleigh index that has been nondimensionalized and normalized to account for the driving pressure amplitude and period. The dependence on gas composition is also removed to give

(4-2) $$R_f = \int_0^1 \frac{p'q'}{p_{rms}\bar{q}} d\xi ,$$

where p_{rms} is the root-mean-square of the amplitude of the driving pressure wave, and $\bar{q}$ is the mean intensity of the heat release. p' is redefined as the driving pressure amplitude, and q' becomes the fluctuation in heat release. The time dependence has been normalized by the period of the driving acoustic wave, T, to give a nondimensional time ξ. R_f can be applied globally to a system to yield a global frequency Rayleigh index, or over a series of small control volumes to produce a 2D map of the frequency Rayleigh index. This will affect the definition of q in equation (4-2), but will be valid provided it is defined in a consistent manner.

4.5.4 Global Forced Rayleigh Results

The phase information brings with it the ability to calculate R_f directly for the system. Since the heat release varies both spatially and temporally, it is important to define how the heat release is calculated in the modified Rayleigh index, equation (4-2). For the global results, the heat release is first calculated according to

(4-3) $$q'(\xi) = \int_0^{L_x}\int_0^{L_y} q'_{2D}(\xi, x, y)\, dy\, dx\,,$$

where q' is the spatially integrated heat release of the spatially resolved quantity, q'_{2D}. In order to evaluate contributions only from the driving frequency, R_f is calculated for a pressure signal that has been bandpass filtered about the fundamental driving frequency.

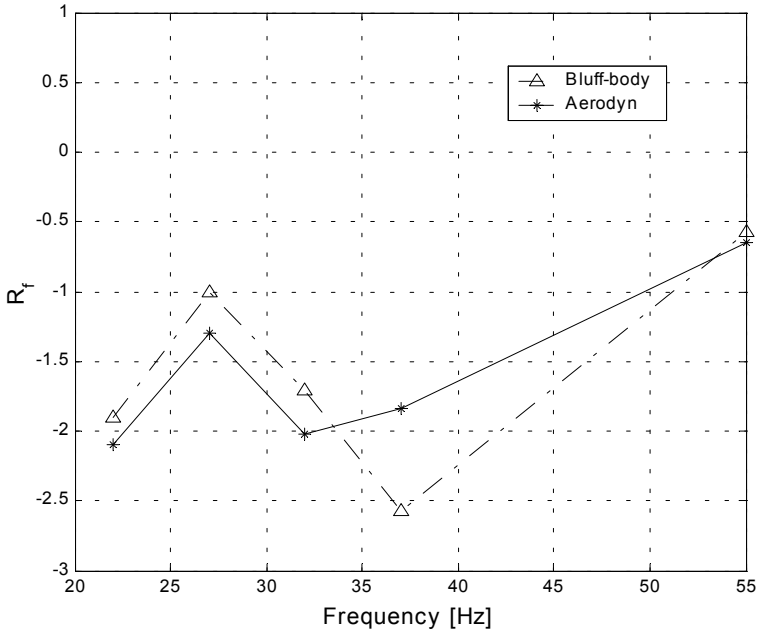

Figure 4-24: Chemiluminescence global forced Rayleigh indices.

The global forced Rayleigh indices are shown in Figure 4-24. They indicate that the aerodynamically stabilized burner in general is more damped than the bluff-body case, except at 37 Hz.

4.5.5 Spatially Resolved Forced Rayleigh Results

A complete set of spatially resolved Rayleigh results can be found in Appendix C. Spatially resolved 2D contour plots and axial forced Rayleigh indices at 32 Hz are shown in Figure 4-25 and Figure 4-26 respectively. The 2D contour plots are shown with contour lines drawn at levels of –20 up to +20, in increments of 2. The positive contours as solid lines, and the negative contours are shown as dashed lines. The 2D indices show a strongly damped anchoring zone at the base of the flame, followed by a driving region in the upper portion of the burner tubes. As the flame exits the burner tube, it is again damped. Some pockets of driving zones also appear, with larger zones appearing in the bluff-body stabilized case.

The axial Rayleigh plots yield similar information, but enable better comparison of the two burner types. The bluff-body axial Rayleigh index peaks approximately 1 cm earlier than the aerodynamic burner, and again shows a stronger driving region at the top end of the flame.

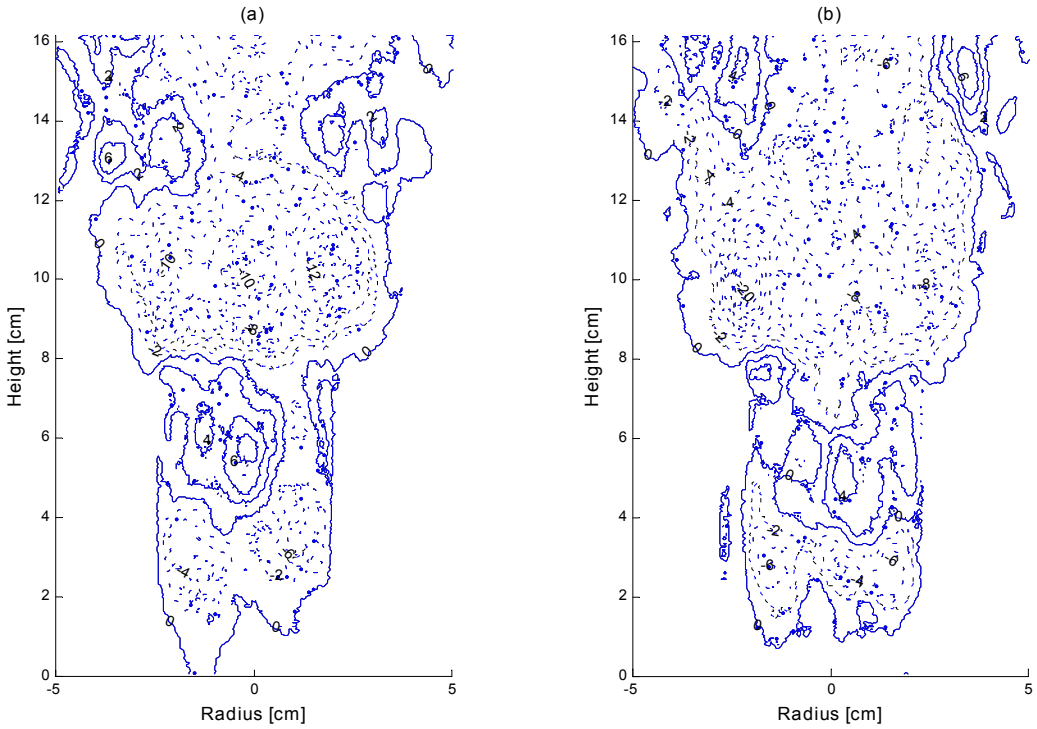

Figure 4-25: Chemiluminescence 2D forced Rayleigh indices at 32 Hz for (a) aerodynamic and (b) bluff-body stabilized burners.

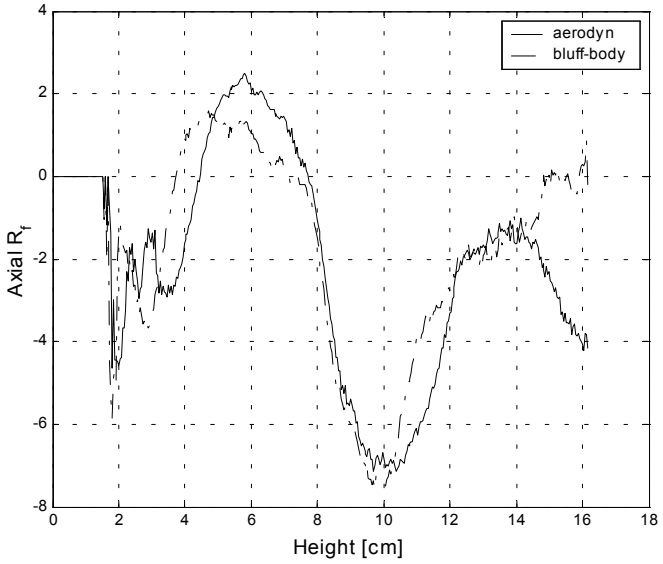

Figure 4-26: Chemiluminescence axial forced Rayleigh indices at 32 Hz.

4.6 Summary

This chapter describes the experimental apparatus and diagnostics used to visualize the two burner types under examination with acoustic excitation. Shadowgraph imagery and chemiluminescence visualization techniques were employed to provide details of the flow field and flame locations. In particular, chemiluminescence provided measures of the flame base location at different forcing frequencies, and the response between the aerodynamically stabilized and bluff-body stabilized burners. In general, the bluff-body burner lowered the position of the flame base, except at 37 Hz, where the opposite effect was observed. Results at 55 Hz showed very little response from the flame to the acoustic excitation. It appears that the burners enter a different regime when they are excited at 55 Hz.

The chemiluminescence measurements also provide relative heat release measurements, which can be used to calculate Rayleigh indices. Global forced Rayleigh indices indicate that the aerodynamically stabilized burner provide more damping at all frequencies, except 37 Hz. Spatially resolved Rayleigh indices were also computed, with examples of 2D contours and axially integrated plots presented.

Chemiluminescence measurements raise questions regarding its validity, particularly in flames that are not two-dimensional in nature, due to the line-of-sight integration that occurs. A possible solution in axisymmetric systems is use of an Abel inversion technique (Smith et al. 2001), which is able to extract planar information from the chemiluminescent signal. However, in highly turbulent environments such as the flames

under study in this work, such a technique is not possible. Adding to this is the complexity that the bluff-body stabilized burner is not axisymmetric. These concerns give rise to more accurate spatially resolved measurements, which are explored in detail in the next chapter.

Chapter 5
OH PLIF Measurements

This chapter describes the experimental results and measurements of combustion dynamics of a flame under a forced oscillatory pressure field. The test apparatus and the majority of the diagnostics are the same as in the previous chapter. The focus of this chapter is on the enhanced spatial and temporal resolution brought about with the introduction of laser diagnostics and OH PLIF measurements, a more advanced technique than chemiluminescence.

5.1 Planar Laser-Induced Fluorescence of OH

5.1.1 PLIF Theory

Laser diagnostics have proven to be ideally suited to acquiring chemical species data. In particular, laser-induced fluorescence (LIF) is capable of resolving minor species concentrations at low parts-per-million (ppm) levels. According to Crosley (1993),

detection of the hydroxyl radical (OH) in an atmospheric flame is possible at sub parts-per-billion (ppb) concentration levels, with a spatial resolution of 1 mm^3 and a temporal resolution of 10 ns, with a signal level on the order of 100 photoelectrons. Other laser techniques such as Raman scattering (Masri et al. 1996) are sensitive to concentrations on the order of 1000 ppm, which are adequate for major species detection, but several orders of magnitude too high for minor species. Raman scattering is also limited by only providing point-wise measurements. Perhaps the major advantage of laser techniques is the ability to provide nonintrusive, in-situ measurements. The introduction of a physical probe will inevitably disturb the flowfield, distorting the physics of the experiment. Another issue to note is the difficulty for a physical probe to survive in a high temperature, high pressure combustion environment. The flexibility of laser diagnostics includes the capability of spreading the laser beam into a sheet. Planar laser-induced fluorescence (PLIF) can then be performed, yielding species information as a 2-D planar image, as opposed to LIF that resolves only a single point with each pulse.

PLIF and LIF operate on essentially the same principles, with the primary difference being the way in which data is collected. In an LIF system, a photomultiplier can be used as a detector, whereas PLIF requires an intensified CCD camera or some other detector that provides spatial resolution. Another obvious consequence is the need for additional optics to produce the laser sheet.

Laser-induced fluorescence involves three essential features. First, the species of interest must be brought to an excited electronic state, usually via a tunable-dye laser, pumped by

an Nd:YAG or Excimer laser. The excited molecules then fluoresce, by emitting photons and decaying to lower energy states. The emitted photon can be at the same wavelength as the excitation source, though this is not necessarily the case. In fact, it is more convenient if it is not, since detection can take place without interference from the laser source. The last step involves detection of the fluorescence signal. Figure 5-1 outlines schematically this process.

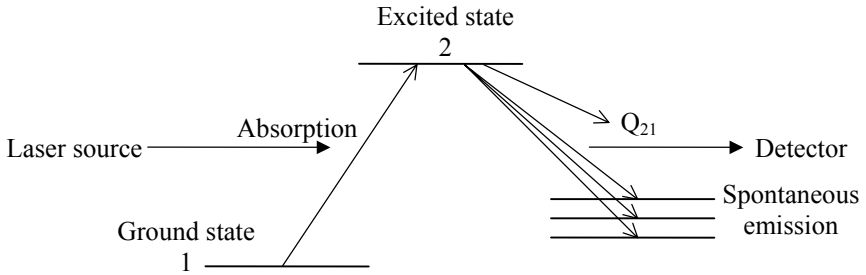

Figure 5-1: Simplified energy level transfer diagram for LIF.

The quenching (or collisional quenching) rate, Q, is of primary importance in determining the accuracy of LIF measurements. Quenching represents energy loss of the molecule by some pathway other than fluorescence. Possibilities include collision with other molecules, dissociation, ionization, chemical reaction, or even transitions to unmonitored molecular energy states.

A technique to avoid errors introduced by unknown quenching rates is to perform saturated LIF. This involves using a high intensity laser such that the quenching rate is small compared to absorption and stimulated emission rates. This has the additional advantage of maximizing the strength of the fluorescence signal that is detected. A problem of saturated LIF is the need for a high-powered, tunable laser with good beam quality. Further difficulties include the finite time required to achieve saturation and

subsequent relaxation of the probed species, especially when temporal accuracy is necessary (Eckbreth 1988). Depletion of the laser-pumped level also leads to fluorescence being a nonlinear function of population fraction (Seitzman and Hanson 1993).

An alternative to saturated LIF is to operate in the linear fluorescence regime. This allows for the use of comparatively low powered lasers, but does not eliminate the quenching dependence. Quenching rates can generally be modeled, but the modeling requires knowledge of the precise state of the system, such as temperature and concentrations of all other species. For single point measurements, Raman scattering can be used to determine major species concentrations, however this is not practical in a two-dimensional flowfield. Temperatures in the flowfield can be determined through a variety of techniques. Seeding the flow with a temperature sensitive tracer molecule such as NO, and performing PLIF on the tracer gas can yield temperature fields (Cadou 1996). Another popular method is use of a two-line technique, which measures the rotational temperature by ratio of the two fluorescence signals (Cattolica 1981; Lucht et al. 1982; Palmer and Hanson 1996). Rayleigh scattering can also yield a two-dimensional temperature field by measuring the density and inferring temperature. Combining Rayleigh scattering with a point two-line LIF measurement has been used to improve precision (Heberle et al. 2000).

A model for the collisional quenching of NO (Paul et al. 1994) and OH (Paul 1994) has been developed for flame environments. Comparisons with experimental results show

relatively good agreement with the empirical correlations proposed (Tamura et al. 1998). Making use of Paul's models, a successful technique for LIF of NO in high pressure (up to 10 atm) environments was developed by Battles and Hanson (1995).

According to Allen et al. (1995a), the fluorescence signal can be modeled by a two-level steady state model, and is given by

(5-1) $$S_f = \eta \left(\frac{\Omega}{4\pi}\right) V_c I_\nu \left[\frac{A_{eff}}{A + Q(\chi_P, P, T)}\right] \chi_j P_t \sum_i \left[f_{B,i}(\mathrm{T})\, B_i\, g_i(\nu, P, T)\right],$$

where:

η = quantum efficiency of ICCD photocathode

Ω = collection optics solid angle

V_c = collection volume of one detector pixel

I_ν = laser spectral fluence

A_{eff} = effective Einstein coefficient for spontaneous emission

A = Einstein coefficient for spontaneous emission

$Q(\chi_P, P, T)$ = electronic quenching rate

χ_j = mole fractions of measured species j, in measurement volume

Pt = total gas pressure

$f_{B,i}(T)$ = Boltzmann fraction of absorbing species in state i

B_i = Einstein coefficient for stimulated emission for transition i

$g_i(\nu, P, T)$ = overlap integral (convolution of absorption and laser lineshape profiles).

It is important to note in equation (5-1), that the fluorescence signal is directly proportional to the species mole fraction within the probed volume, and thus can be related to species concentration. Quenching can be accounted for through the use of the models of Paul previously mentioned. The quenching rate is defined as

(5-2) $$Q = \langle v_j \rangle \langle\langle \sigma \rangle\rangle P/k_B T,$$

where $\langle v_j \rangle = (8k_B T/\pi m_j)^{1/2}$ and $\langle\langle \sigma(\chi_P, T) \rangle\rangle$ is the total electronic quenching cross section, given by

(5-3) $$\langle\langle \sigma (\chi_i, T) \rangle\rangle = \sum_i \chi_i (1 + m_j/m_i)^{1/2} \langle\langle \sigma_i (T) \rangle\rangle .$$

These modeling efforts however still require detailed information regarding the species concentrations and temperature within the probed volume.

An alternative to modeling of the quenching rate and arguably superior is direct measurement of the fluorescence decay time as performed by Kollner and Monkhouse (1995) using point measurements and a picosecond laser. A similar approach is discussed by Cadou (1996) and also involves measurement of the fluorescence signal as it decays, since it provides a direct measurement of the quenching rate. This requires an extremely fast collection system, since the fluorescence signal decays on the order of a few nanoseconds. While this is possible for single point measurements with use of a photomultiplier tube, current multi-point detectors, such as intensified CCD cameras, do not possess the speed required to perform this measurement.

The primary purpose of applying a quenching correction is to provide quantitative species concentration information. Due to limitations in modeling and current equipment technologies, a quenching correction is a nontrivial task for this work. Previous work with methane diffusion flames has shown uncorrected LIF measurements of OH concentration to be within ± 10% of the actual value (Barlow and Collignon 1991). However, due to differences in the constituents and geometry of the reacting flow of this work, direct comparison is not possible. Since the primary purpose of this work is to provide relative measurements, a fully quantitative measurement is not required. Therefore, no attempt is made to correct for quenching effects in the flowfield.

5.1.2 Laser System

The PLIF system is based on an Nd:YAG laser (Continuum Powerlite 9010) operating at 10 Hz, pumping a tunable dye laser (Continuum ND6000), which in turn drives a mixer/doubler system (U-oplaz) as in Figure 5-2. The Nd:YAG laser outputs 2000 mJ/pulse at 1064 nm (IR), and is equipped with a secondary harmonic generation system to provide 1000 mJ/pulse at 532 nm (green). The 532 nm beam pumps the dye laser, while excess energy at 1064 nm (energy not converted to 532 nm) is passed through a delay line. The delay line allows the 1064 nm beam to coincide spatially and temporally with the output of the dye laser for frequency mixing purposes. The mixer/doubler system, shown in more detail in Figure 5-3, was custom designed in cooperation with Dr. Sheng Wu of U-oplaz Technologies, for optimal energy conversion by special tuning of the BBO crystals (Wu et al. 2000). Use of Rhodamine 590 as the dye laser in methanol optimizes conversion efficiency near 564 nm (> 200 mJ/pulse), which is then doubled to approximately 282 nm to excite the (1,0) band of OH (Dieke and Crosswhite 1962).

Energy in excess of 60 mJ/pulse is easily provided by this system, but this experiment did not require operation at full power, providing approximately 30 mJ/pulse in the measurement volume. This maintains fluorescence in the linear regime, and represents an ideal compromise between systemic error (~15%) and SNR (~ 3.4%) over other laser pumping options (Seitzman and Hanson 1993).

5.1.3 Optics

In order to take calibration shots of the laser beam profile, a method is employed which allows the beam energy to be "turned down" without changing the actual beam energy output (and also the beam characteristics) of the laser. This involves passing the beam through a zero-order half-waveplate (U-oplaz, coated for 285 nm) mounted on a rotatable stand (about the beam axis), which polarizes the beam to a particular orientation. The beam then passes through a thin film plate polarizer (CVI, TFP-280-PW-2025-UV). This allows the energy transmitted to vary from "full power" when the polarization is in line with the waveplate, to "minimum power" (approximately 3-4% of full power) when the polarizer is not aligned with the waveplate. Figure 5-4 gives more details of the optical arrangement. After the polarizer, a portion of the beam (approximately 2%) is split using a beamsplitter. Shot-to-shot laser energy is measured for each pulse with an energy meter (Molectron J9LP). The beam is then narrowed using a plano-concave cylindrical lens (radius of curvature = 100 mm), and spread into a sheet in the plane at 90° to the converging plane by a plano-convex cylindrical lens (radius of curvature = 25.43 mm). It should be noted that all beam steering is done using total-internal-reflection prisms, and all optics are UV grade fused silica, coated with an antireflective coating which minimizes reflections to less than 1% from 225 nm up to over 400 nm.

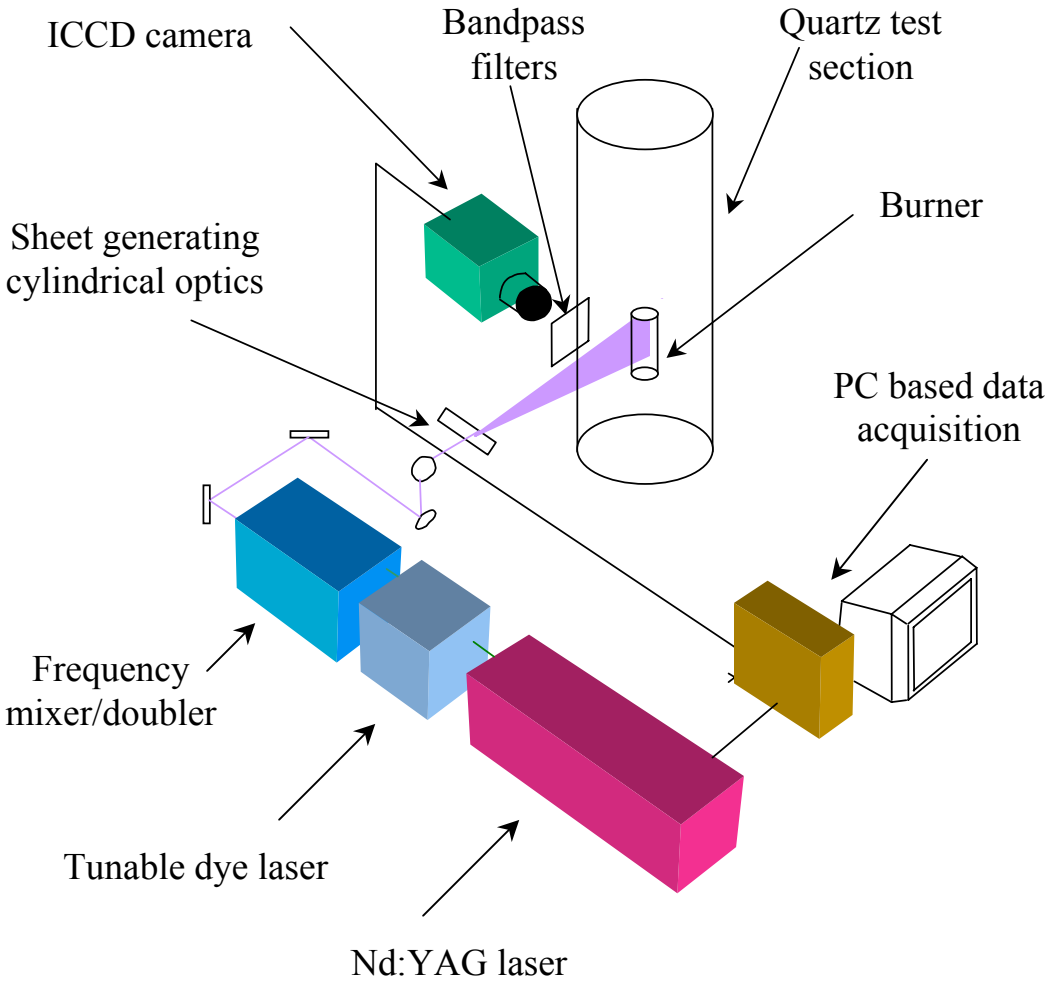

Figure 5-2: PLIF system.

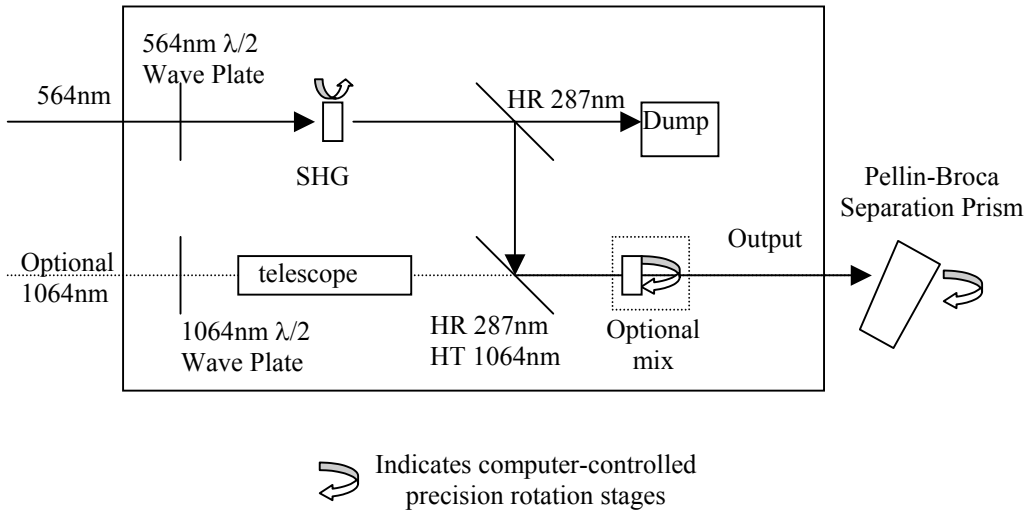

Figure 5-3: Mixer/doubler system (Stages available but not used are indicated by dashed lines).

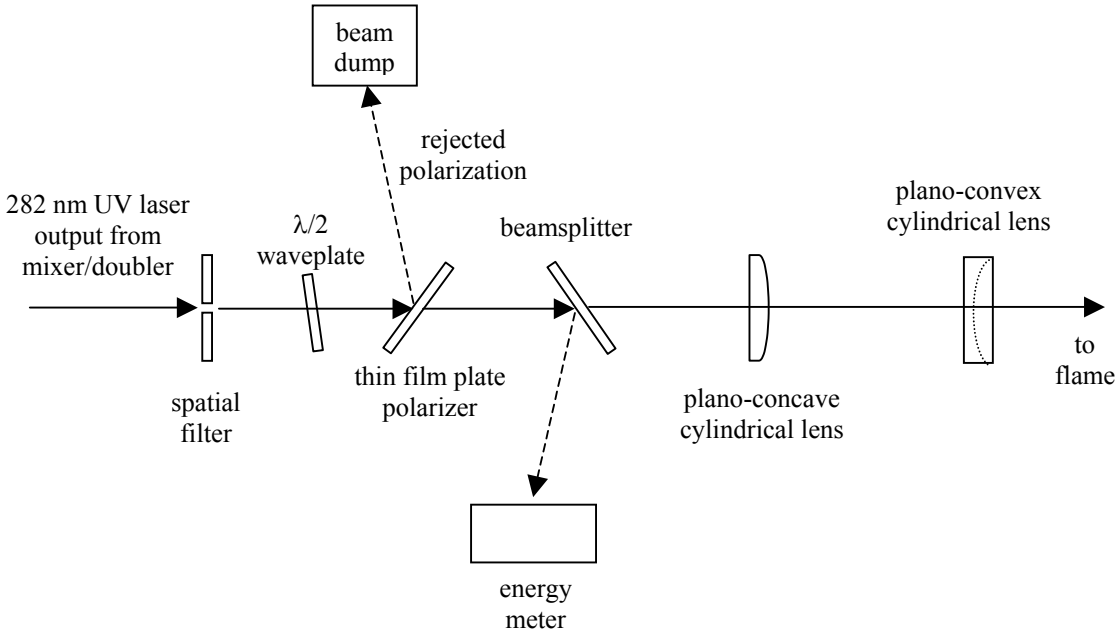

Figure 5-4: OH PLIF optics arrangement.

5.1.4 ICCD Camera

The detector for the fluorescence signal is an intensified CCD camera (Roper Scientific/Princeton Instruments ICCD-MAX), using a 512 x 512 Thomson CCD array, operated with a gate width of 200 ns. The photocathode used in the camera is a handpicked DEP "super-blue" model, for maximum quantum efficiency in the UV. Due to the requirement of high QE as well as fast gating, the microchannel plate (MCP) of the camera is gated, since the thin UV sensitive coating on the photocathode does not allow the intensifier to be gated quickly. Attached to the camera is a catadioptric (similar to Cassegrain telescope designs) all-reflective F/1.2 UV lens with a focal length of 105 mm. The lens provides exceptionally fast light throughout, as well as minimizing spherical and chromatic aberrations. This results in a spatial resolution of 215 μm x 215 μm per pixel at the focal plane with an image size of 11 cm^2. A 2 mm thick UG5 Schott glass filter to block light generated by the laser, and a 2 mm thick WG305 Schott glass filter to remove light generated by flame luminosity and ambient sources filter the fluorescence signal. A digital delay/pulse generator (Stanford Research Systems DG-535) controls camera timing, which is synchronized to the laser pulse.

Particular benefits of this PLIF system include flexibility, exceptionally high energy output, conversion efficiencies, and collection efficiencies. Other molecules of interest to combustion can be readily probed using this system such as CH and NO, with much higher energy levels than previous researchers (Hanson et al. 1990; Allen et al. (1995a)).

5.2 Experimental Procedure

The following steps outline the general procedures followed in conducting the combustion dynamics experiments.

1. Laser setup.
    - Verify the calibration of the dye laser, either with a wavemeter or an opto-galvanic (OG) cell.
    - Optimize the mixer/doubler tuning crystal angles for maximum energy conversion.
2. Setup necessary gas flows.
    - Air jacket flow over acoustic drivers.
    - Nitrogen purge through ICCD camera.
3. Optics alignment.
    - Focus the ICCD camera on a card in the test section. Ensure the laser sheet is passing through the probed volume cleanly. This is done with the aid of the ICCD camera taking focusing images so scattered light from the laser sheet can be minimized.
4. Beam profile calibration.
    - Minimize laser energy throughput using the waveplate. Set camera gain to 1, and gate width to 10 ms.
    - Allow laser sheet to impinge on fluorescent card and acquire the beam profile with the ICCD camera, placing card in three different positions (left, center, right).

- Return camera gain to 200, and gate width to 200 ns and waveplate to allow maximum laser energy throughput.

5. Take background images.
   - Typically 200 images with no flame, but with the laser sheet passing through the test section.
6. Set experimental conditions.
   - Light burner and set methane and carbon dioxide flow rates (see Appendix B for more details).
   - Set acoustic driver power on controller, and activate drivers.
   - Allow laser sheet to pass through test section.
7. Perform experimental run (duration approximately three minutes).
   - Start LabView data acquisition program.
   - Start WinView camera imaging software, typically taking 300 images (limited by system RAM).
8. End experimental run.
   - LabView and WinView routines end automatically. Save camera images to hard drive (takes several minutes due to file size).
   - Turn off fuel and CO_2 flows, extinguishing the flame.
   - Turn off acoustic drivers.
9. Repeat experiment.
   - Repeat steps 6-8 until more than 5000 images have been acquired at a particular test condition.
10. Take post-run background images.

11. Take post-run beam profile calibration images.
12. Change experimental conditions.
    - Changes may include drive frequency, burner height, or burner configuration.
    - Repeat steps 4-11 until experimental session is complete.
13. Shutdown systems.

After the experiments have been performed, the raw data files are zipped and burned to CD-ROM for archival purposes. The data is then ready for post-processing, described in the next section.

5.3 Data Reduction

5.3.1 Phase Characterization

By taking advantage of the periodic forcing of the chamber, and assuming that the flame responds accordingly in a periodic fashion, the PLIF images can be phase-binned and averaged together, to generate the periodic response of the OH fluorescence in the flame. As previously mentioned, the oscillating pressure used to phase-resolve the images is acquired by a pressure transducer located 8 cm above the fuel spud, in the zone where the flame is stabilized. The transducer signal is filtered about the fundamental driving frequency using a phase preserving 4th order butterworth bandpass filter in Matlab, to produce a clean signal with which to phase-bin. Each image is placed in an appropriate bin, based on the position of the incident laser shot (and subsequent camera trigger) relative to the rising edge zero crossing of the pressure signal. This process is illustrated schematically in Figure 5-5 using 8 bins, while in the actual data analysis, 36 bins are used. Since the hydroxyl radical is an intermediary of combustion and thus an indicator

for the reaction zone in the flame, this procedure yields a proportional measurement of the heat release over a period of the acoustic driving cycle.

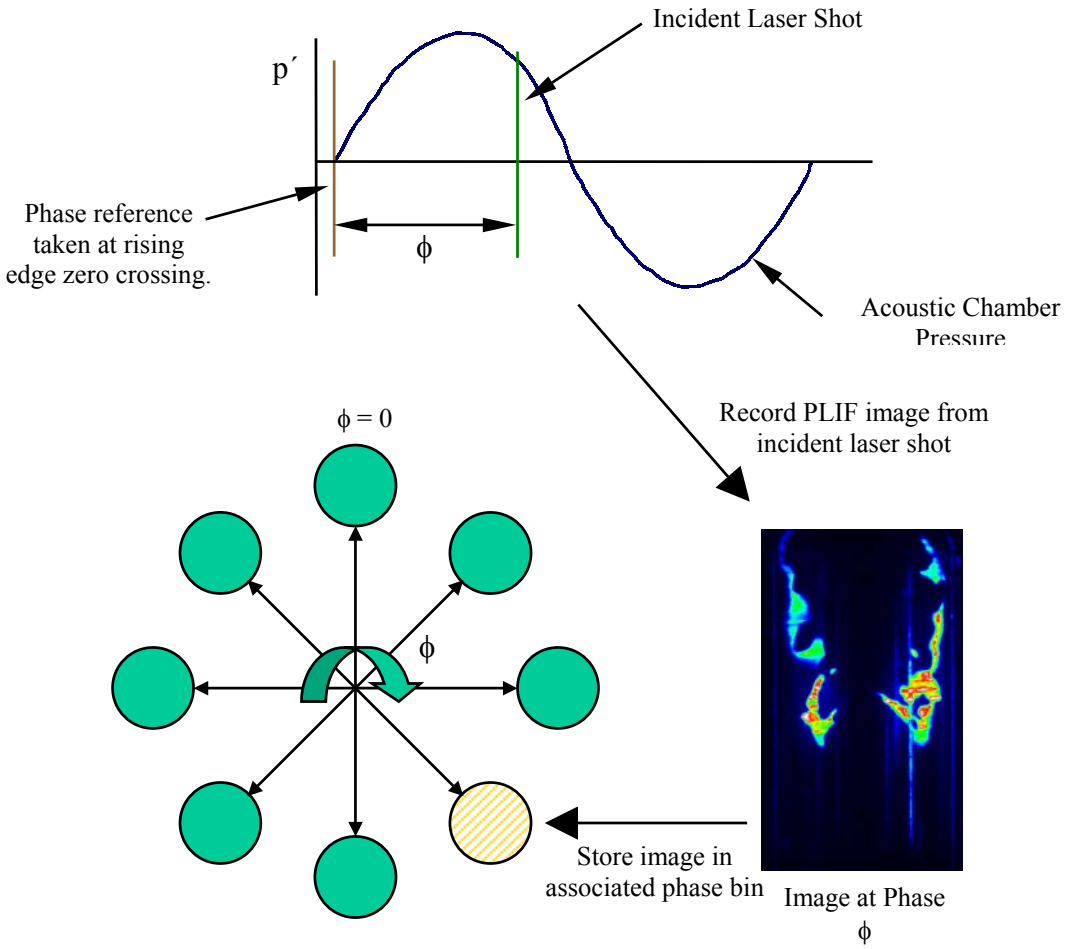

Figure 5-5: Phase-binning procedure for OH PLIF images.

5.3.2 Image Processing

Due to the distributed nature of the flame under study and limitations on the ICCD camera's field of view, multiple sets of images were taken at each test condition at different heights. Each case contains a total of over 5000 images, phase-averaged into 36 equally spaced bins. Statistics indicate an even distribution among the bins, with well

over 100 images per bin. The averaged background is subtracted in each bin to eliminate scattering effects from the laser; and corrections are made for variations in spatial and shot-to-shot beam intensity. Images at the same phase but different heights are then matched geometrically, and their intensities adjusted to match in the overlap region using a least-squares minimization routine. The composite images are then smoothed using a filter, using the weighting matrix given in Table 5-1. The weight is determined by the inverse of the distance to the center pixel. Stronger smoothing is done in the y-direction, the direction of the flow. Further details regarding the software written to perform these processes can be found in Palm (*in progress*).

$1/\sqrt{5}$	1/2	$1/\sqrt{5}$
$1/\sqrt{2}$	1	$1/\sqrt{2}$
1	1	1
$1/\sqrt{2}$	1	$1/\sqrt{2}$
$1/\sqrt{5}$	1/2	$1/\sqrt{5}$

Table 5-1: Smoothing filter weighting matrix.

5.4 OH PLIF Results

5.4.1 Pressure and Heat Release Measurements

Phase-averaged images for 12 of the 36 bins are displayed in Figure 5-6 for a representative case of the aerodynamically stabilized burner, driven at 32 Hz. The relative change between images is more easily observed by noting the variation in intensity over the lower right quadrant of each image. Spatial integration of the phase-

averaged OH PLIF images gives a "global" heat release at each phase angle. Plots of chamber pressure and the computed global heat release, and their corresponding FFTs are shown in Figure 5-7 through Figure 5-16.

It is evident from plots of the lowest frequency of 22 Hz (Figure 5-7 and Figure 5-8) that the pressure signals contain much more harmonic content than the fundamental frequency. Limitations of the response of the acoustic drivers at low frequencies account for the excitation of higher harmonics. Data at the 27 Hz condition show a similar, although largely attenuated effect. Once frequencies reach 32 Hz, the pressure traces are relatively clean, and show almost no harmonics. These effects are common for both the aerodynamically and bluff-body stabilized configurations.

In general, the FFTs of heat release show a response at the same driving frequency as the excited acoustic mode. Figure 5-7 through Figure 5-10 (22 Hz & 27 Hz cases) show higher harmonic content virtually identical in both the pressure and heat release. At driving frequencies greater than 27 Hz, the heat release contains elevated levels of higher harmonic content, which does not appear in the pressure traces. In both 32 Hz cases, the additional frequency content other than the fundamental in the heat release traces is minimal. However, the 37 Hz cases contain significant amounts of higher frequency heat release content, particularly at the 2nd mode of the system at 74 Hz. This result is most clearly evident at 55 Hz in Figure 5-15 and Figure 5-16, which show the ringing of higher frequency modes over the fundamental mode of heat release at this driving frequency. In

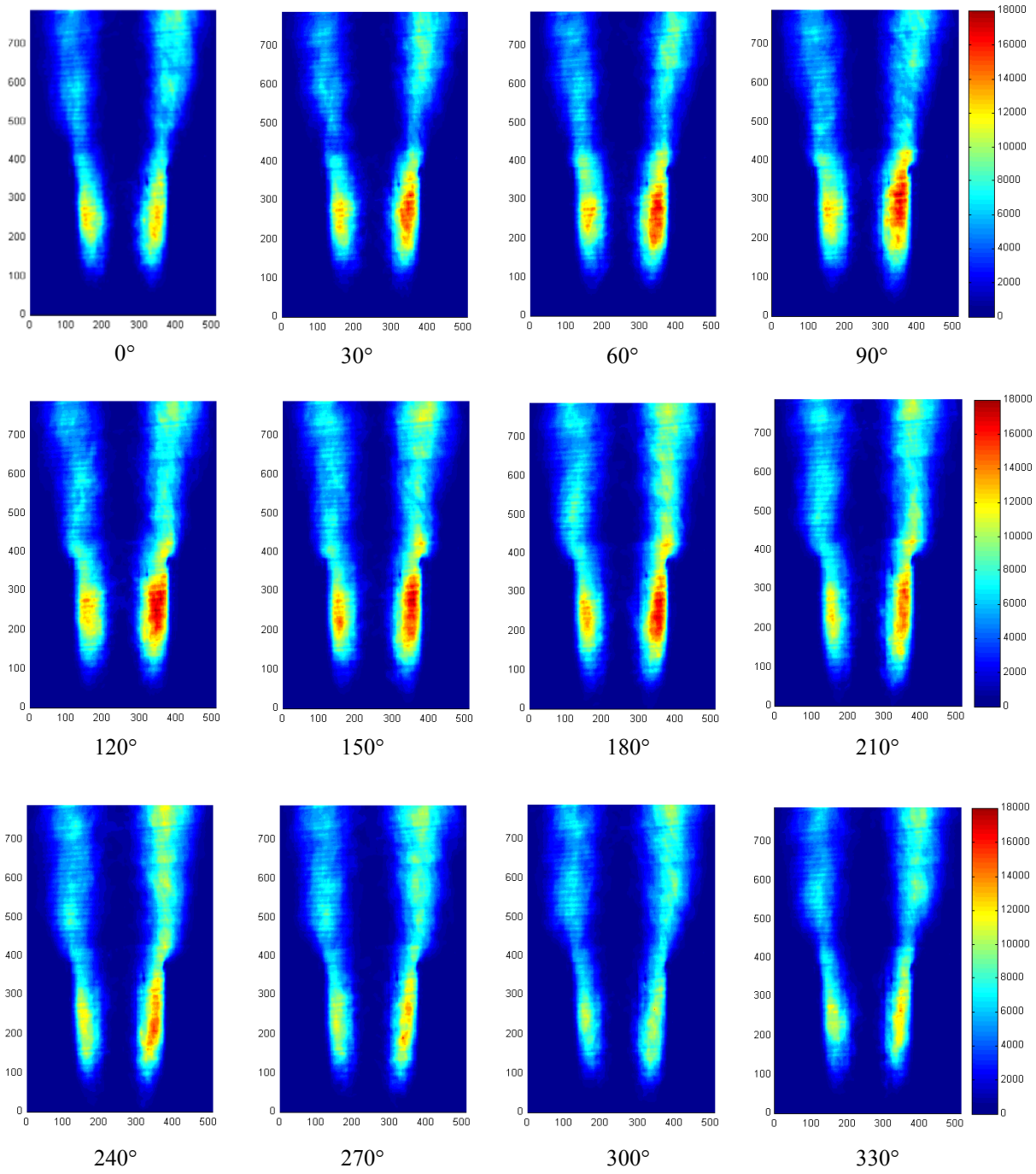

Figure 5-6: OH PLIF images over a period of a sinusoidal pressure oscillation for the aerodynamically stabilized burner at 32 Hz. The intensity scale is in number of counts, and the x and y coordinates are in pixels.

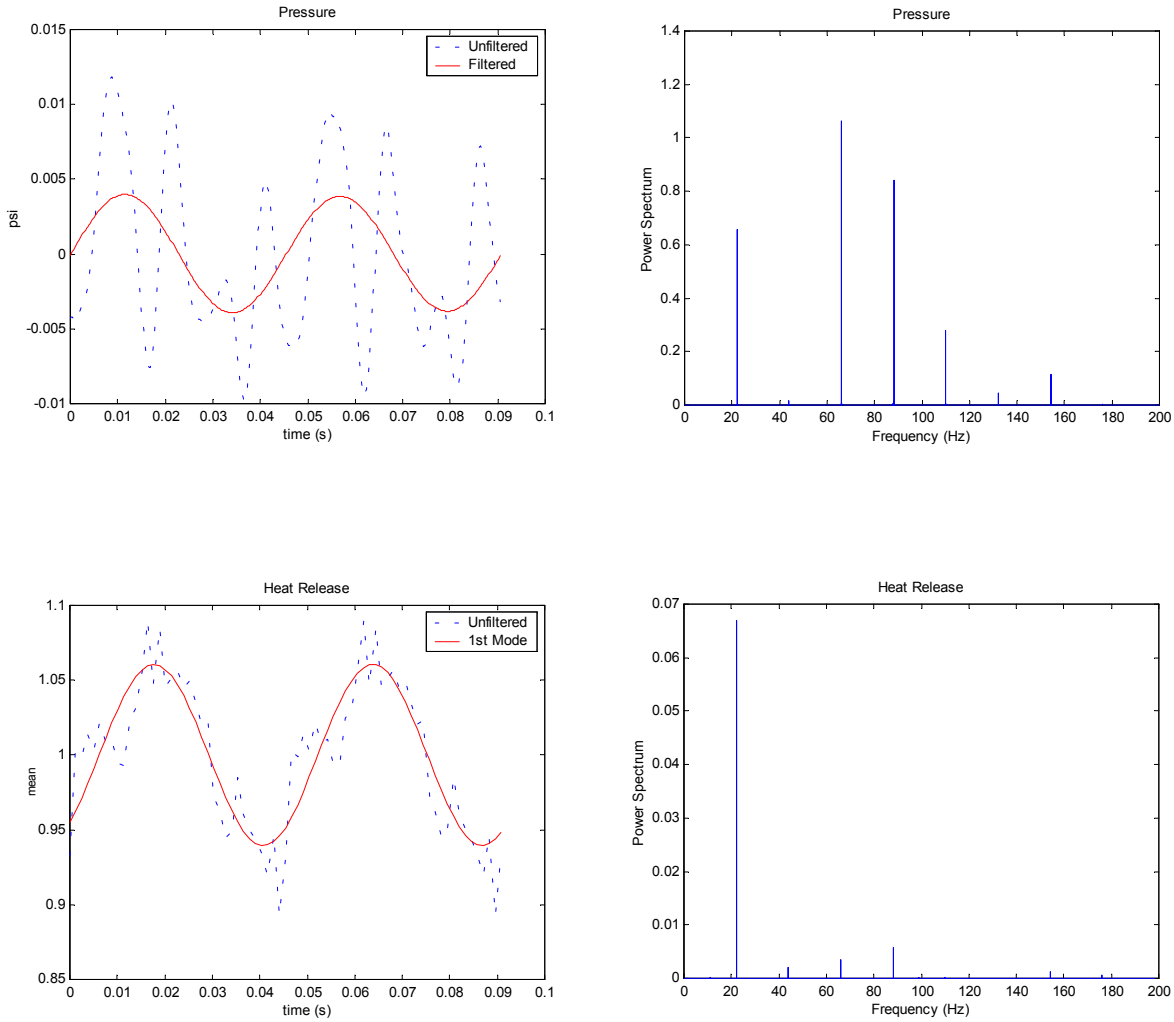

Figure 5-7: Pressure and heat release traces and power spectrums for the aerodynamically stabilized burner driven at 22 Hz.

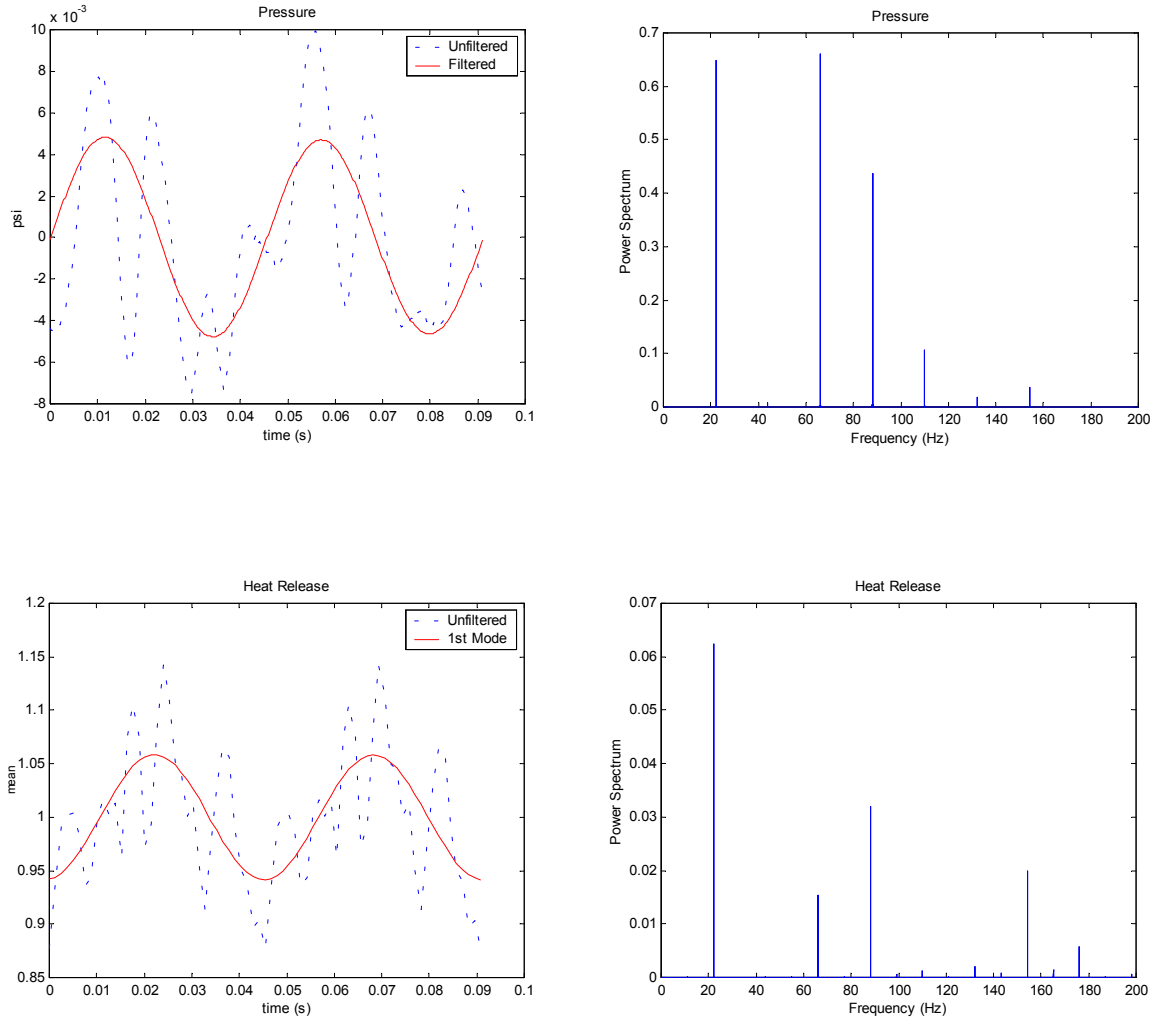

Figure 5-8: Pressure and heat release traces and power spectrums for the bluff-body stabilized burner driven at 22 Hz.

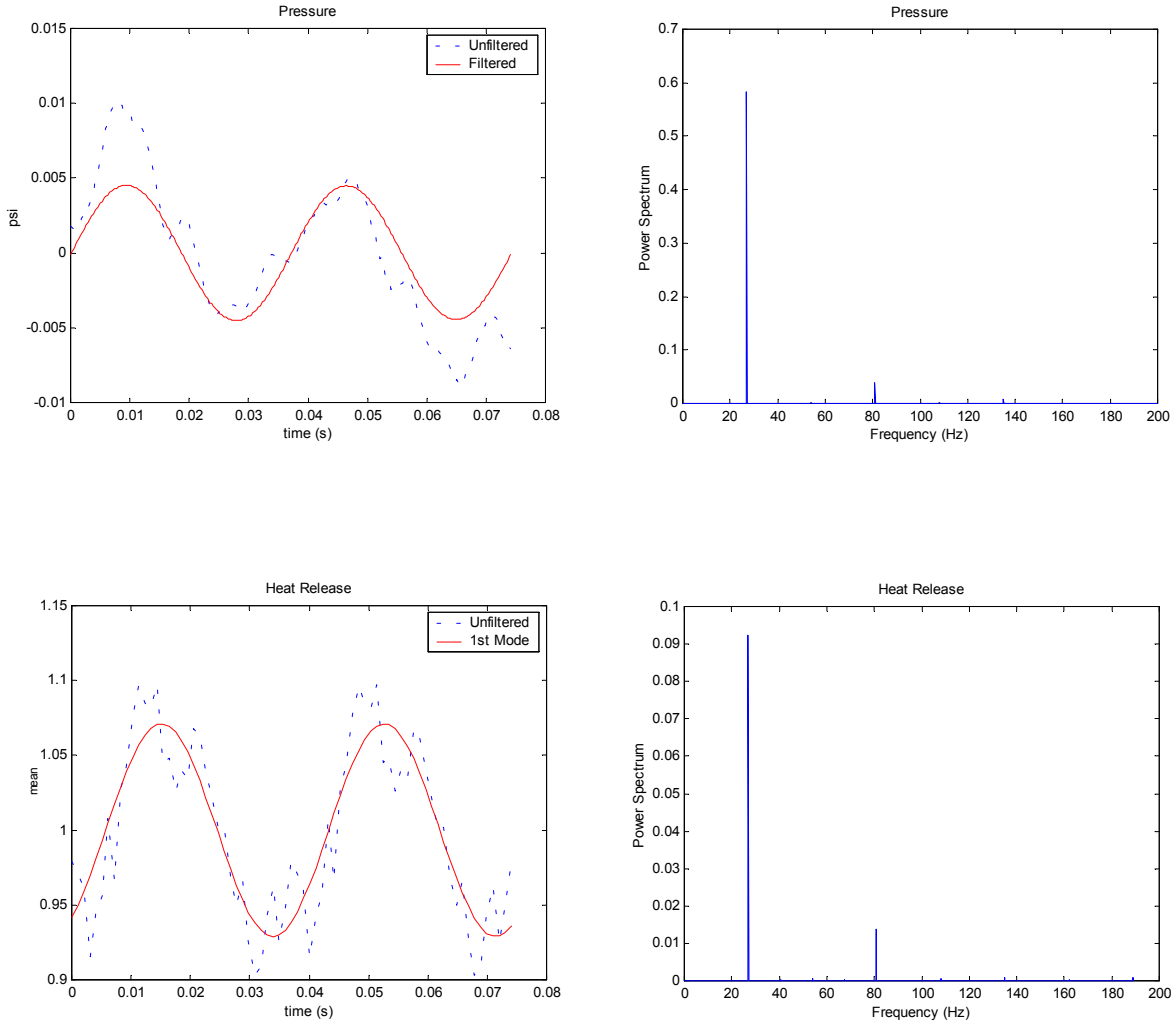

Figure 5-9: Pressure and heat release traces and power spectrums for the aerodynamically stabilized burner driven at 27 Hz.

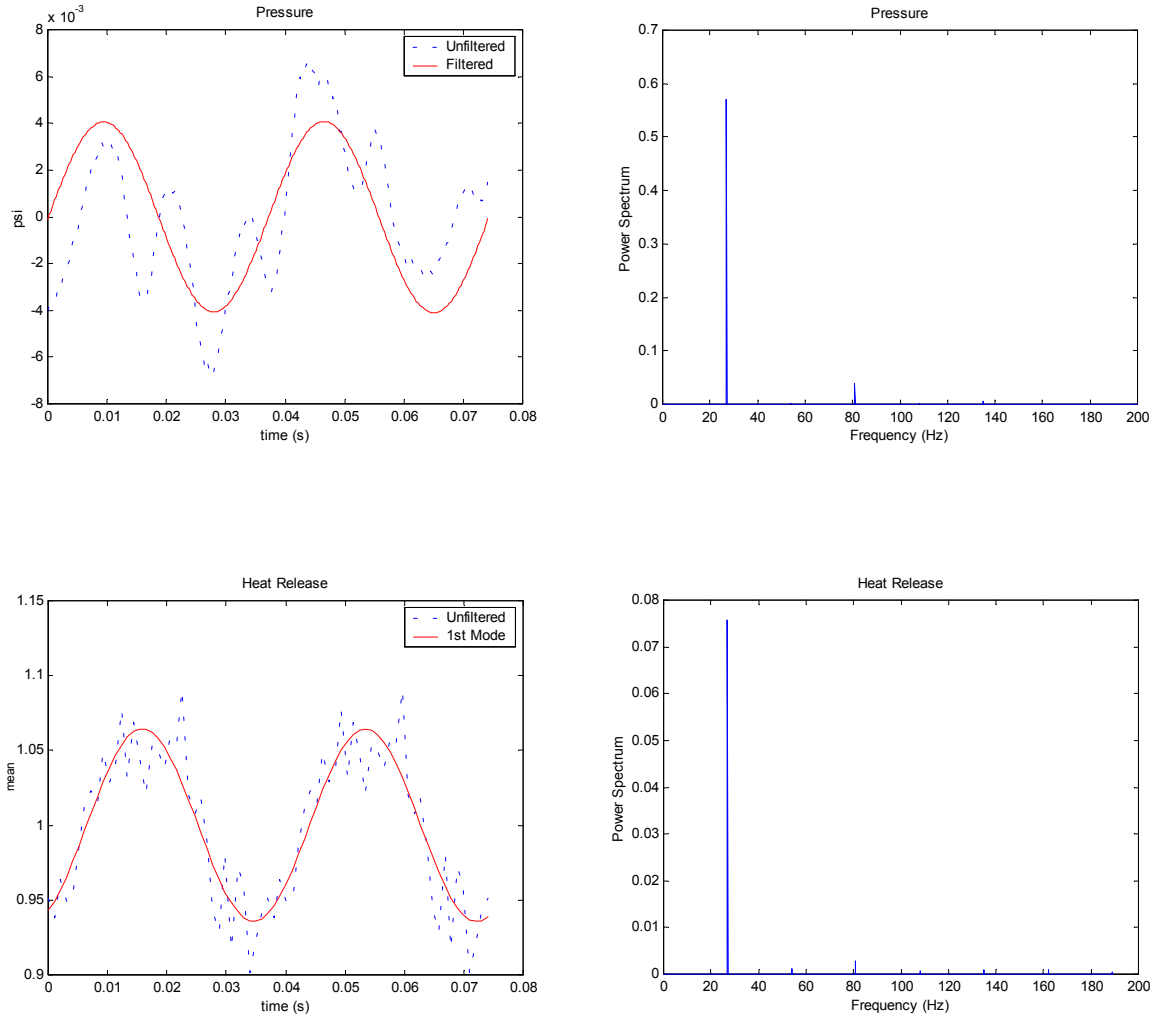

Figure 5-10: Pressure and heat release traces and power spectrums for the bluff-body stabilized burner driven at 27 Hz.

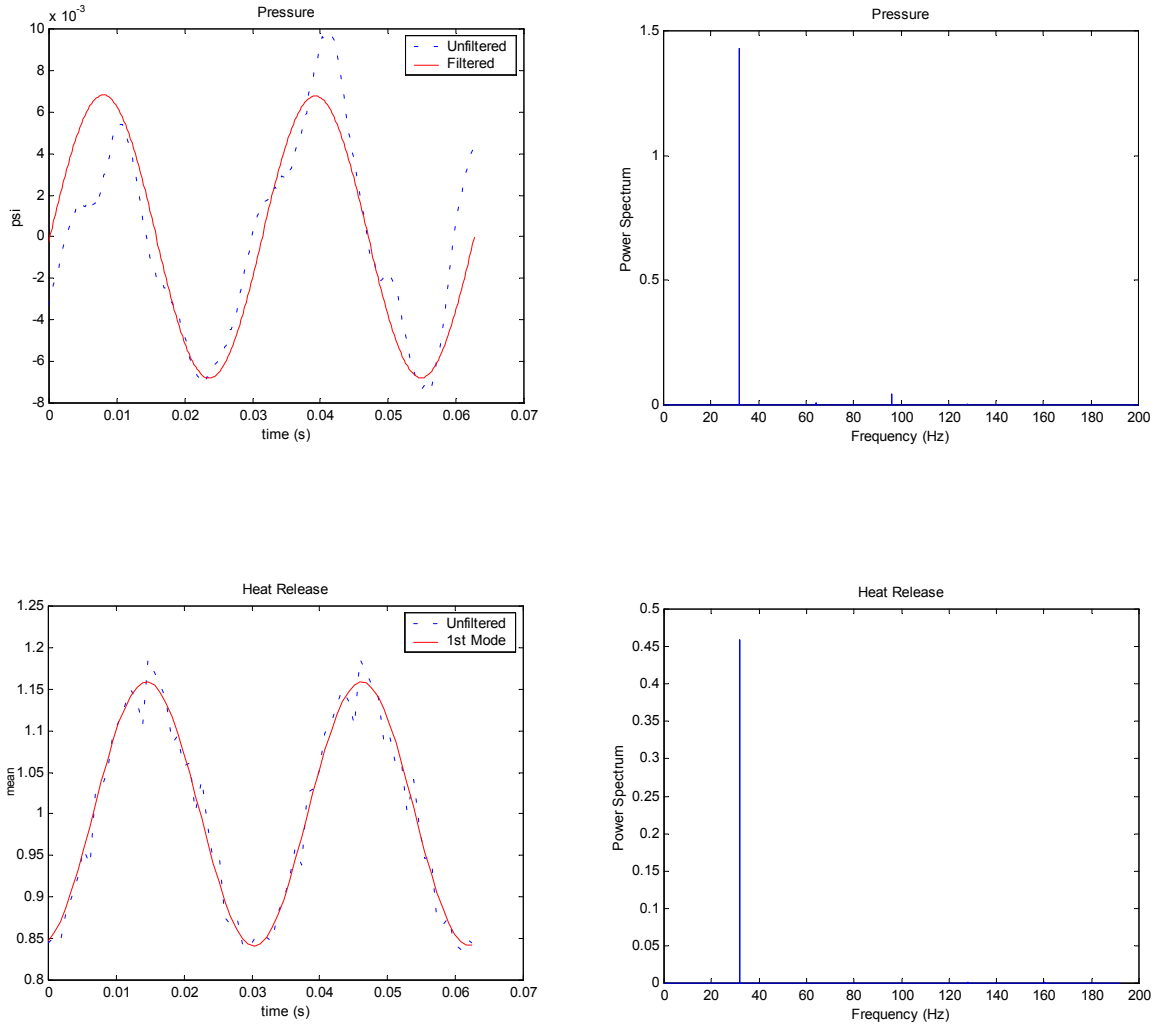

Figure 5-11: Pressure and heat release traces and power spectrums for the aerodynamically stabilized burner driven at 32 Hz.

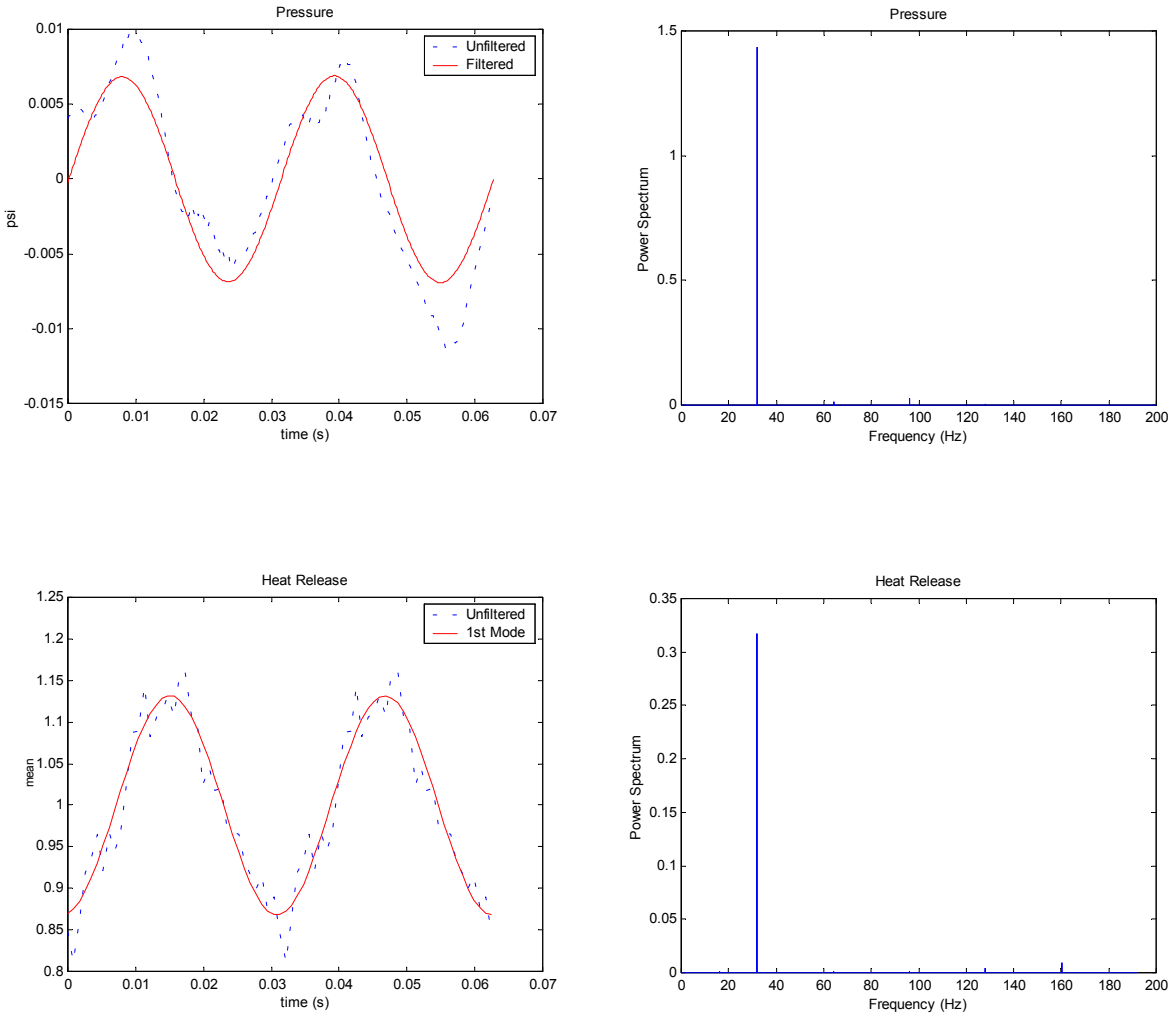

Figure 5-12: Pressure and heat release traces and power spectrums for the bluff-body stabilized burner driven at 32 Hz.

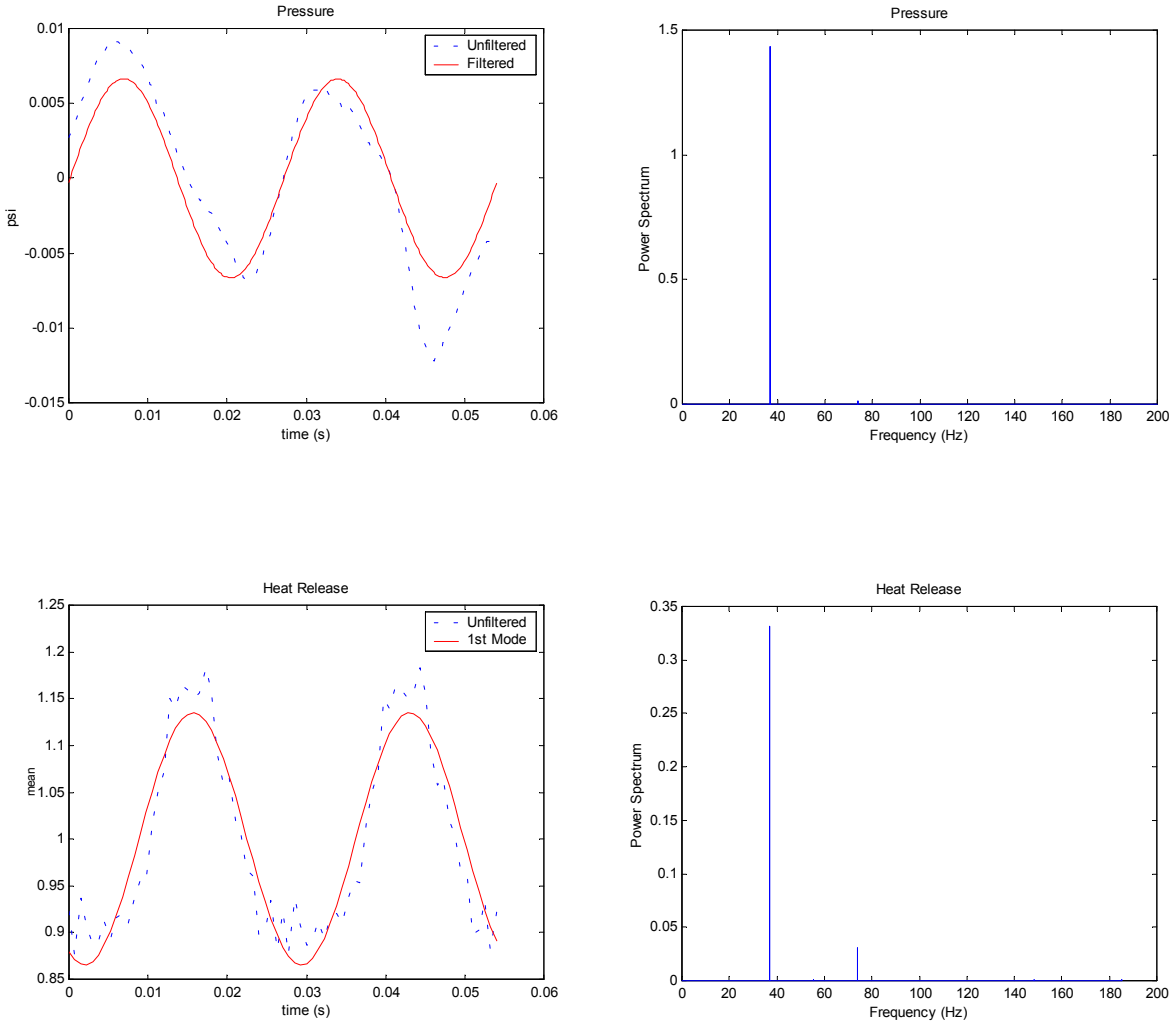

Figure 5-13: Pressure and heat release traces and power spectrums for the aerodynamically stabilized burner driven at 37 Hz.

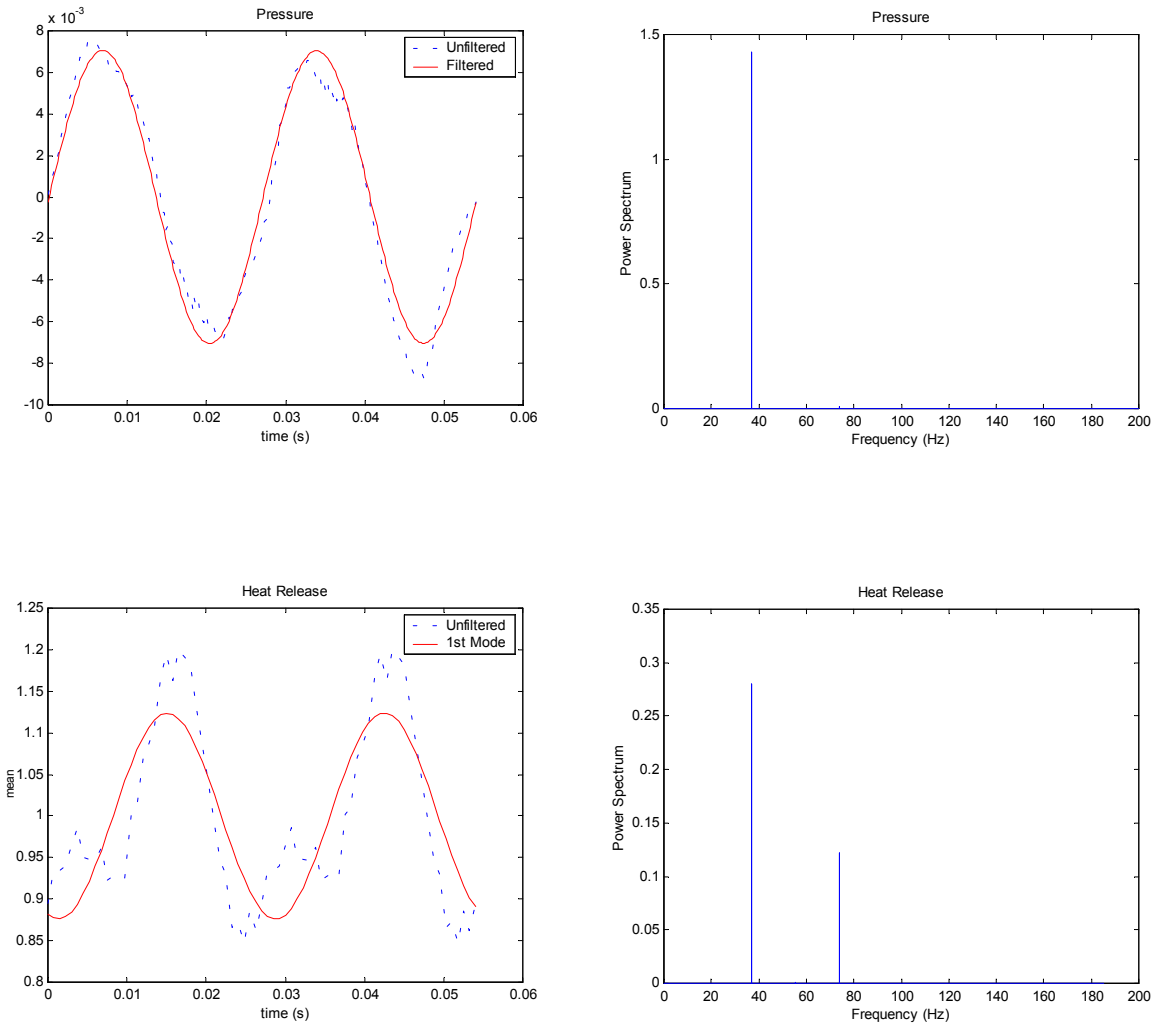

Figure 5-14: Pressure and heat release traces and power spectrums for the bluff-body stabilized burner driven at 37 Hz.

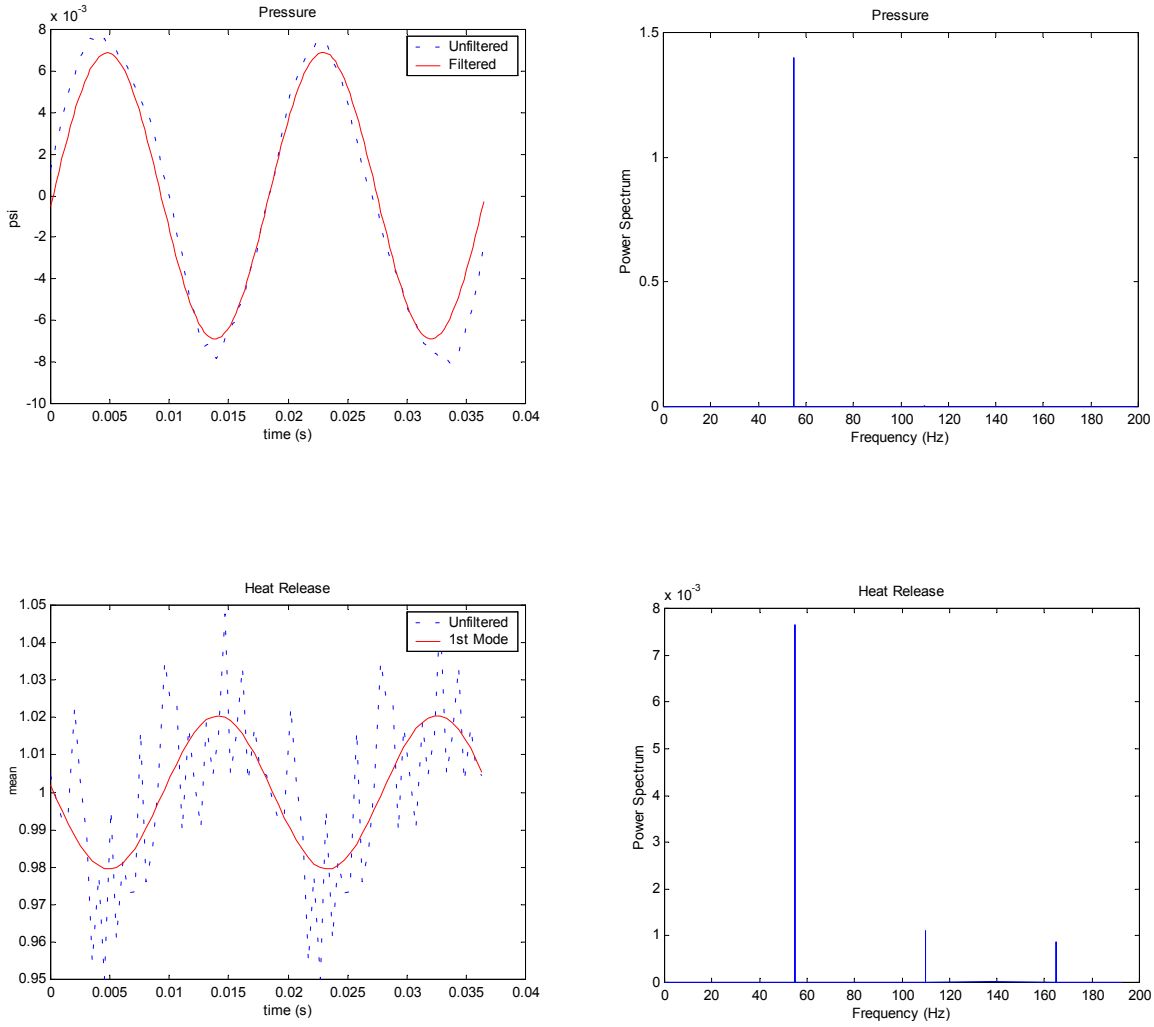

Figure 5-15: Pressure and heat release traces and power spectrums for the aerodynamically stabilized burner driven at 55 Hz.

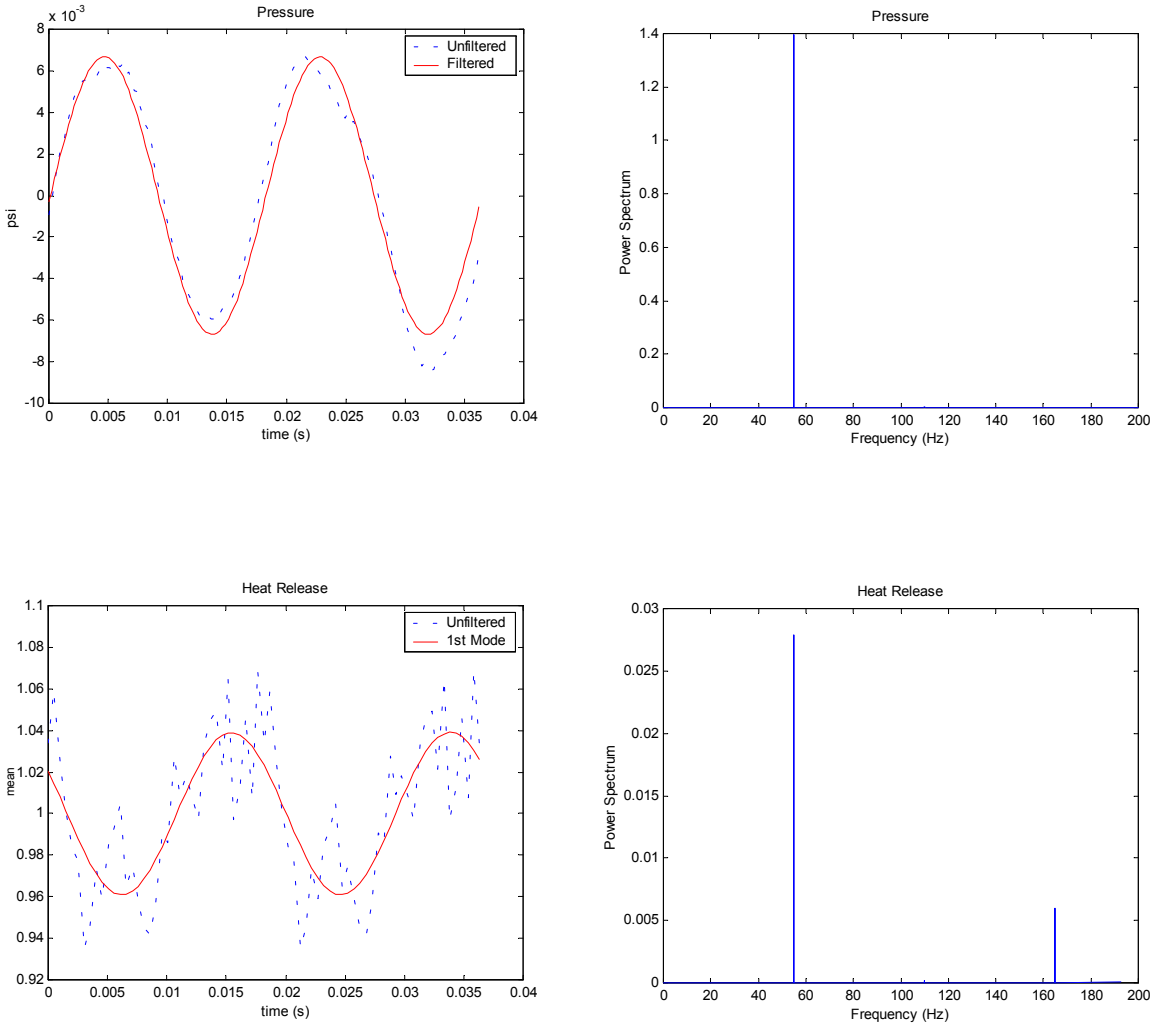

Figure 5-16: Pressure and heat release traces and power spectrums for the bluff-body stabilized burner driven at 55 Hz.

this case, the aerodynamically stabilized case shows the 2nd and 3rd modes, while the bluff-body case displays only significant content of the 3rd mode.

The FFTs of pressure and heat release contain amplitude and phase information of their respective signals. This information can be extracted at a particular frequency, by inverse FFT of the peak at the frequency under consideration. A representative plot is shown in Figure 5-17, displaying the relationship (scaled for comparison) between the first mode of heat release and pressure. Figure 5-17 (a) displays the relative phases for an aerodynamically stabilized burner subjected to acoustic forcing at 22 Hz, and Figure 5-17 (b) displays the relative phases for the bluff-body stabilized case. It can be noted that the bluff-body case shows a larger phase difference between the pressure and heat release than the aerodynamically stabilized case. This concept will be explored in more detail in the next section with respect to Rayleigh's criteria.

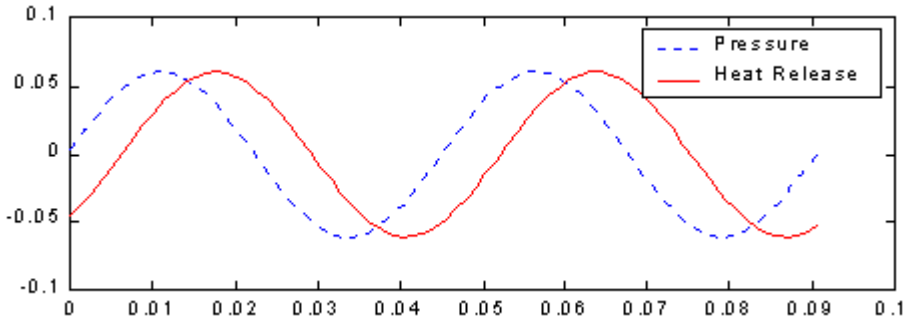

(a)

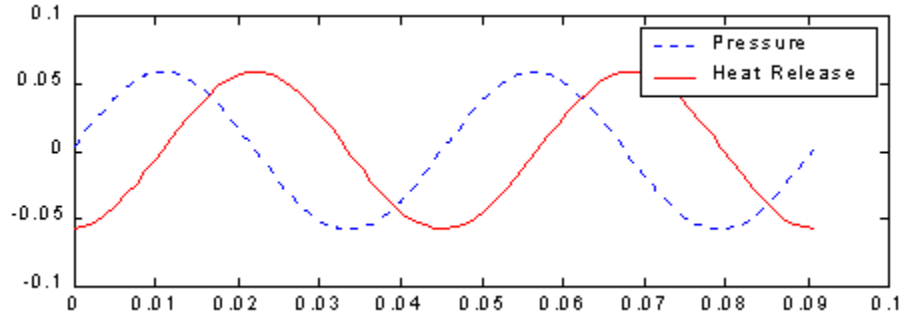

(b)

Figure 5-17: Phase relationship between the 1st mode of pressure and heat release for the (a) aerodynamically stabilized and (b) bluff-body stabilized cases at 22 Hz. Heat release traces have been scaled for ease of comparison.

5.4.2 Forced Rayleigh Index

As stated in section 4.5.3, the forced or frequency-driven Rayleigh is defined as

(5-4) $$R_f = \int_0^1 \frac{p'q'}{p_{rms}\bar{q}} d\xi \,,$$

where p_{rms} is the root-mean-square of the amplitude of the driving pressure wave, and $\bar{q}$ is the mean intensity of the heat release. p' is redefined as the driving pressure amplitude, and q' becomes the fluctuation in heat release. The time dependence has been normalized by the period of the driving acoustic wave, T, to give a nondimensional time ξ. Again, R_f can be applied globally to a system or locally to produce spatially resolved maps of Rayleigh indices.

5.4.3 Global Rayleigh Results

R_f can be computed directly for the system with the phase relationship between heat release and pressure. Since the heat release varies both spatially and temporally (while the pressure is assumed to vary only temporally), it is important to define how the heat release is calculated in the modified Rayleigh index, equation (5-4). For the global results, the heat release is first calculated according to

(5-5) $$q'(\xi) = \int_0^{L_x}\int_0^{L_y} q'_{2D}(\xi, x, y)\, dy\, dx \,,$$

where q' is the spatially integrated heat release of the spatially resolved quantity, q'_{2D}. In order to evaluate contributions from modes other than the driving frequency, R_f is calculated in two ways: directly from the pressure and heat transfer global response; and

for a pressure signal that has been bandpass filtered about the fundamental driving frequency.

The forced global Rayleigh index is plotted in Figure 5-18. In general, the bluff-body (1st pressure mode filtered) stabilized configuration is less sensitive to changes in the pressure field than the corresponding aerodynamically stabilized counterpart. This manifests itself as a frequency-driven global Rayleigh index with a lower magnitude. The requirement of filtering the pressure about the primary excitation frequency is justified, since the dynamic response of the flame is sought at a particular frequency, without the additional harmonics introduced through inadequacies of the acoustic drivers. This is especially apparent at a frequency of 22 Hz, which shows the discrepancies between results for the aerodynamically stabilized burner when the first mode is filtered, and when it is not.

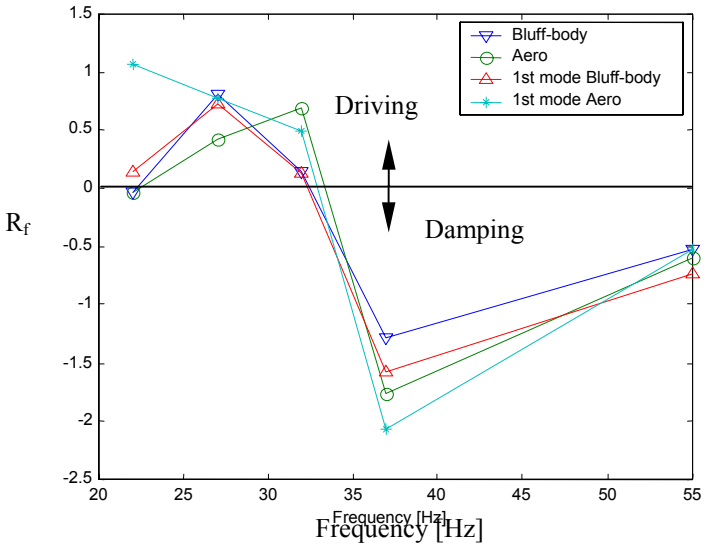

Figure 5-18: Frequency driven global Rayleigh index.

5.4.4 Spatially Resolved Rayleigh Results

The pressure field generated in the chamber is a bulk mode (established in the previous chapter), resulting in a relatively uniform pressure over the reaction zone at each phase. This allows a 2-D map of Rayleigh's criterion to be computed, using the assumption of uniformity in pressure in the chamber at a particular instant in time. Note that the flame may introduce its own pressure oscillations associated with the dynamical response the flame has to the bulk pressure field. The 2-D map will give insight into which zones in a particular configuration are more susceptible to acoustic oscillations.

Figure 5-19 through Figure 5-23 are contour plots of the 2-D forced Rayleigh index, R_f for both the aerodynamically and bluff-body stabilized cases, at each of the five forcing frequencies examined. Solid contours represent positive values for R_f (driving), while negative values are indicated by the dashed contours (damping). For the first four frequencies (22-37 Hz), the contour levels are [-20, –10, –4, –2, 2, 4, 10, 20]. Due to significant differences in the dynamical response of the system at 55 Hz, contour levels of [-3, –1.5, 1.5, 3] were used for clarity. In all cases, the pressure has been band pass filtered about the fundamental of the driving frequency.

Comparison of Figure 5-19(a) and Figure 5-19(b) denotes the differences between the aerodynamically stabilized and bluff-body stabilized cases at 22 Hz. The bluff-body tabs appear to induce a stronger recirculation zone in the stabilization region at the base of the flame, resulting in the flame stabilizing at a lower height and with more (negative) intensity. This region is less susceptible to instability than the aerodynamically stabilized

case. In the positive region, the strong "level +10" contours are smaller than in the bluff-body case, with the positive region in general being slightly smaller than the aerodynamic situation. Note it is possible to observe the quartz burner tube, which ends at approximately 8 cm in height, before the flame diverges. In the region where the flame diverges, there is a large negative R_f in both cases. These trends are also observed as the driving frequency is increased to 27 Hz in Figure 5-20, but with the disparities in sizes of the positive regions becoming more pronounced, and heights of the flame stabilization zone becoming less pronounced. By Figure 5-21 at 32 Hz, the penetration of the positive region in the central core of the flame has been greatly decreased, and differences in the flame stabilization height have disappeared. The highest positive contours of R_f are found at 32 Hz, but the diminished size of the positive zone, combined with the appearance of larger negative zones do not produce as large global Rayleigh indices as the 27 Hz case (Figure 5-18). As the driving frequency is increased to 37 Hz (Figure 5-22), the positive zone contributions to the frequency-driven Rayleigh index have decreased further in size. Once the acoustic frequencies have reached 55 Hz in Figure 5-23, the character of the Rayleigh contour plot changes dramatically. The large positive structures have vanished in the center of the flame and are replaced by large, relatively low amplitude negative zones.

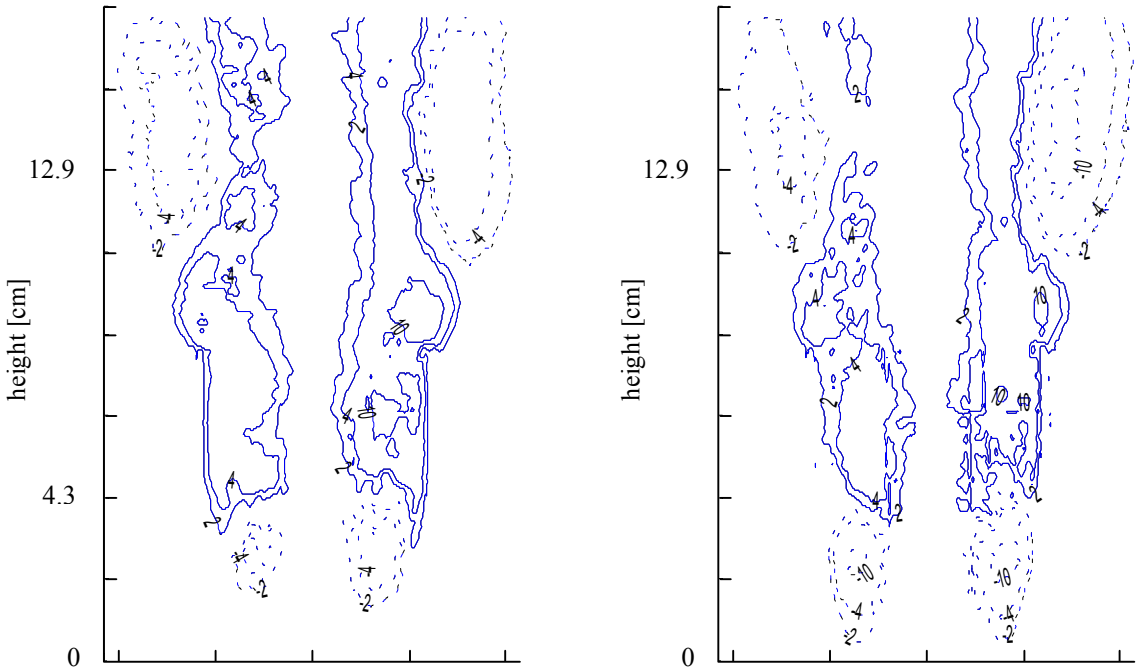

Figure 5-19: Contour plot of R_f for (a) aerodynamically and (b) bluff-body stabilized burners at a driving frequency of 22 Hz.

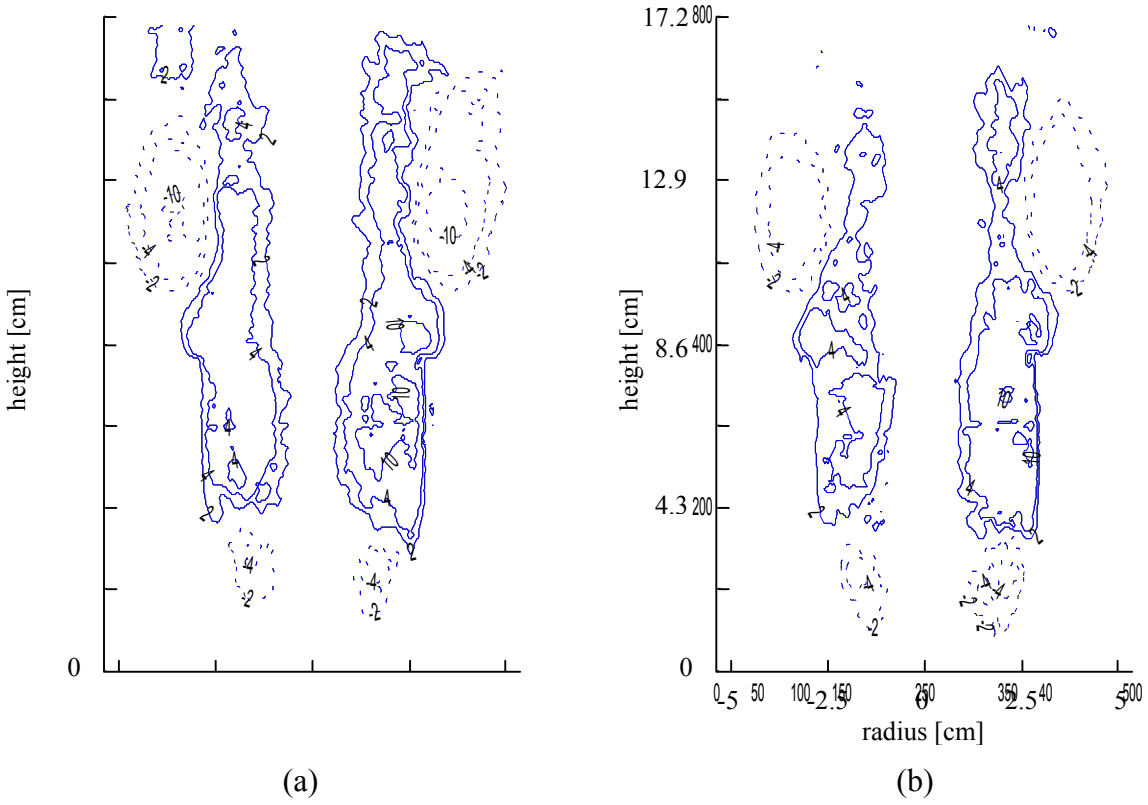

Figure 5-20: Contour plot of R_f for (a) aerodynamically and (b) bluff-body stabilized burners at a driving frequency of 27 Hz.

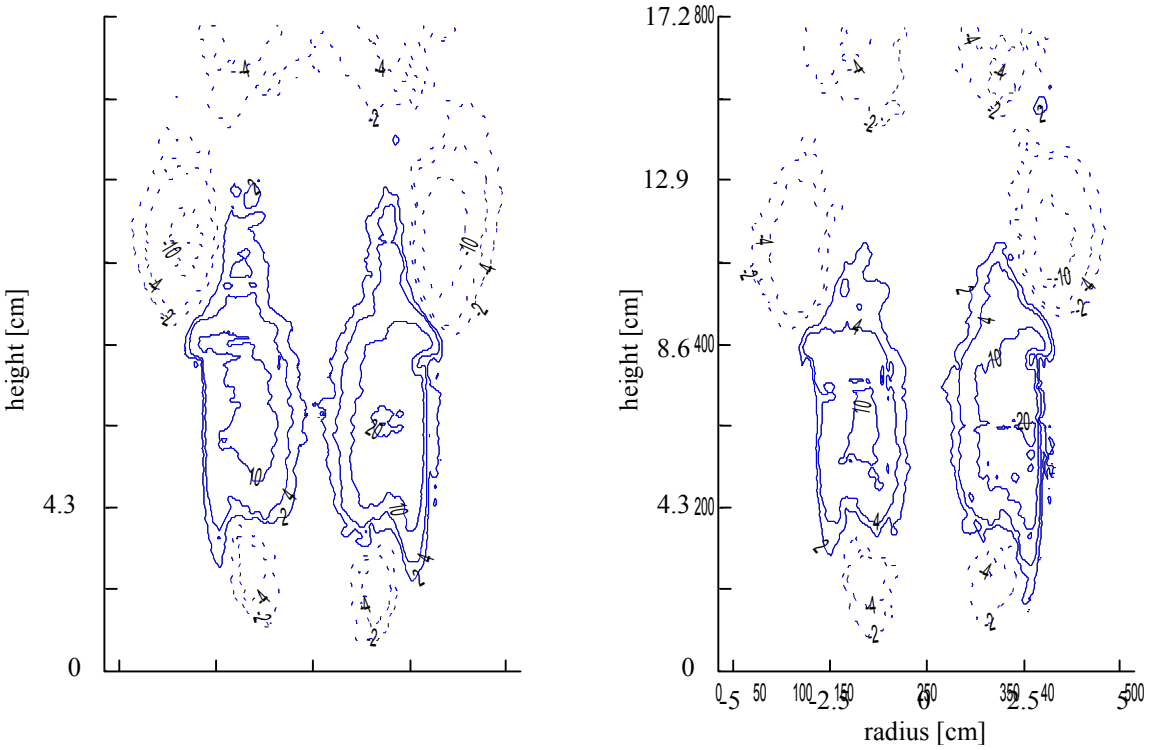

Figure 5-21: Contour plot of R_f for (a) aerodynamically and (b) bluff-body stabilized burners at a driving frequency of 32 Hz.

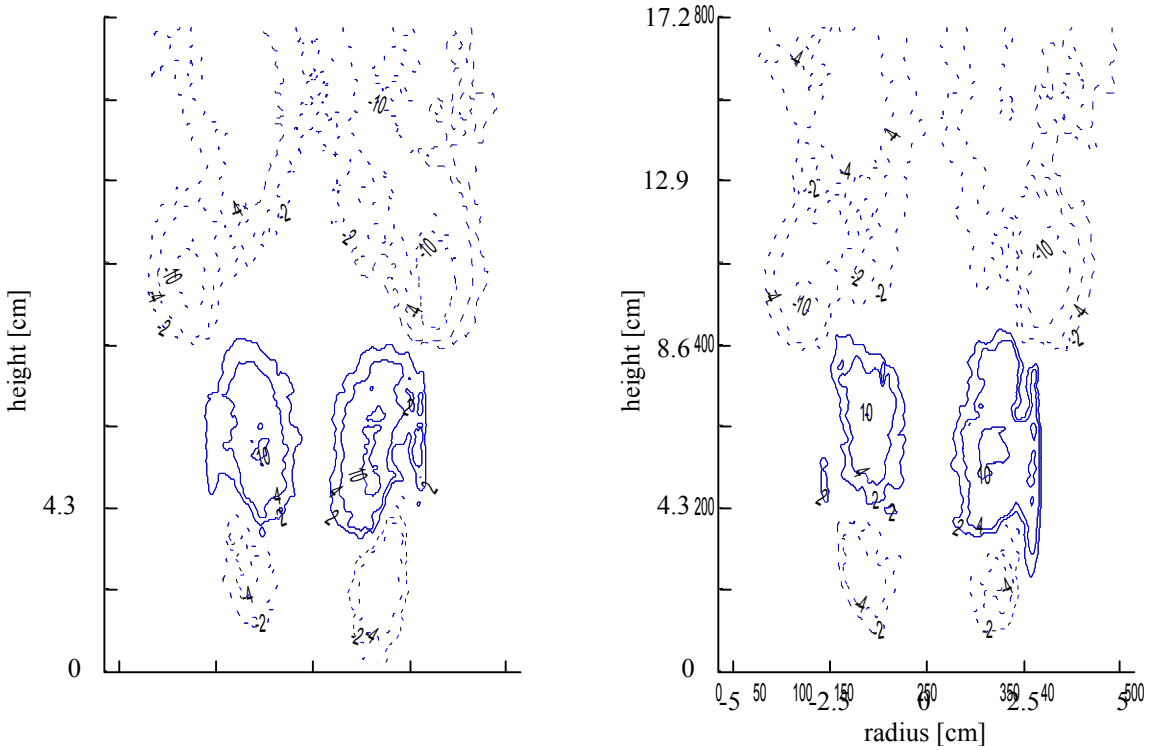

Figure 5-22: Contour plot of R_f for (a) aerodynamically and (b) bluff-body stabilized burners at a driving frequency of 37 Hz.

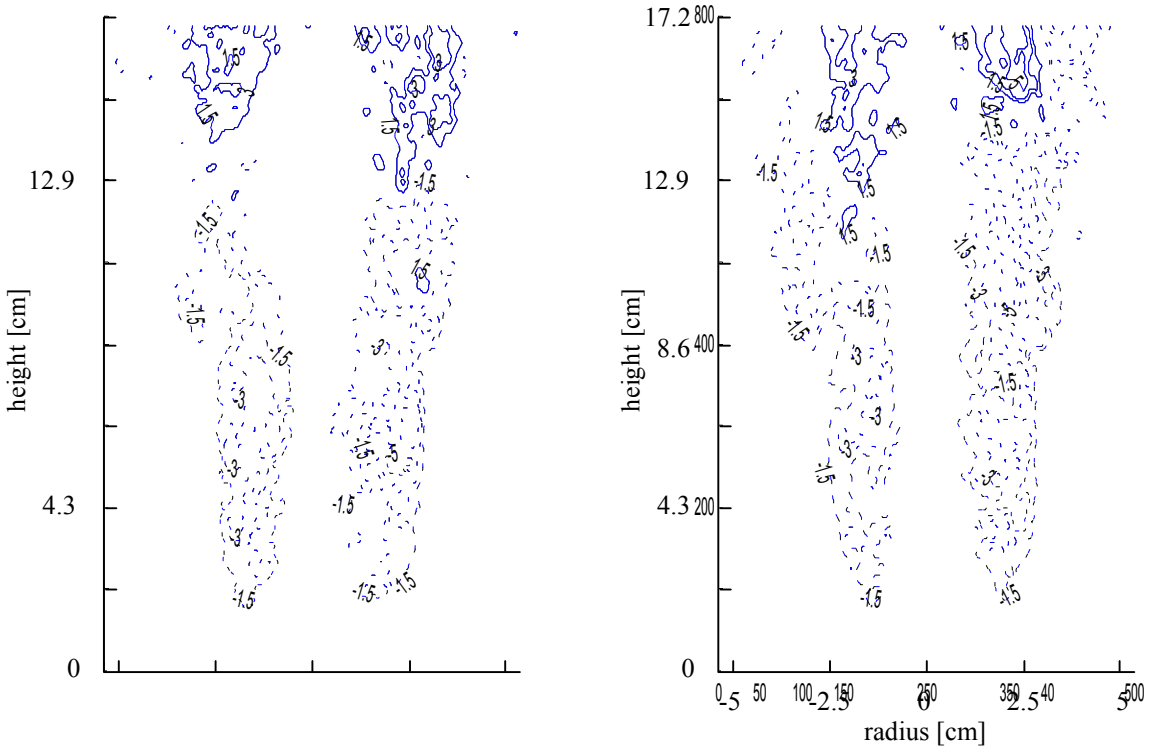

Figure 5-23: Contour plot of R_f for (a) aerodynamically and (b) bluff-body stabilized burners at a driving frequency of 55 Hz.

The contour plots have been replotted into two sets of 2-D color plots (Figure 5-24 and Figure 5-25) of Rayleigh indices, showing only the left side of the flame's dynamical response. This allows for ease of comparison as the driving frequency is changed. As the forcing frequency increases from 22 Hz to 37 Hz, the size of the central "hot zone" (positive local Rayleigh index) decreases and the "cold zone" (negative local Rayleigh index) that appears above it travels down and increases in size. The large drop in the global Rayleigh index (Figure 5-18) at 37 Hz corresponds to the appearance of larger negative regions, particular in the central core of the flame. Other trends are similarly observed between the global and 2-D Rayleigh indices. Although this does not hold at a drive frequency of 55 Hz, comparison of the plots show that the 2-D Rayleigh indices are of very low magnitude throughout the flame. The flame therefore seems to be relatively insensitive to a driving frequency of 55 Hz. These trends are more clearly seen in an axial Rayleigh plot (Figure 5-26), which is obtained by integrating the 2-D plot along the radial direction at each height. This plot indicates that the magnitude of the Rayleigh index is slightly lower for the bluff-body versus aerodynamically stabilized case.

The global Rayleigh index data (Figure 5-18) appears to indicate that the flame should also be insensitive to a drive frequency of 22 Hz – even more so than the 55 Hz case (lower magnitude of R_f). However, comparison of the 22 Hz cases in Figure 5-24 and Figure 5-25 denote that in this situation, correspondingly large negative regions balance regions of large positive Rayleigh index. This point emphasizes the importance of spatially resolved data of Rayleigh's index. It is conceivable that a local flame region responding in phase to a pressure fluctuation could drive an instability due to nonlinear

and geometric effects, if it were situated at an especially critical region (i.e., the ¼ point in a Rijke tube), even if the global Rayleigh index indicated a stable state. Local regions with $R_f > 0$ can also be identified and modified at the design stage, to improve the stability margins of combustion systems.

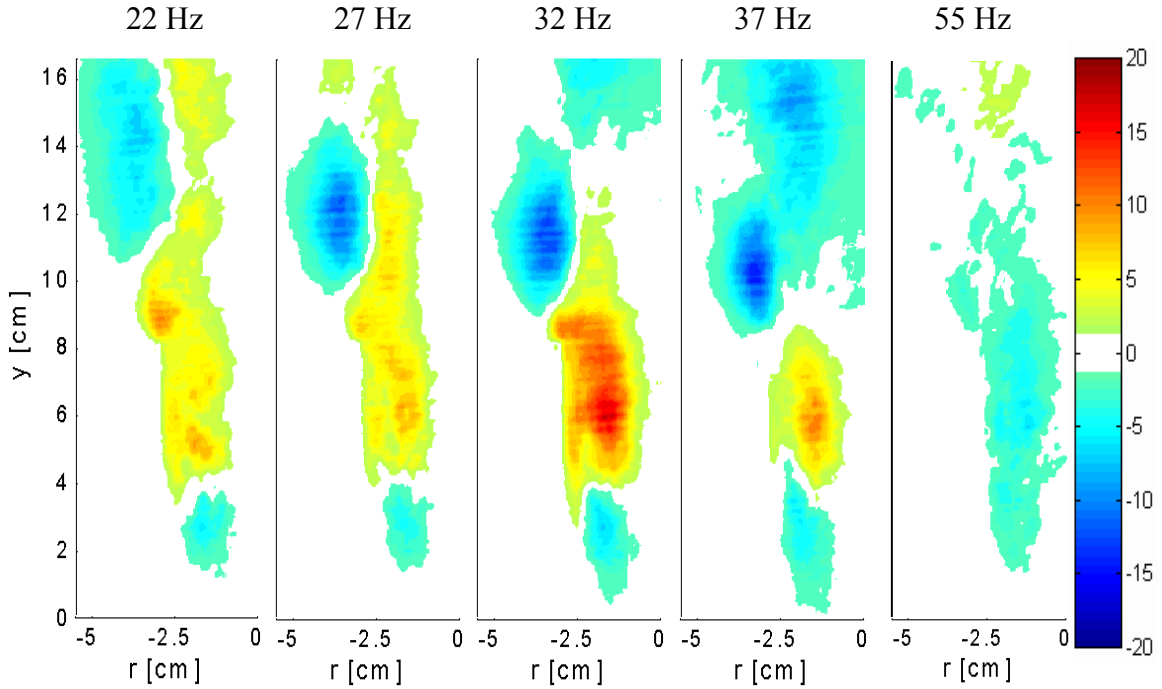

Figure 5-24: Aerodynamically stabilized 2-D Rayleigh plots.

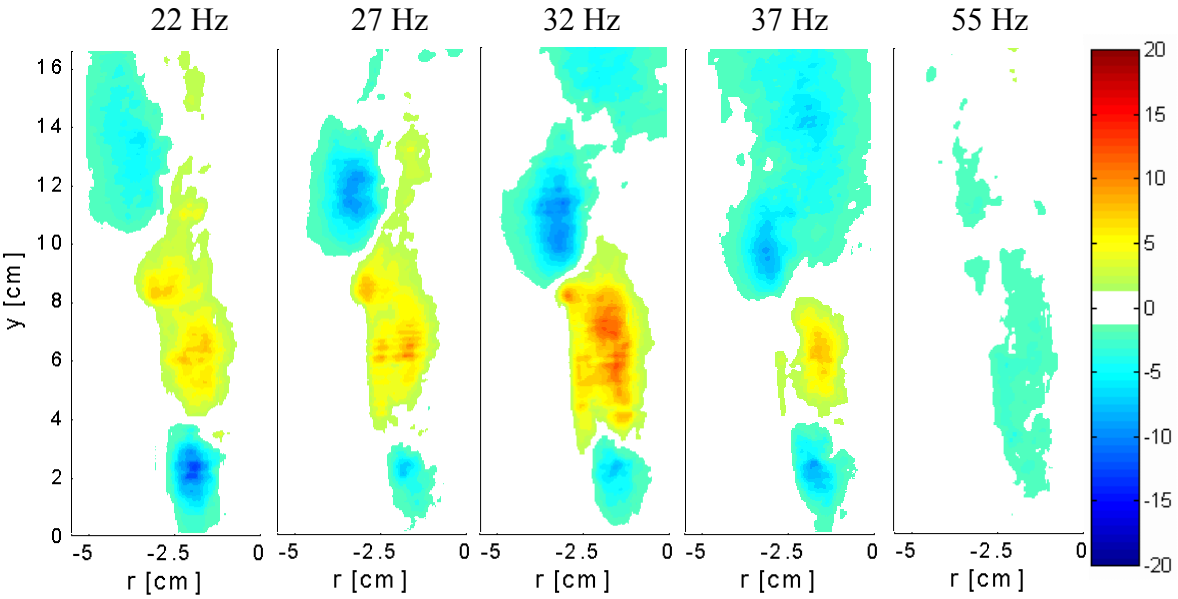

Figure 5-25: Bluff-body stabilized 2-D Rayleigh plots.

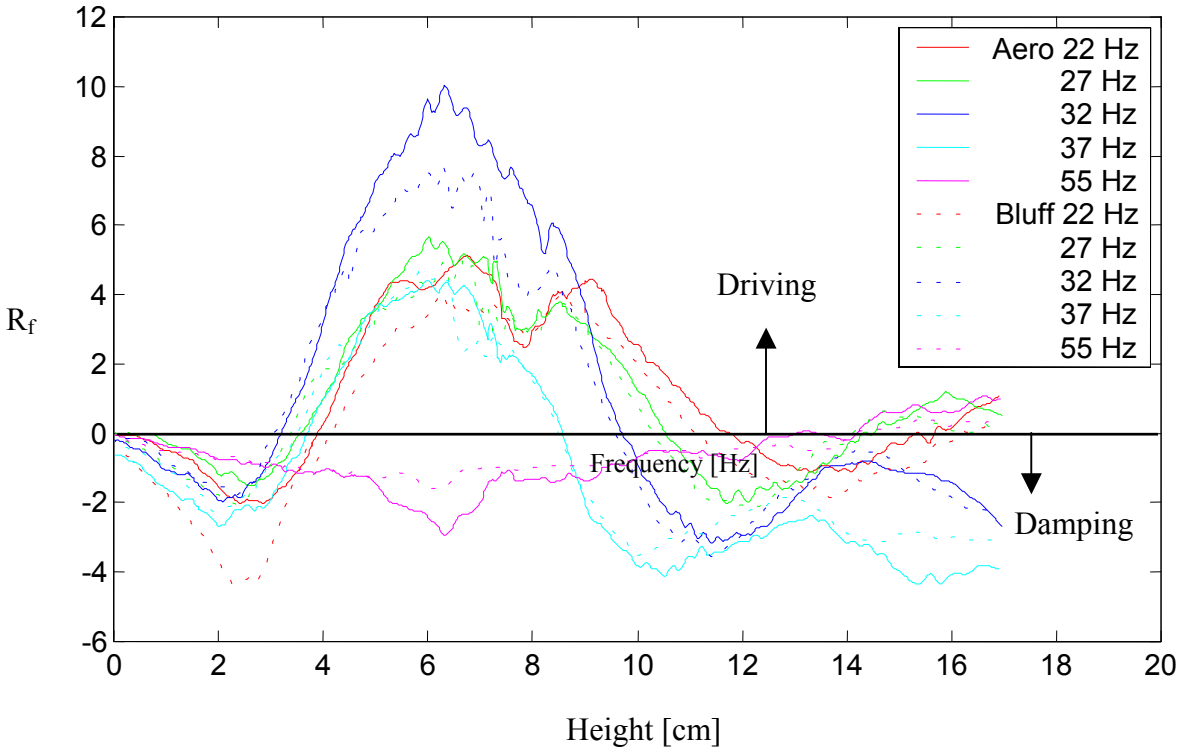

Figure 5-26: Axial Rayleigh index plot: Solid lines are the aerodynamically stabilized burner, and dashed lines are the bluff-body stabilized case.

5.4.5 Combustion Response

The concept of a response function is well known in solid propellant combustion as a modeling tool to quantify the coupling between the pressure and the burning rate. For solid propellants, it is typically formulated as $(m'/\overline{m})/(p'/\overline{p})$, where m represents the mass flux, $(\ )'$ represents fluctuation quantities, and $(\sim)$ denotes time-averaged quantities (Culick, 1968). In this work, it is possible to measure a similar combustion response

function directly, which can be used to close the loop between combustor dynamics and combustion dynamics (Figure 1-2). The combustion response function is defined as

(5-6)
$$C_R = \frac{\left(q'_{rms} / \bar{q}\right)}{\left(p'_{rms} / \bar{p}\right)}$$

In general, C_R will be a complex quantity, since there is a phase difference between the heat release and pressure. Again, this can be evaluated globally or for spatially resolved regions, similar to the Rayleigh index, through judicious use of normalization values.

The global combustion response for both sets of burners is plotted in Figure 5-27. The phase of the heat release has been defined such that it lags the pressure wave. The form

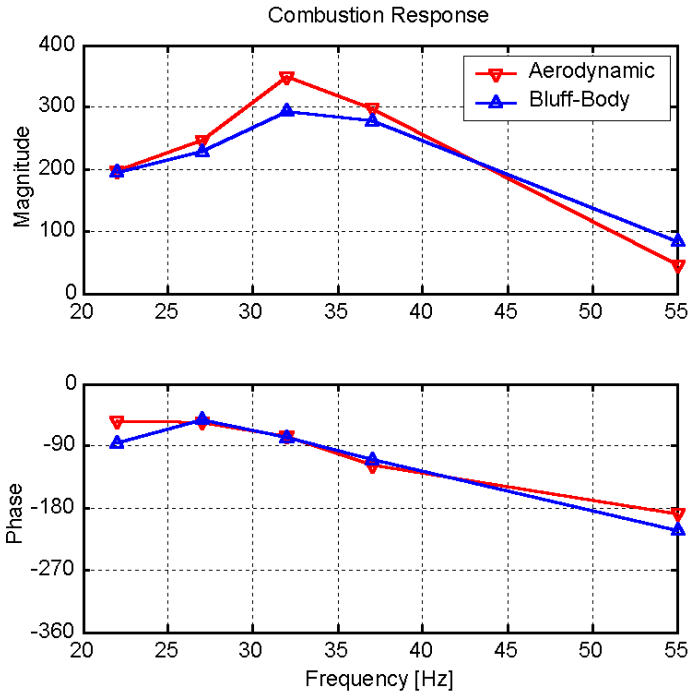

Figure 5-27: Global combustion response function.

of the global combustion response function is similar to the classic quasi-steady response function used in solid propellants (Isella, 2001), containing a single resonant peak. A simple scaling analysis of the magnitude of the fluctuations shows that for pressure amplitudes on the order of $p' \sim 0.005$ psi (Figure 5-7 through Figure 5-16) with a combustion response magnitude of 200, the heat release fluctuation is approximately 7% of the mean heat release rate.

The local combustion response is plotted in Figure 5-28 and Figure 5-29, displaying the magnitude and phase respectively. The magnitude plot (Figure 5-28) has been normalized using the spatial mean of the heat release rate, as opposed to a temporal mean. This is discussed further in Appendix D, where the alternate method is also displayed. The plots are generated by performing an FFT in time for each spatial location, extracting the fluctuating heat release and phase, and constructing the response function.

The spatially resolved plots of magnitude show, in general, that the bluff-body stabilized flame has a weaker response than the aerodynamically stabilized flame, which corresponds to the global result (Figure 5-27). The phase plots (Figure 5-29) show regions where the heat release is in phase (0° to –90° dark red, -270° to –360°dark blue) and out of phase (-90° to -270° orange to light blue).

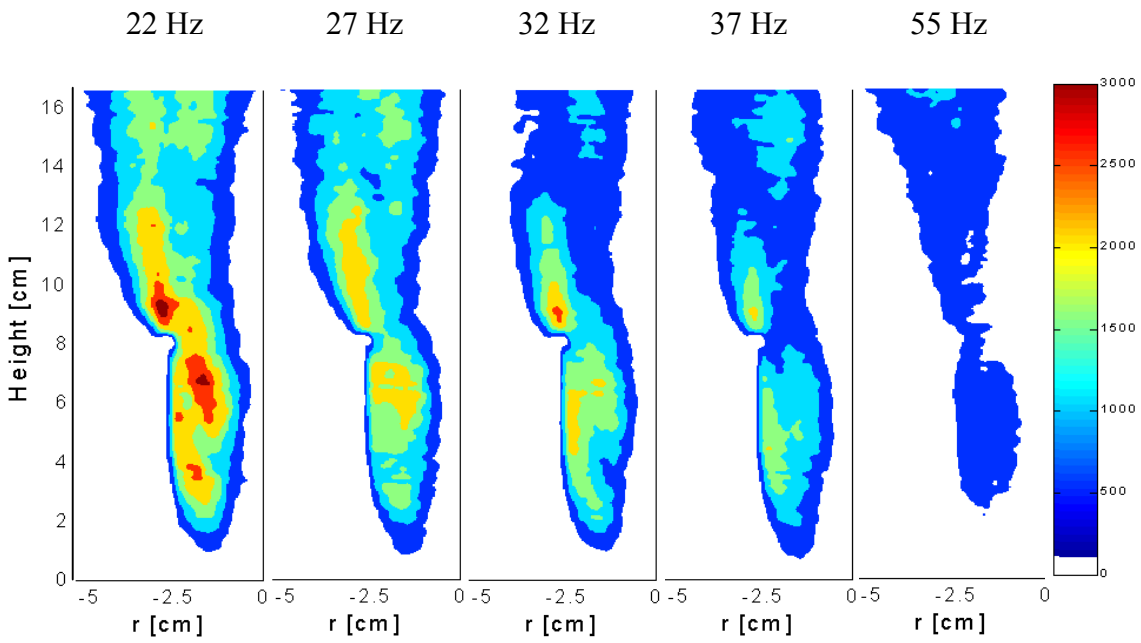

(a)

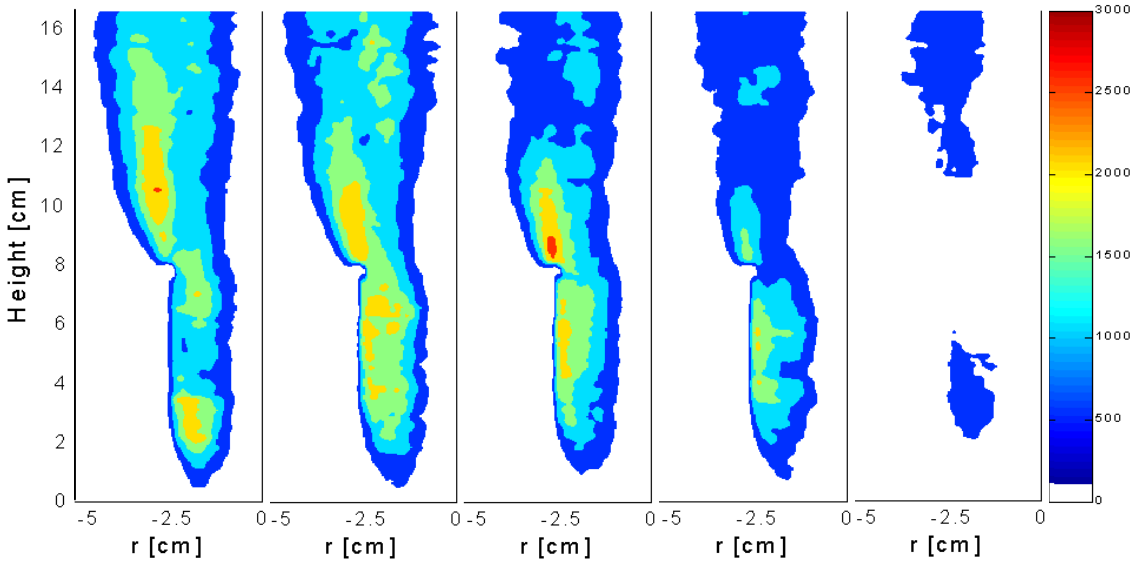

(b)

Figure 5-28: Combustion response – magnitude (a) aerodynamically stabilized (b) bluff-body stabilized.

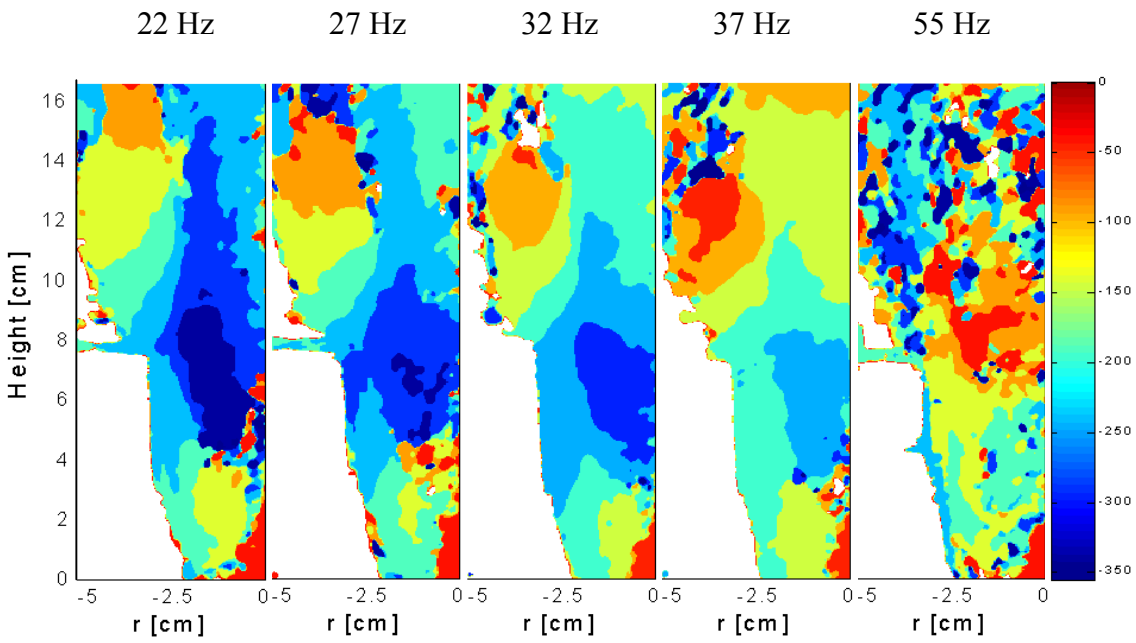

(a)

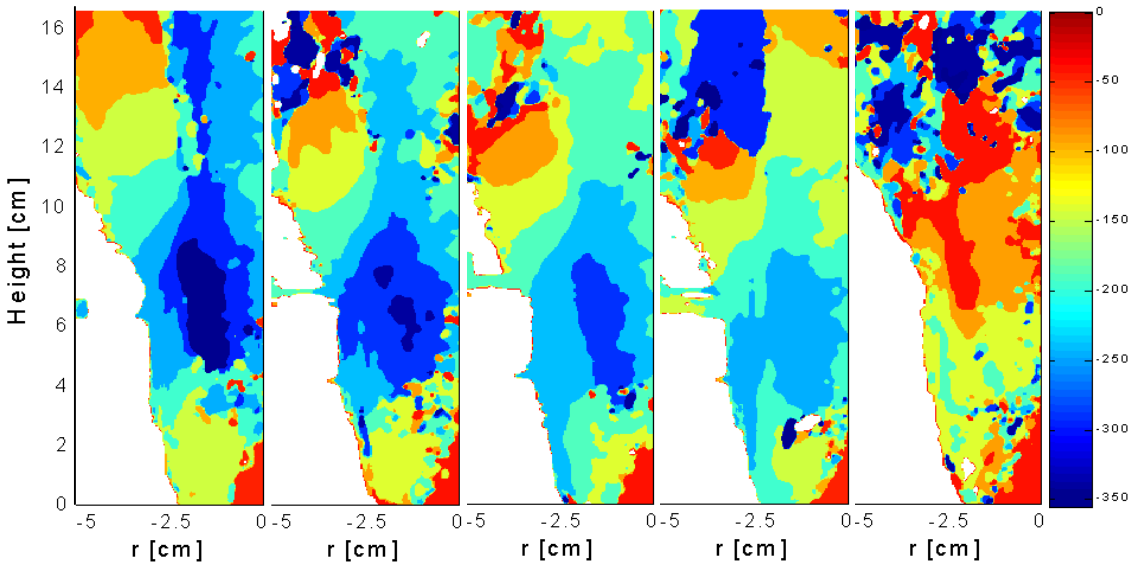

(b)

Figure 5-29: Combustion response – phase (a) aerodynamically stabilized (b) bluff-body stabilized.

The additional information provided by the combustion response function can be used in conjunction with the Rayleigh index to understand what is occurring in the flame during driving or damping. Examining first the global plots, at 22 Hz the global Rayleigh index (Figure 5-18) shows the bluff-body (first mode)[3] to be considerably less driven than the aerodynamic counterpart. The global combustion response at 22 Hz (Figure 5-27) shows that while the magnitude of the response is similar, the heat release of the aerodynamically stabilized burner is more in phase with the pressure oscillation than the bluff-body burner. At 27 and 32 Hz, the phase relationship between the burners is nearly identical, while the bluff-body has a weaker response to acoustic driving, and thus lower Rayleigh indices. At 37 Hz, the aerodynamic burner has a lower Rayleigh index than the bluff-body burner. While the magnitude of the response is lower for the bluff-body, it is also slightly more in phase with the pressure, thus a higher Rayleigh index. This demonstrates the high sensitivity of the system to slight variations in phase. Finally at 55 Hz, the magnitude of the combustion response has dropped very low, such that there is very little driving or damping, and the Rayleigh index drops close to zero.

A similar discussion will apply to the spatially resolved plots of Rayleigh index (Figure 5-24 and Figure 5-25) and combustion response (Figure 5-28 and Figure 5-29). Considering primarily the phase plots, they generally display an anchoring region centered at a height of 2 cm, followed by a strong driving section at the top of the burner tube, and another damped region at the exit of the tube. The 55 Hz case shows extremely

[3] For comparative purposes, the filtered first mode Rayleigh index is always used.

weak driving in the combustion response magnitude, as well as very few coherent structures in phase.

5.5 Summary

A novel system is presented which is capable of measuring the combustion dynamics of a flame under forced oscillatory conditions. The diagnostic used in this chapter is OH PLIF, which provides temporally and spatially resolved measurements, and makes use of the periodic forcing of the flame. The technique presented in this work can potentially be used to directly measure the response of any optically accessible combustion system to an acoustic field. It has been applied to a jet-mixed burner in two configurations: an aerodynamically stabilized and a bluff-body stabilized design. Results are presented in the form of spatially resolved and global Rayleigh indices, as well as global and spatially resolved combustion response functions of the burner. The importance of spatially resolved data manifests itself in the development of more stable designs, as well as improving predictive modeling capabilities. A database of spatially and temporally resolved data on instabilities is important to verify work done in numerical simulations

The 2-D contour and axially integrated plots of Rayleigh's index indicate that the dependence on frequency has a stronger impact on the dynamic response of the flame versus burner configurations tested. Though geometric differences between the burners are slight, the bluff-body design appears to be superior in terms of insensitivity to an imposed acoustic field. The most dramatic difference between the two burner designs occurs at the lowest frequency, 22 Hz, as illustrated in the global change in Rayleigh

index (Figure 5-18). The experimentally derived combustion response function indicates that in the 22 Hz case, the change in Rayleigh index is due to primarily to a shift in phase characteristics between the two burners. The Rayleigh index and combustion response can be used in conjunction, to better understand the dynamics of the flame and acoustic interaction.

These results agree with work by Chen et al. (1998), which demonstrate improved general flame stability (i.e. flame anchoring, but not necessarily improvements with respect to combustion instabilities) with the use of a bluff-body. A more direct comparison can be made to the work of Kendrick et al. (1999), where a bluff-body stabilized system is shown to be superior at resisting the tendency to produce acoustic oscillations than an aerodynamically stabilized system. This does not necessarily indicate a configuration less prone to combustion instabilities since the aerodynamically stabilized burner has a lower Rayleigh index at a drive frequency of 37 Hz using OH PLIF diagnostics. Furthermore, assessment of the tendency for instabilities to appear must be based on analysis of the complete system, comprising the combustion dynamics and the dynamics of the combustor.

Chapter 6
Concluding Remarks

This work provides experimental measurements of a variety of devices involving thermo-acoustic interactions pertaining to the general problem of combustion instabilities. We begin with an electrically driven Rijke tube, perhaps the simplest demonstration of heat-induced pressure oscillations, continue on to a large scale industrial flare, and conclude with detailed measurements of the combustion dynamics of two burners under forced oscillatory conditions.

Measurements from the Rijke tube indicate the presence of hysteresis with respect to the power input at high mass flow rates (over 3 g/s in this configuration). As the heater input power is increased until the Rijke tube exhibits instability, when the power is reversed, significantly less power continues to sustain the oscillation. A detailed stability map with uncertainty of the stability boundary over a range of mass flow rates and heater power

levels is provided, at a heater location of x/L = ¼. A precise definition of instability is introduced combining both pressure amplitudes and frequencies of decomposed modes, which allows for better determination of system instability in possibly ambiguous situations. A one-dimensional linear stability model is offered that accounts for variations of heat release and associated time delays by incorporating numerical simulations from Kwon and Lee (1985). This model is based entirely on physical properties of the experiment and uses no empirical fits. The model qualitatively reproduces the instability curve, but is unable to accurately match the stability boundary over a wide range of mass flow rates, nor provide an explanation for hysteresis.

Data collected on the industrial flare emphasized the nonorthogonality of the acoustic modes, with the quarter-wave mode occurring at 8.3 Hz, and the three-quarter-wave mode located at 21.5 Hz. Sub-scale modeling efforts brought forth difficulties in scaling unstable frequencies, since the acoustic losses scale with frequency.

A novel technique was demonstrated which can measure the combustion dynamics of a flame in an acoustically excited environment. Measurements of the combustion dynamics of two versions (aerodynamically and bluff-body stabilized) of a partially premixed jet burner were taken using two different techniques. Chemiluminescence measurements offered greater convenience since a laser source is not required, while OH PLIF measurements have finer spatial and temporal resolution. The method employed in this work is useful in the design and prediction of how a particular burner will respond in a real combustor environment.

Chemiluminescence measurements also provide insight into the flow visualization of burners. The evolution of the flame and flame base mean location and oscillation amplitude were observed at each of the forcing conditions over an entire cycle. Forcing at 55 Hz was virtually transparent to both burner configurations, and is considered to be a different regime of operation. At frequencies below 37 Hz, the flame base position decreased with the bluff-body stabilized burner when compared with the aerodynamically stabilized system. At 37 Hz the opposite effect occurred.

Forced Rayleigh indices were computed using two techniques: heat release derived from OH PLIF measurements, and heat release inferred from flame chemiluminescence. Examination of 2-D spatially resolved R_f contour plots using OH PLIF (Figure 5-19 to Figure 5-23) and the same plots computed using chemiluminescence (Figure C-6 to Figure C-10), shows fairly consistent discrepancies due primarily to the line-of-sight integration occurring with chemiluminescence. Most obvious is the hollow core in the OH measurements, since the flame is not burning in the core region of the burner. There are also differences in the relative sizes of the flame damping and driving zones.

Starting at the base of the flame, the OH results show a much smaller damped zone than the chemiluminescence results. Axial plots show qualitative agreement in the general shape of the response for both techniques, however the relative magnitudes differed in various zones. Global Rayleigh indices for the first mode of pressure filtered show the bluff-body burner superior in all cases in resisting oscillations in all cases except at 37

Hz. The opposite result is obtained for chemiluminescence global Rayleigh indices. Part of this discrepancy is attributable to the fact that the chemiluminescence imaging technique integrates across the flame. Another factor is the contribution of other chemiluminescent species that do not indicate zones of heat release, such as CO_2. The OH PLIF Rayleigh results agree with the chemiluminescent flow visualization of the flame base; a lower flame base corresponds to a stiffer flame, which is more able to resist coupling with the acoustic waves.

The combustion response of the flame is also computed, based on the OH PLIF measurements. It is useful in conjunction with the Rayleigh index in explaining the combustion dynamics of the flame. The high sensitivity of the Rayleigh index to the phase of the combustion response is demonstrated, particularly for the 37 Hz case. These measurements of the combustion dynamics of a flame are the first of its kind.

Directions for Future Work

The Rijke tube experiment offers an ideal test bed to develop theoretical models to predict limit cycle amplitudes and stability boundaries. The experimental configuration is easily modified to produce stability maps at other heater locations of interest, such as x/L = 1/8, which, according to Rayleigh's criteria, should preferentially drive the 2nd mode of the system. In order to accurately model the response of the Rijke tube, more detailed models of heat release from the grid and gas dynamics will be required. Prediction of limit cycle amplitudes will also require additional modeling of nonlinear

processes. Nonorthogonality of the modes should be addressed, as temperature profiles indicate a complex temperature distribution as the flow develops.

Although chemiluminescence does not provide accurate Rayleigh indices in this work, it should be investigated further, using OH PLIF as a means to evaluate its accuracy. Possible improvements would be to use a bandpass filter to eliminate sources of chemiluminescence that do not indicate heat release. The sensitivity of the camera must also be increased if this is done, possibly by addition of an intensifier. Other species of interest can also be probed using PLIF techniques, such as CH and NO. Zones of NO_x production under an acoustic field can be identified and possibly minimized in future burner designs to aid in the development of ultra low emissions engine systems.

Since a framework has been established for measuring combustion dynamics, a variety of other burner designs can be evaluated. A simple burner, easily modeled would be useful in verifying results from numerical and theoretical models. Additional improvements would entail improvement of the test section, such as the use of flat windows to improve optical access. The addition of other diagnostics such as PIV will improve visualization of the flow field, more precisely mapping vorticity production and velocity responses to the acoustic field.

Appendix A
Mechanical Drawings

Scale: 1" = 5"

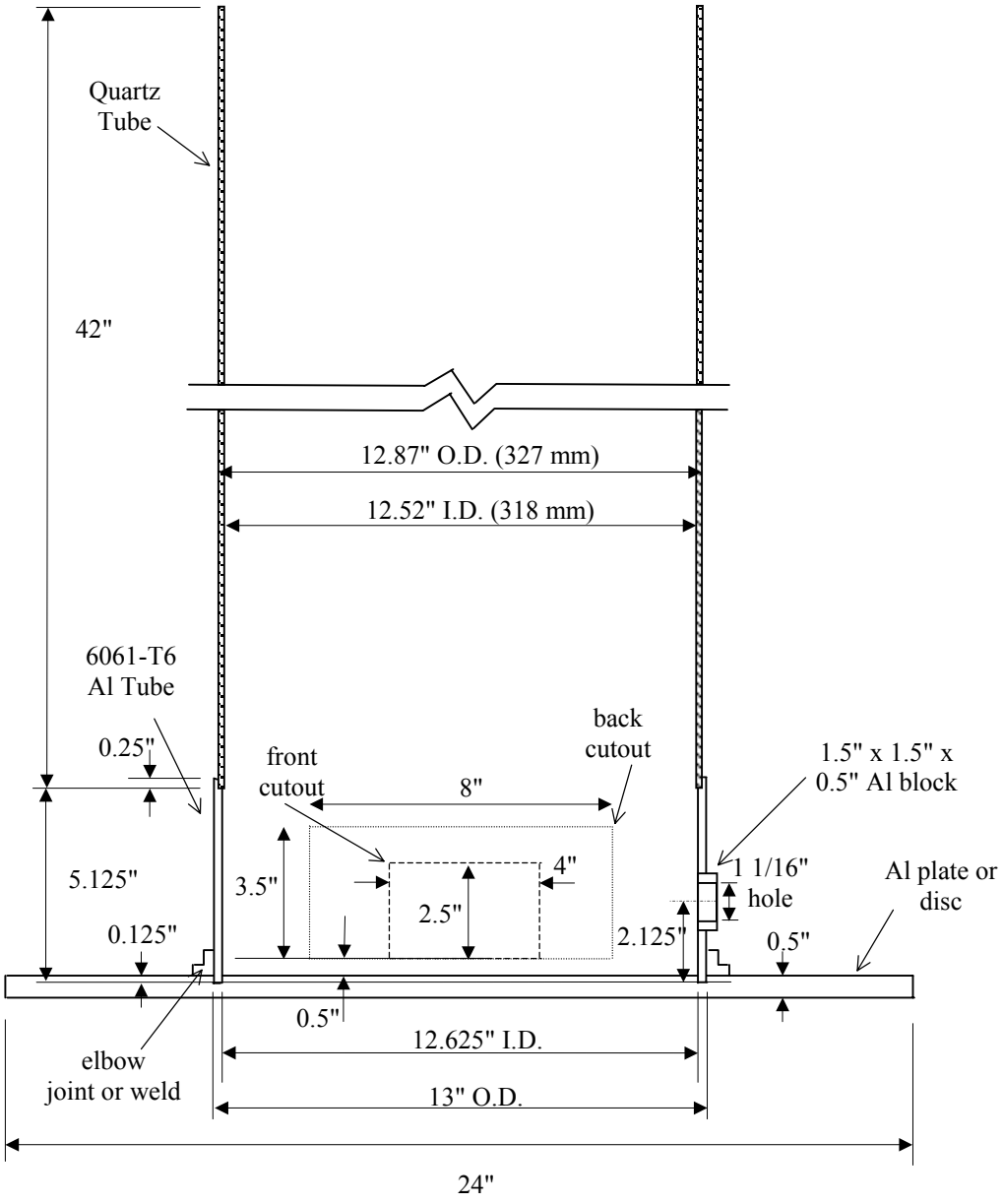

NOTES:

1. Al block is welded to the Al tube, after an appropriately sized hole is cut, to allow a ¾" bulkhead fitting centered in the block.
2. Burner, plumbing, holes in quartz tube, and bulkhead fitting are not shown.
3. A cover for the holes should be constructed, which consists of a rolled sheet to match the Al tube, with cutouts matching those on the tube. Appropriate slots (elbow joints, bulkhead) should also be cut, to allow the cover to rotate around the tube on the platform, from a fully open to a fully closed position. It is preferable if both slots can be covered independently, but not required.

Figure A-1: 1/12th scale flare model: chamber section.

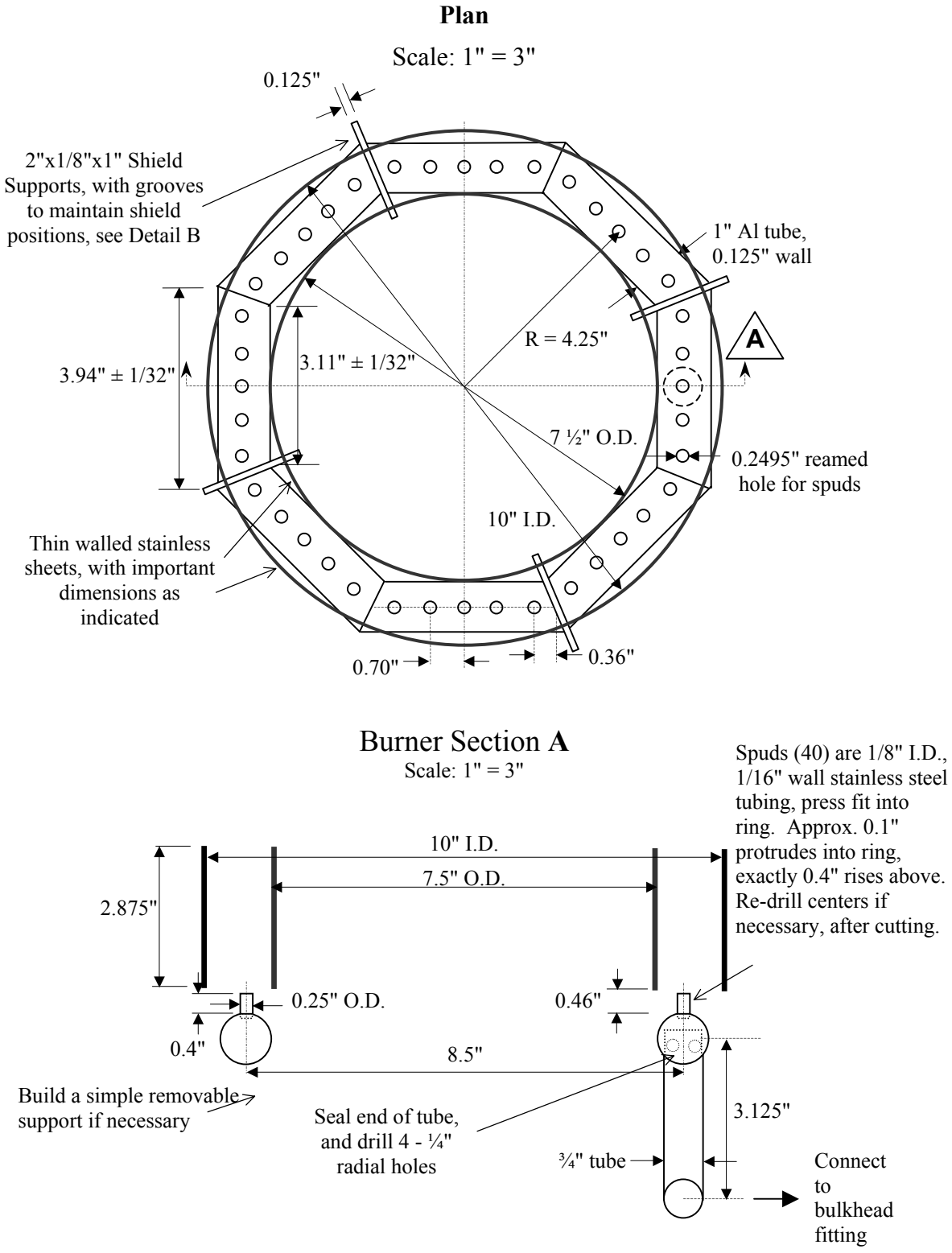

Figure A-2: 1/12th scale flare model: burner section.

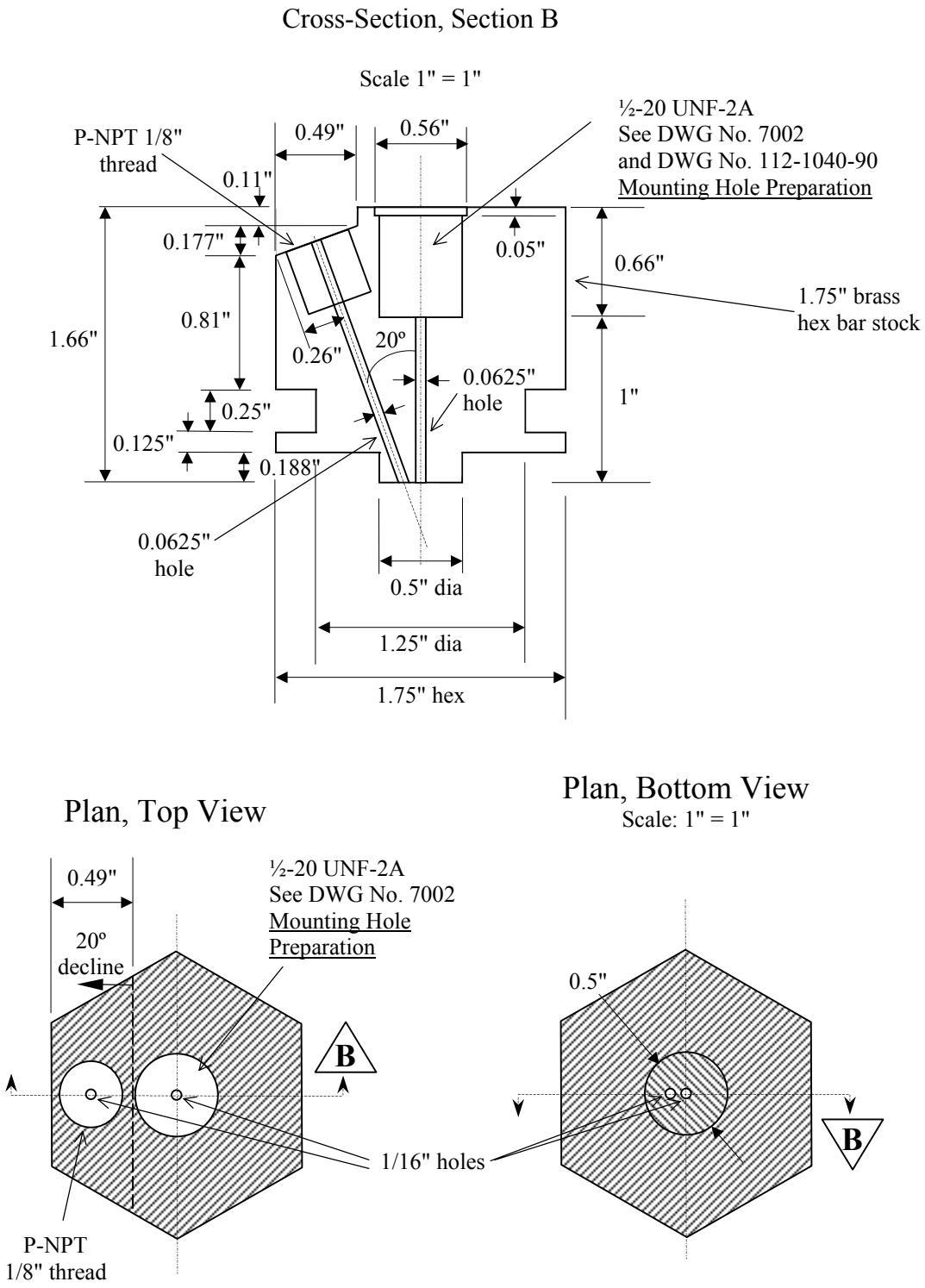

Figure A-3: Instrumentation boss.

Appendix B
Gas Mixture Viscosity Calculation

For a gas mixture, the mixture viscosity can be calculated using the following equation (Kanury, 1975):

(B-1)
$$\mu_{mixture} = \sum_{i=1}^{n} \frac{\chi_i \mu_i}{\sum_{j=1}^{n} \chi_j \phi_{ij}},$$

where

$$\phi_{ij} = \frac{1}{\sqrt{8}} \left(1 + \frac{M_i}{M_j}\right)^{-1/2} \left[1 + \left(\frac{\mu_i}{\mu_j}\right)^{1/2} \left(\frac{M_j}{M_i}\right)^{1/4}\right]^2$$

and χ_i is the mole fraction of species i, M_i is the molecular weight of species i, μ_i is the viscosity of species i, and n is the total number of species.

In the experiments measuring combustion dynamics, a binary gas mixture is used. The mixture viscosity is important since the flow is premixed and measured using a single laminar flow element. A quadratic fit for the viscosity of several gases, valid from 5 °C – 45 °C is performed, such that

(B-2)
$$\mu_i = a_2 T^2 + a_1 T + a_0,$$

where μ_i is the viscosity of species i in micropoise (1 gm/cm/sec = 10^6 micropoise) and T is in °C. The constants a_2, a_1, and a_0 are given in Table B-1.

Species	a_2	a_1	a_0
CH_4	-0.005	0.710	96.499
CO_2	-0.010	1.060	130.500
N_2	-0.010	1.100	160.000

Table B-1: Coefficients for viscosity quadratic fit, valid for P = 1 atm, 5 °C < T < 45 °C.

Appendix C
Chemiluminescence Rayleigh Indices

This appendix contains the spatially resolved chemiluminescent forced Rayleigh indices. Figure C-1 to Figure C-5 show the axial profiles, with the aerodynamic and bluff-body burners plotted together. The axial profiles are obtained by integrating the averaged 2-D flame contours at each height and phase, and multiplying with the bulk averaged and filtered (about the driving mode) pressure. The 2-D plots (Figure C-6 to Figure: C-10) are obtained by direct evaluation of Rayleigh's criterion with the averaged 2-D contours.

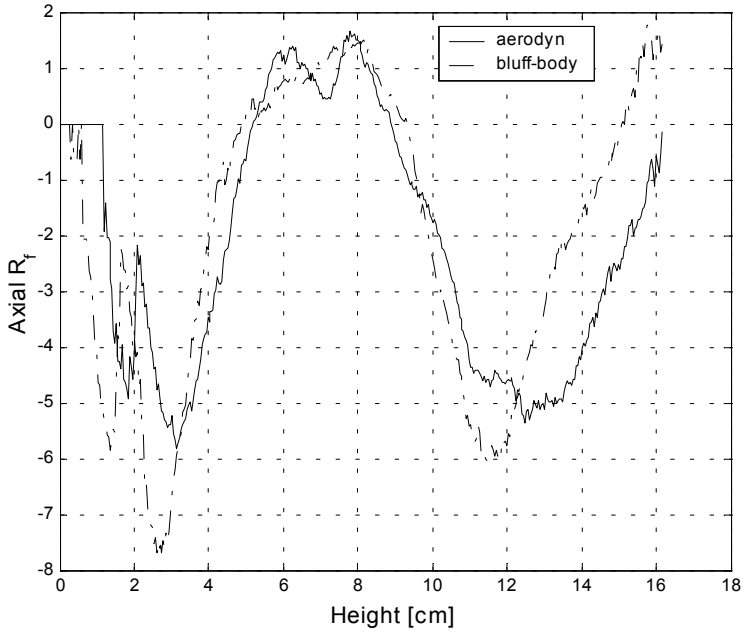

Figure C-1: Chemiluminescence axial forced Rayleigh indices at 22 Hz.

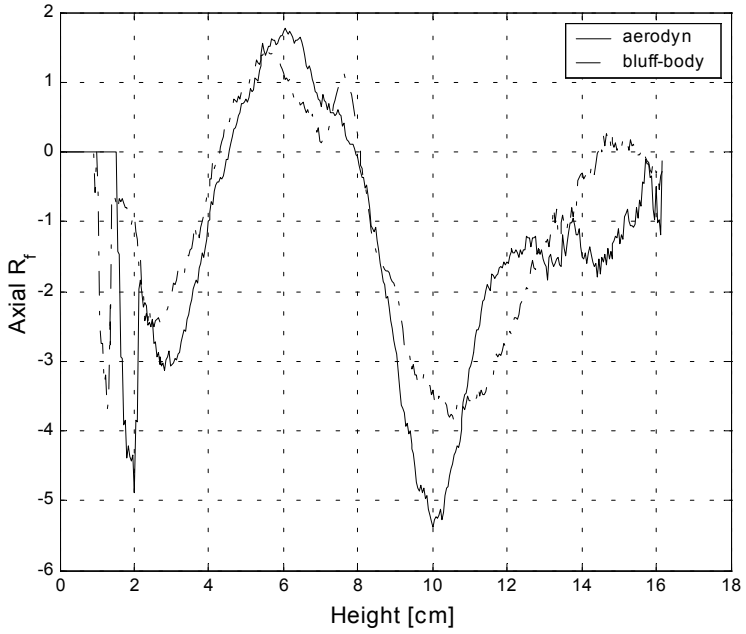

Figure C-2: Chemiluminescence axial forced Rayleigh indices at 27 Hz.

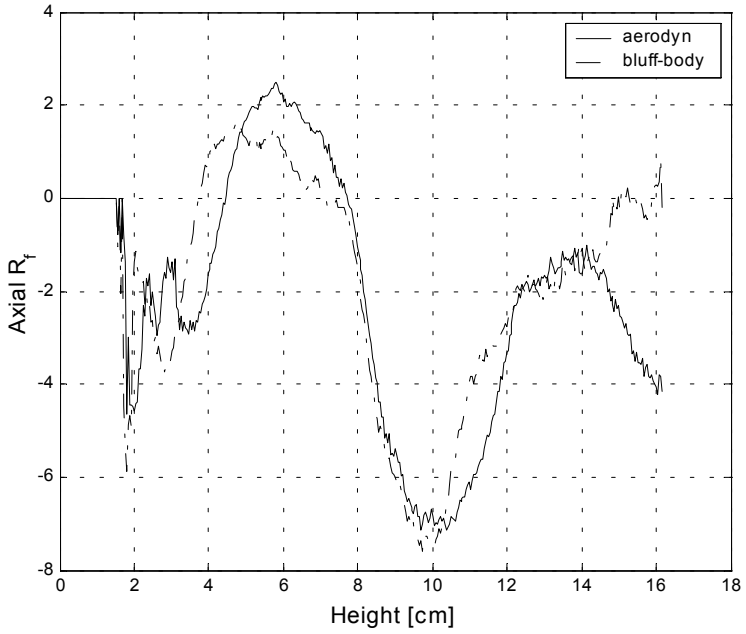

Figure C-3: Chemiluminescence axial forced Rayleigh indices at 32 Hz.

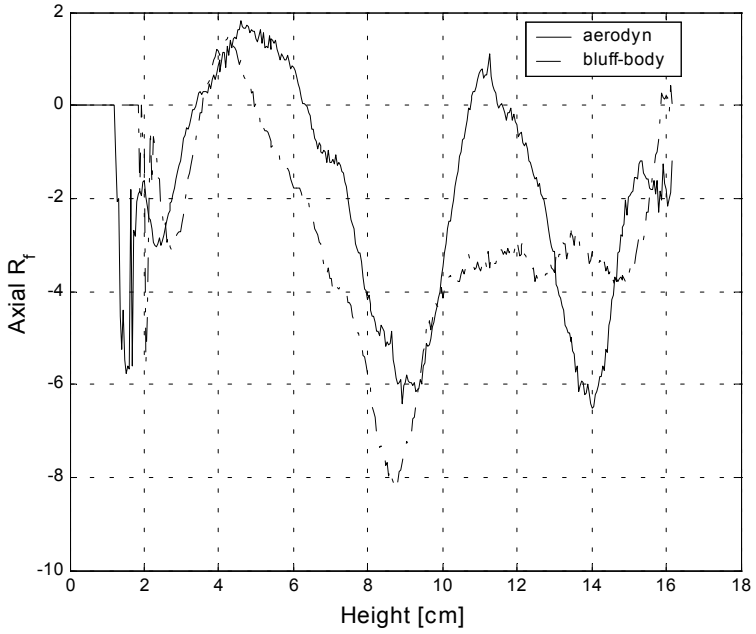

Figure C-4: Chemiluminescence axial forced Rayleigh indices at 37 Hz.

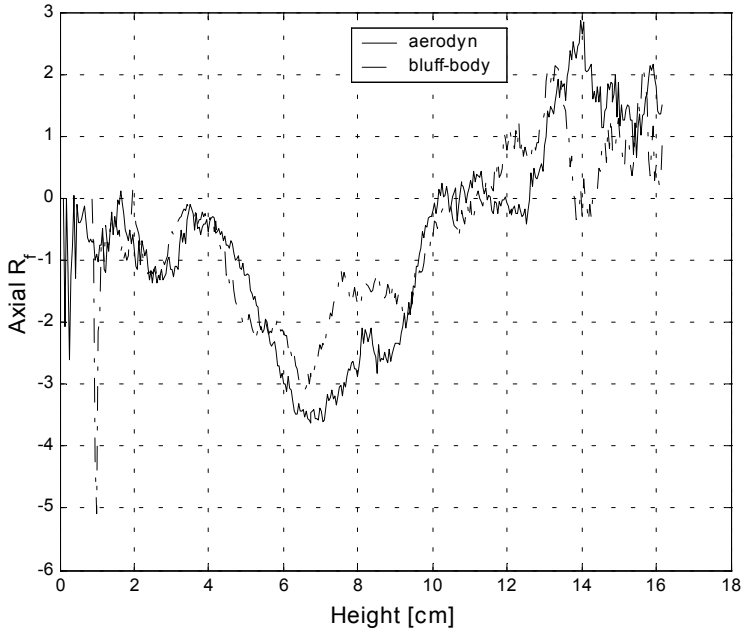

Figure C-5: Chemiluminescence axial forced Rayleigh indices at 55 Hz.

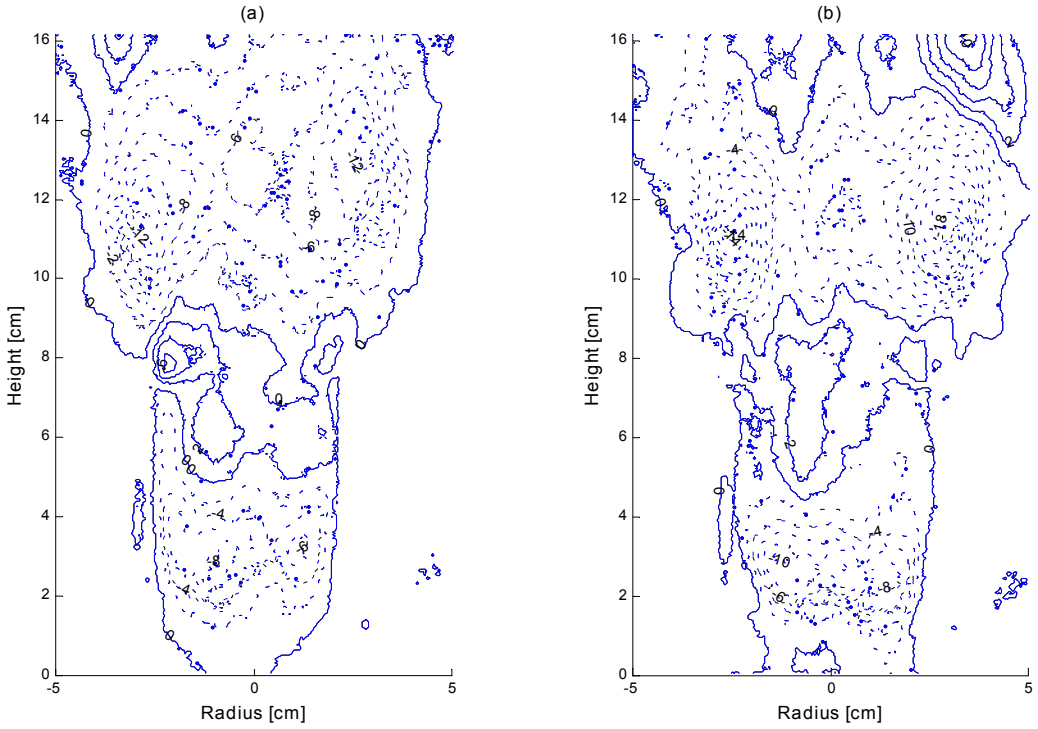

Figure C-6: Chemiluminescence 2-D forced Rayleigh indices at 22 Hz for (a) aerodynamically and (b) bluff-body stabilized burners.

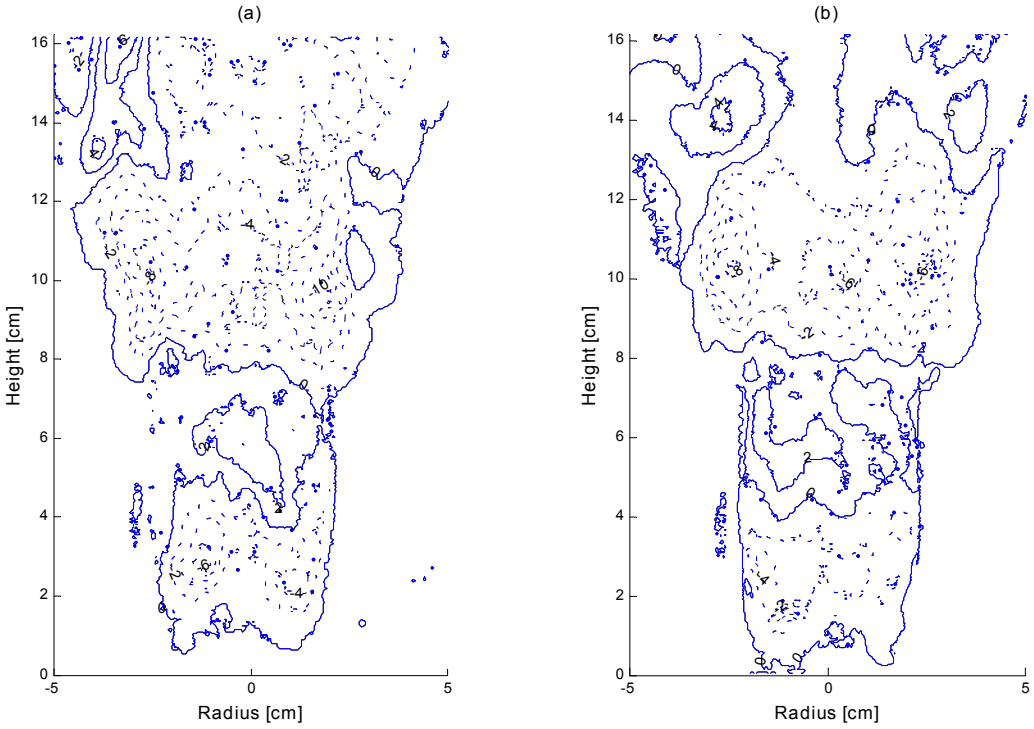

Figure C-7: Chemiluminescence 2-D forced Rayleigh indices at 27Hz for (a) aerodynamically and (b) bluff-body stabilized burners.

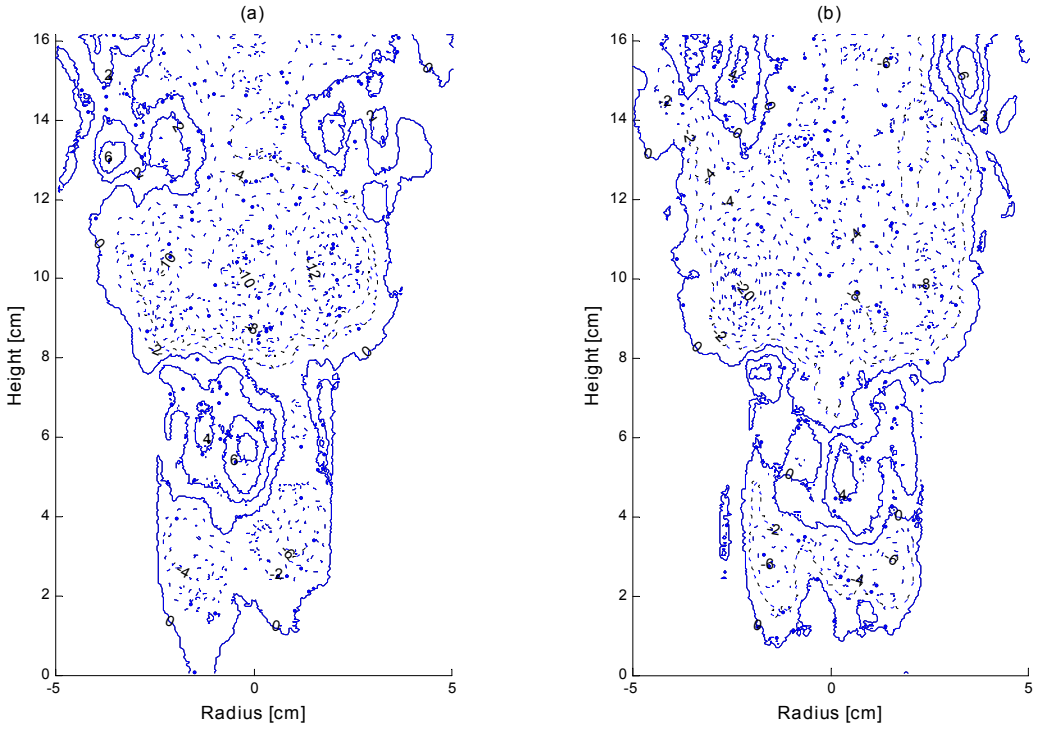

Figure C-8: Chemiluminescence 2-D forced Rayleigh indices at 32Hz for (a) aerodynamically and (b) bluff-body stabilized burners.

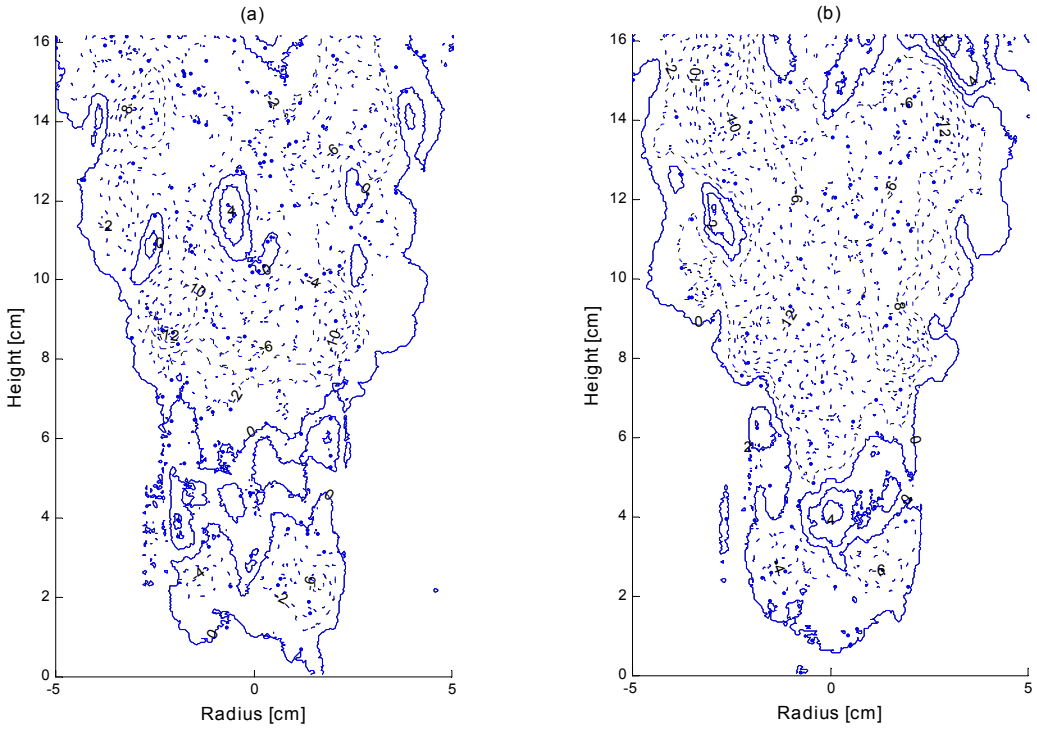

Figure C-9: Chemiluminescence 2-D forced Rayleigh indices at 37 Hz for (a) aerodynamically and (b) bluff-body stabilized burners.

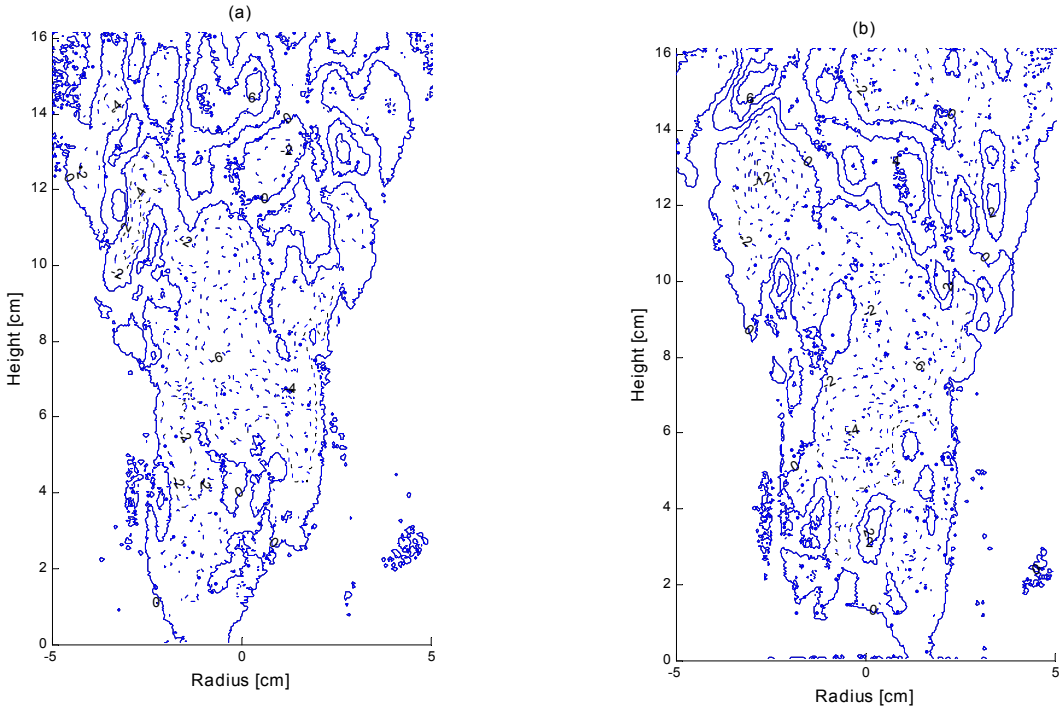

Figure: C-10: Chemiluminescence 2-D forced Rayleigh indices at 55 Hz for (a) aerodynamically and (b) bluff-body stabilized burners.

Appendix D
Locally Normalized Combustion Response

The magnitude of the local combustion response can be plotted in two ways:

- using the a spatial heat release mean, or
- using a local, temporal mean for the heat release.

Section 5.5 uses the former method, as it was found to be more useful, however it was not evident that this would be the case.

The main problem that arises when using the local temporal mean to normalize the heat release is at the edges of the flame. The edges of an oscillating flame are continually fluctuating in space, as well as time. As a result, a particular spatial location near the edge may or may not contain a flame at any particular instant. While the mean heat release rate will be non-zero (compared to a region outside the flame zone), the temporal mean will be very low due to the periods of time when there is no flame present. This causes the $q'/\overline{q}$ term in the combustion response function to be extremely large compared to other interior regions of the flame.

This phenomenon is displayed in Figure D-1, using a log scale for the magnitude. The same process that magnifies the edge of the flame also enhances any inherent noise in the image field. This is seen in Figure D-1 as the “fingers” extending from to the left. Although it was determined that these plots are not practically useful, they are presented here to provide guidance in future works.

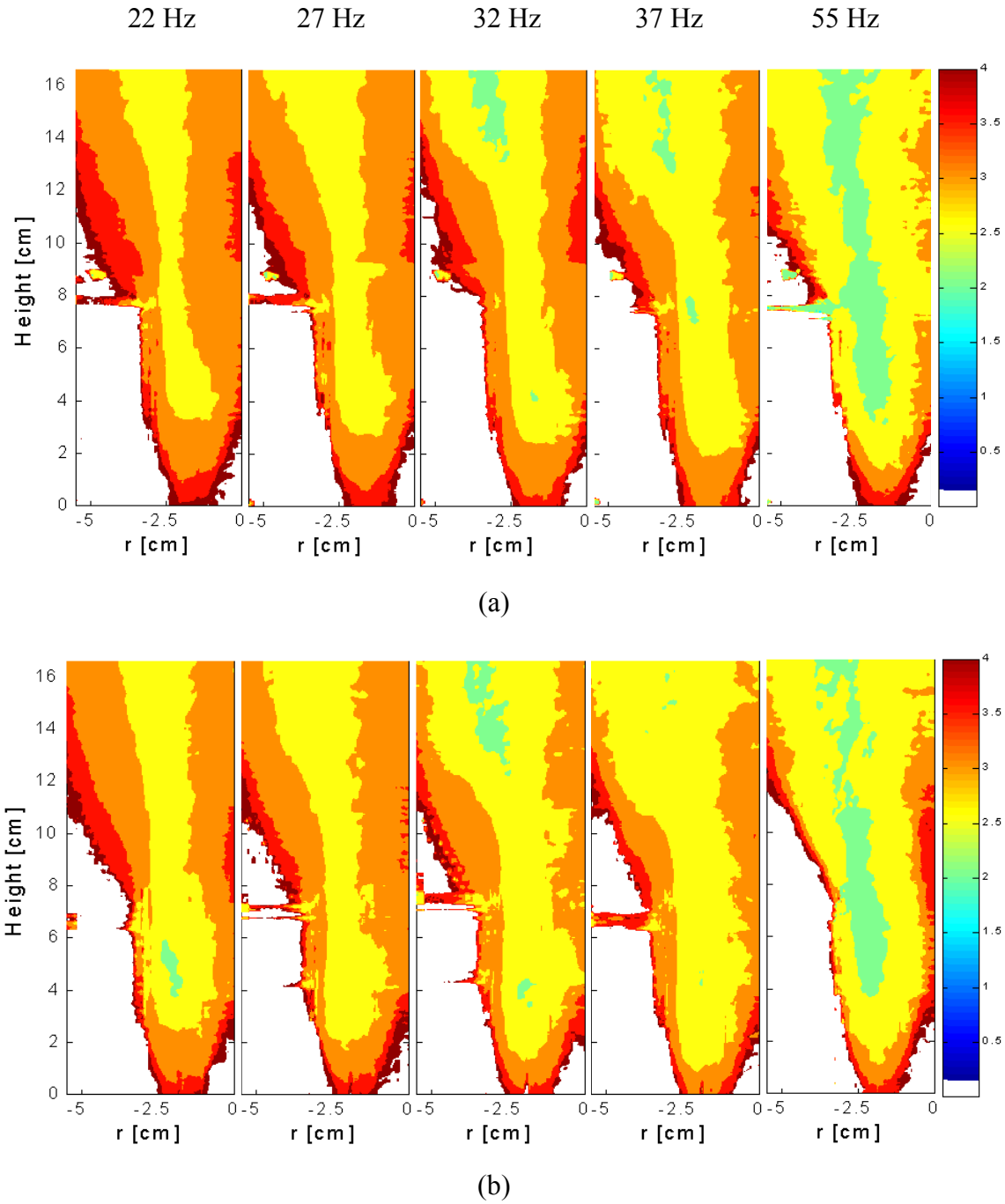

Figure D-1: Locally normalized combustion response – magnitude (intensity is on a log scale) (a) aerodynamically stabilized (b) bluff-body stabilized

References

Allen, M.G., McManus, K.R., Sonnenfroh, D.M., and Paul, P.H., (1995) "Planar laser-induced fluorescence imaging measurements of OH and hydrocarbon fuel fragments in high-pressure spray-flame combustion", Applied Optics, Vol. 34, No. 27.

Allen, M.G., McManus, K.R., and Sonnenfroh, D.M., (1995a) "PLIF Imaging in Spray Flame Combustors at Elevated Temperatures", AIAA Paper 95-0172.

Allen, M.G., Parker, T.E., Reinecke, W.G., Legner, H.H., Foutter, R.R., Rawlins, W.T., and Davis, S.J. (1993) "Fluorescence Imaging of OH and NO in a Model Supersonic Combustor", AIAA Journal, Vol. 31, No. 3.

Anderson, T.J., Kendrick, D.W., and Cohen, J.M. (1998) "Measurement of Spray/Acoustic Coupling in Gas Turbine Fuel Injectors", presented at the 36th Aerospace Sciences Meeting & Exhibit, Reno, NV, AIAA 98-0718.

Barlow, R.S., and Collignon, A., (1991) "Linear LIF Measurements of OH in Nonpremixed Methane-Air Flames: When are Quenching Corrections Unnecessary", AIAA Paper 91-0179.

Barlow, R.S., Dibble, R.W., Chen, J.-Y., and Lucht, R.P. (1990) "Effect of Damkohler Number on Superequilibrium OH Concentration in Turbulent Nonpremixed Jet Flames", Combustion and Flame, Vol. 82, pp. 235-251.

Battles, B.E. and Hanson, R.K. (1995) "Laser-Induced Fluorescence Measurements of NO and OH Mole Fraction in Fuel-Lean, High-Pressure (1-10 atm) Methane Flames: Fluorescence Modeling and Experimental Validation", J. Quant. Spectrosc. Radiat. Transfer, Vol. 54, No. 3, pp. 521-537.

Bjerken, L. (1999) Personal Communication.

Burnley, V.S., and Culick, F.E.C. (2000) "Comment on Triggering of Longitudinal Combustion Instabilities in Rocket Motors: Nonlinear Combustion Response", J. of Prop. Power, Vol. 16, No. 1, pp. 164-166.

Broda, J.C., Seo, S., Santoro, R.J., Shirhattikar, and Yang, V. (1998) "An Experimental Study of Combustion Dynamics of a Premixed Swirl Injector", Twenty-Seventh Symposium (International) on Combustion, The Combustion Institute.

Cadou, C.P. (1996) "Two-Dimensional, Time-Resolved Temperature Measurements in a Resonant Incinerator using Planar Laser-Induced Fluorescence", Ph.D. Thesis, University of California (Los Angeles).

Cadou, C.P., Logan, P., Karagozian, A.R., and Smith, O.I. (1991) "Laser diagnostic techniques in a resonant incinerator", Environ. Sensing Combust. Diagn., SPIE, Vol. 1434, pp. 67-77.

Cadou, C.P., Smith, O.I., and Karagozian, A.R. (1998) “Transport Enhancement in Acoustically Excited Cavity Flows, Part 2: Reactive Flow Diagnostics”, AIAA Journal, Vol. 36, No. 9, pp. 1568-1574.

Cattolica, R. (1981) “OH rotational temperature from two-line laser-excited fluorescence”, Applied Optics, Vol. 20, No. 7, pp. 1156-1166.

Cessou, A. and Stepowski, D. (1996) “Planar Laser Induced Fluorescence Measurement of [OH] in the Stabilization Stage of a Spray Jet Flame”, Combust. Sci. and Tech., Vol. 118, pp. 361-381.

Chen, T.Y., Hegde, U.G., Daniel, B.R., and Zinn, B.T. (1993) “Flame Radiation and Acoustic Intensity Measurements in Acoustically Excited Diffusion Flames”, J. Propul. Power, Vol. 9, No. 2.

Chen, Y.C., Chang, C.C., Pan, K.L., and Yang, J.T. (1998) “Flame Lift-off and Stabilization Mechanisms of Nonpremixed Jet Flames on a Bluff-body Burner”, Combustion and Flame, Vol. 115, pp. 51-65.

Christo, F.C., Fletcher, D.F., and Joseph, S.D. (1998) “Computational fluid dynamics modelling of a landfill gas flare”, Journal of the Institute of Energy, Vol. 71, pp/ 145-151.

Clanet, C., Searby, G., and Clavin, C. (1999) “Primary acoustic instability of flames propagating in tubes: cases of spray and premixed gas combustion”, J. Fluid Mech., vol. 385, pp.157-197.

Collyer, A.A., and Ayres, D.J. (1972) “The generation of sound in a Rijke tube using two heating coils”, *J.Phys.D:Appl.Phys.*, Vol. 5.

Correa, S.M., (1992) “A Review of NOx Formation Under Gas-Turbine Combustion Conditions”, Combust. Sci and Tech., Vol. 87, pp. 329-362.

Culick, F.E.C. (1968) “A Review of Calculations for Unsteady Burning of a Solid Propellant”, AIAA Journal, Vol. 6, No. 12, pp. 2241-2255.

Culick, F.E.C., (1976) “Nonlinear Behavior of Acoustic Waves in Combustion Chambers”, Parts I and II, Acta Astronautica, Vol. 3, pp. 714-757.

Culick, F.E.C. (1987) “A Note on Rayleigh’s Criterion”, Combust. Sci. and Tech., Vol. 56, pp. 159-166.

Culick, F.E.C. (1999) “Combustor Dynamics: Fundamentals, Acoustics, and Control”, A Short Course of Lectures, United Technologies Research Center.

Culick, F.E.C. and Jahnke, C. (1994) “An Application of Dynamical Systems Theory to Nonlinear Combustion Instabilities”, J. Prop. and Power, Vol. 10, No. 4, pp. 508-517.

Crosley, D. (1993) “Collisional effects on laser-induced fluorescence flame measurements”, Optical Engineering, Vol. 20, No. 7.

Dieke, G.H. and Crosswhite, H.M. (1962) “The Ultraviolet Bands of OH”, J. Quant. Spectrosc. Radiat. Transfer, Vol. 2, pp. 97-199.

Dyer, M.J. and Crosley, D.R. (1982) “Two-dimensional imaging of OH laser-induced fluorescence in a flame”, Optics Letters, Vol. 7, No. 8.

Eckbreth, R.C. (1988) Laser Diagnostics for Combustion Temperature and Species, Abacus Press, Cambridge.

Fric, T.F., (1993) “Effects of Fuel-Air Unmixedness on NOx Emissions”, Journal of Propulsion and Power, Vol. 9, No. 5, pp. 708-713.

Hanson, R.K., Seitzman, J.M., and Paul. P.H. (1990) "Planar Laser-Fluorescence Imaging of Combustion Gases", Applied Physics B, Vol. 50, pp. 441-454.

Heberle, N.M., Smith, G.P., Jeffries, J.B., Crosley, D.R., and Dibble, R.W., (2000) "Simultaneous laser-induced fluorescence and Rayleigh scattering measurements of structure in partially premixed flames", Appl. Phys. B, Vol. 71, pp. 733-740.

Howe, M.S. (1998) Acoustics of Fluid-Structure Interactions, Cambridge University Press, Cambridge.

Hurle, I.R., Price, R.B., Sugden, T.M., and Thomas, A., (1968) "Sound Emission from Open Turbulent Premixed Flames", Proc. Roy. Soc., Vol. 303, pp. 409-427.

Isella, G.C. (2001) "Modeling and Simulation of Combustion Chamber and Propellant Dynamics and Issues in Active Control of Combustion Instabilities", Ph.D. Thesis, California Institute of Technology, Pasadena, California.

Isella, G., Seywert, C., Culick, F.E.C., and Zukoski, E.E. (1997) "A Further Note on Active Control of Combustion Instabilities Based on Hysteresis" Combust. Sci. and Tech., Vol. 126, pp. 381-388.

John Zink Corp. (1988) "Biogas Flares" presented at the GRCDA 11th Annual International Landfill Symposium, Houston, Texas.

Kanury, A.M., (1975) Introduction to Combustion Phenomena, Gordon and Breach Science Publishers, New York.

Kappei, F., Lee, J.Y., Johnson, C.E., Lubarsky, E., Neumeier, Y., and Zinn, B.T. (2000) "Investigation of Oscillatory Combustion Processes In Actively Controlled Liquid Fuel Combustor", presented at the 36th Joint Prop. Conf., Huntsville, Al, AIAA 2000-3348.

Katto, Y., and Sajiki, A. (1977) "Onset of Oscillation of a Gas-Column in a Tube Due to the Existence of Heat-Conduction Field (A Problem of Generating Mechanical Energy from Heat)", *Bulleton of the JSME*, Vol. 20, No. 147, pp. 1161-1168.

Kendrick, D.W., (1995) “An Experimental And Numerical Investigation Into Reacting Vortex Structures Associated With Unstable Combustion”, Ph.D. Thesis, California Institute of Technology, Pasadena, CA.

Kendrick, D.W., Anderson, T.J., Sowa, W.A., and Snyder, T.S. (1999) “Acoustic Sensitivities of Lean-Premixed Fuel Injectors in a Single Nozzle Rig”, J. Eng. Gas Turbines and Power, Vol. 121, Iss. 3, pp. 429-436.

Kwon, Y-P., and Lee, B-H. (1985) “Stability of the Rijke thermoacoustic oscillation”, J. Acoust. Soc. Am., Vol. 74, No. 4, pp. 1414-1420.

Laufer, G., (1996) “Introduction to Optics and Lasers in Engineering”, Cambridge University Press, Cambridge, UK.

Lucht, R.P., Laurendeau, N.M., and Sweeney, D.W.,(1982) “Temperature measurement by two-line laser-saturated OH fluorescence in flames”, Applied Optics, Vol. 21, No. 20, pp. 3729-3735.

Madarame, H. (1981a) “1st Report: Oscillations Induced by Plane Heat Source in Air Current”, *Bulletin of the JSME*, Vol. 24, No. 195, Sept. 1981.

Madarame, H. (1981b) “2nd Report: Oscillations induced by Interference of Heat Sources”. *Bulletin of the JSME*, Vol. 24, No. 198, Dec. 1981.

Maling, G.C. (1963) “Simplified Analysis of the Rijke Phenomenon”, *JASA*, Vol. 35, No. 7, pp. 1058-1060.

Masayuki, T., Berg, P.A., Harrington, J.E., Luque, J., Jeffries, J.B., Smith, G.P., and Crosley, D.R., (1998) "Collisional Quenching of CH(A), OH(A), and NO(A) in Low Pressure Hydrocarbon Flames", Combustion and Flame, Vol. 114, pp. 502-514.

Masri, A.R., Dibble, R.W., and Barlow, R.S., (1996) "The Structure of Turbulent Non-premixed Flames Revealed by Raman-Rayleigh-LIF Measurements", Prog. Energy Combust. Sci., Vol. 22, pp. 307-362.

McManus, K., Yip, B., and Candel, S., (1995) "Emission and Laser-Induced Fluorescence Imaging Methods in Experimental Combustion", Experimental Thermal and Fluid Science, Vol. 10, pp. 486-502.

Murray, R.M. (1995) Sparrow Reference Manual, California Institute of Technology.

Palm, S.L. (in progress) "Dynamic Response of Premixed and Non-Premixed Flames Under Acoustic Forcing", Ph.D. Thesis, California Institute of Technology, Pasadena, CA.

Palmer, J.L., and Hanson, R.K., (1996) "Temperature imaging in a supersonic free jet of combustion gases with two-line OH fluorescence", Applied Optics, Vol. 35, No. 3, pp. 485-499.

Paul, P.H. (1994) "A Model for Temperature Dependent Collisional Quenching of OH A2 ∑+", J. Quant. Spectrosc. Radiat. Transfer, Vol. 51, No. 3, pp. 511-524.

Paul, P.H., and Dec, J.E. (1994) "Imaging of reaction zones in hydrocarbon-air flames by use of planar laser-induced fluorescence of CH", Optics Letters, Vol. 19, No. 13.

Paul, P.H., Gray, J.A., Durant, J.L., and Thoman, J.R., (1993) "A Model for Temperature-Dependent Collisional Quenching of NO A2 ∑+", Appl. Phys. B, Vol. 57, pp. 249-259.

Paul, P.H., Gray, J.A., Durant, J.L., and Thoman, J.R. (1994) "Collisional Quenching Corrections for Laser-Induced Fluorescence Measurements of NO A2 ∑+", AIAA Journal, Vol. 32, No. 8.

Poinsot, T.J., Trouve, A.C., Veynante, D.P., Candel, S.M., and Esposito, E.J., (1987) "Vortex-driven acoustically coupled combustion instabilities", J. Fluid Mech., Vol. 177, pp. 265-292.

Poinsot, T., Bourienne, F., Candel, S., and Esposito, E., (1989) "Suppression of Combustion Instabilities by Active Control", Journal of Propulsion and Power, Vol. 5., No. 1, pp. 14-20.

Poncia, G. (1998) "A Study on Thermoacoustic Instability Phenomena in Combustion Chambers for Active Control", *Ph.D. Thesis*, Politecnico di Milano.

Pun, W., Palm, S.L., and Culick, F.E.C. (2000) "PLIF Measurements of Combustion Dynamics in a Burner under Forced Oscillatory Conditions" AIAA-2000-3123, *presented at the 36th Joint Propulsion Conference*, Huntsville, AL.

Putnam, A.A., and Dennis, W.R. (1954) "Burner Oscillations of the Gauze-Tone Type", J. Acoust. Soc. Am., Vol. 26, No. 5, pp. 716-725.

Qin, W., Egolfopoulos, F.N., and Tsotsis, T.T. (2001) "A Detailed Study of the Combustion Characteristics of Landfill Gas", Chemical Engineering Journal, Vol. 3773, pp. 1-16.

Raun, R. L., Beckstead, M.W., Finlinson, J.C., and Brooks, K.P. (1993) "A Review of Rijke Tube Burners and Related Devices", Prog. Energy Combust. Sci., Vol. 19, pp. 313-364.

Rayleigh, J.W.S. (1945) The Theory of Sound Vol. II, Dover Publications, New York.

Rijke, P. (1859) “Notiz über eine neie Art, die Luft in einer an beiden Enden offenen Röhre in Schwingungen zu versetzen”, *Annal der Physik*, Vol. 107, pp. 339-343.

Rosfjord, T. (1995) “Lean-Limit Combustion Instability” *United Technologies Research Center*.

Samiengo, J.M., Yip, B., Poinsot, T., and Candel, S., (1993) “Low-Frequency Combustion instability Mechanisms in a Side-Dump Combustor”, Combustion and Flame, Vol. 94, Iss. 4, pp. 363-380.

Sankar, S.V., Jagoda, J.I., and Zinn, B.T., (1990) “Oscillatory Velocity Response of Premixed Flat Flames Stabilized in Axial Acoustic Fields”, Combustion and Flame, Vol. 80, pp. 371-384.

Schadow, K., Yang, V., Culick, F.E.C., Rosjford, T., Sturgess, G., and Zinn, B., (1996) “Active Combustion Control for Propulsion Systems”, AGARD Workshop Report, May 6-9, 1996, Athens, Greece.

Seitzman, J.M., and Hanson, R.K., (1993) “Comparison of Excitation Techniques for Quantitative Fluorescence Imaging of Reacting Flows”, AIAA Journal, Vol. 31, No. 3, pp. 513-519.

Seywert, C. (2001) “Combustion Instabilities: Issues in Modeling and Control” Ph.D. Thesis, California Institute of Technology, Pasadena, California.

Shih, W.P, Lee, J.G., and Santavicca, D.A., (1996) “Stability and Emissions Characteristics of a Lean Premixed Gas Turbine Combustor”, Twenty-Sixth Symposium (International) on Combustion, The Combustion Institute.

Smith, G.P., Luque, J., Jeffries, J.B., Crosley, D.R. (2001) “Rate Constants for Flame Chemiluminescence”, 2nd Joint Meeting of the U.S. Sections of the Combustion Institute, Oakland, CA.

Sterling, J.D., (1987) “Longitudinal Mode Combustion Instabilities in Air Breathing Engines”, Ph.D. Thesis, California Institute of Technology, Pasadena, CA.

Sterling, J.D. and Zukoski, E.E., (1991) “Nonlinear Dynamics of Laboratory Combustor Pressure Oscillations”, Combust. Sci. and Tech., Vol. 77, pp. 225-238.

Swenson, G., Pun, W., and Culick, F.E.C., (1996) “Nonlinear Unsteady Motions and NOx Production in Gas Turbine Combustors”, 11th Symposium on Combustion and Explosion, Russian Academy of Sciences, Chernogolovka, Russia, November.

Venkataraman, K.K., Preston, L.H., Simons, D.W., Lee, B.J., Lee, J.G., and Santavicca, D.A. (1999) “Mechanism of Combustion Instability in a Lean Premixed Dump Combustor”, J. Propul. Power, Vol 15, Iss. 6, pp. 909-918.

Wu, S., Blake, G.A., Sun, S., and Ling, J., “A multicrystal harmonic generator that compensates for thermally induced phase mismatch”, Optics Communications, Vol. 173, pp. 371-376.

Yip, B., Miller, M.F., Lozano, A., and Hanson, R.K. (1994) “A combined OH/acetone planar laser-induced fluorescence imaging technique for visualizing combusting flows”, Experiments in Fluids, Vol. 17, pp.330-336.

Zsak, T.W. (1993) “An Investigation of the Reacting Vortex Structures Associated with Combustion”, Ph.D. Thesis, California Institute of Technology, Pasadena, CA.